Institut für Geodäsie und Geoinformation

Effects on the Geodetic-VLBI Observables Due to Polarization Leakage in the Receivers

I n a u g u r a l - D i s s e r t a t i o n

zur
Erlangung des Grades
Doktor-Ingenieur
(Dr.-Ing.)

der
Hohen Landwirtschaftlichen Fakultät
der
Rheinischen Friedrich-Wilhelms-Universität
zu Bonn

vorgelegt am 26. April 2010 von

Dipl.-Phys. Alessandra Roy

aus S. Dona' di Piave

Angefertigt mit Genehmigung der Landwirtschaftlichen Fakultät der Rheinischen Friedrich-Wilhelms-Universität Bonn

Referent: Priv.-Doz. Dr.-Ing. Axel Nothnagel

Korreferenten: Univ.-Prof. Dr.-Ing. Heiner Kuhlmann

Univ.-Prof. Dr.-rer. nat. Anton Zensus

Tag der mündlichen Prüfung: 07. Jun 2010

Contents

Abstract

Geodetic VLBI delivers baseline length and Earth orientation parameter measurements, which offer the most viable and precise way to study Earth crustal and core dynamics and to support space navigation. The precision of these geodetic and astrometric measurements is degraded by instrumental errors of which polarization leakage is one of the larger.

Its effect can be corrected in the data provided one knows the leakage characteristics of the stations. In this work I introduce the concept of polarization, why it needs to be considered in the geodetic analysis and present a VLBI experiment that measured the polarization leakage at 16 geodetic and VLBA stations over the frequency range 8212.99 MHz to 8932.99 MHz and 2225.99 MHz to 2365.99 MHz. I describe resulting polarization leakage measurements and the algorithm that was implemented to correct for their effect on the geodetic delay measurables. I applied the correction for polarization leakage to a routine geodetic VLBI experiment and check for the resulting improvement.

From the measured leakage terms, one would expect polarization leakage to affect the group delay measurements by 0.5 ps to 7 ps, depending on the stations involved in the baseline. This proved to be below the statistical noise in a single VLBI experiment and so the improvement from the correction could not be detected.

Polarization leakage was found, unespectedly, not the dominant source of non-closing errors.

Zusammenfassung

Die durch geodätisches VLBI ermittelten Basislinenlängen und Erdrotationsparameter bieten die praeziseste Methode, Erdkrusten- und Kerndynamik zu studieren und Weltraumnavigation zu unterstützen.

Polarisationsverluste gehören zu den instrumentellen Störungen, die die Präzision der geodätischen und astrometrischen Messungen verringern. Ihr Effekt kann in den Daten korrigiert werden, vorausgesetzt man kennt die Verlust-Charakteristika. In dieser Arbeit stelle ich kurz das Konzept der Polarisation vor und warum sie in der geodätischen Analyse berücksichtigt werden muss. Ich stelle RD0705 vor, ein Projekt zur Messung der Polarisationsverluste an einigen geodätischen VLBI Stationen und am VLBA. Ich beschreibe die Beobachtungsstrategie, die verwendet wird, um die Verluste zu messen, den Prozess der Korrelation, die Datenreduktion und die erzielten Ergebnisse.

Chapter 1

Introduction

1.1 Radio Interferometry and its Geodetic Application

Very long baseline interferometry (VLBI) is a radio interferometric technique used in astronomy to study the sky at radio wavelengths (i.e. from a wavelength, λ, of about 1 mm to 10 m) with an extremely high angular resolution. Thanks to the high resolution compared to that of single radio telescopes, radio interferometry enables the study of small structures within the cores of the quasi stellar radio objects (quasars), gives precise positions of the quasars on the sky, and gives very high accuracy station positions for geodesy. VLBI techniques pay a lot of attention to the geometry and can measure accurately the arrival time of the wavefronts at the different radio telescopes. Because of this, this technique can be used to localize the position of the stations within a few millimetres. These measurements are used to study plate tectonics, earth rotation, polar motion and other geophysical phenomena. The use of VLBI in geodesy is fundamental because it is one of the few techniques that is referenced to an approximately inertial frame: the one defined by the quasars, which are effectively at infinite distance from the observer and hence irrotational. Only VLBI and ring laser gyroscopes can keep trace of the orientation of the spin axis of the earth and of the variation of the rotation of the earth over the long term.

The geodetic observable obtainable from VLBI measurements is the difference in propagation time of electromagnetic radiation from the quasars to the antennas (group delay). Within the past 35 years the precision of the geodetic measurements has improved by a factor 100, from metre precision (Hinteregger et al 1972) down to a few millimetre precision (Niell et al 2007) opening possibilities for geophysicists to study the earth interior dynamics and climatologists to study the climate (Chao 2004). Still, the requirement to increase the precision drives geodesists to eliminate, where possible, factors that hinder their goal of reaching the sub-millimetre level (Niell et al 2007). Among these factors, the primary limitations come from the atmospheric and ionospheric refraction, source structure and instrumental effects such as polarization leakage (D-term).

1.2 Past Studies

That polarization leakage affects the VLBI measurements has been known for more than a decade but both the geodetic and astronomical communities have conducted only a very few studies to either model theoretically or measure the contamination of the observables by polarization leakage. Rogers (1991) in his brief theoretical work, adopted a nominal value for polarization leakage of -15 dB (corresponding to a leakage of about 3 % of the power from one polarization into the other) and estimated from it, for unpolarized radio sources, a group delay error of the order of 14 ps (4.2 mm) or less. For 10 %-polarized radio sources typically an extra 8 ps (2.4 mm) error was determined assuming that the polarization leakage introduces a phase gradient over a 360 MHz bandwidth. This work does not permit correction of

polarization leakage on the individual geodetic stations because it did not make any measurements and instead used a nominal worst case leakage.

Corey and Titus (2006) measured the polarization leakage of the antennas of the Very Long Baseline Array (VLBA) and found them to be less than -20 dB at both 2.3 GHz (S-band) and 8.4 GHz (X-band), so the leakage is less than 1 % of the power from one polarization into the other. They estimated from that a maximum of 1.0 ps (0.3 mm) multiband delay (MBD) error at X-band and a maximum of 2.2 ps (0.7 mm) MBD error at S-band. At a few geodetic sites, they measured the polarization leakage to be typically greater than -20 dB, leading to MBD errors between 2 ps (0.6 mm) and 9 ps (2.7 mm) at X-band. They observed using six VLBA antennas for 8 hours observing 16 frequencies, four at a time and derived the leakage terms for these stations. Then those VLBA stations and ten geodetic stations observed for another 16 hours. In the analysis they applied the leakage corrections to the VLBA stations to make them effectively leakage free. Then they used the observations of radio sources to derive the leakage at the geodetic stations acknowledging that any intrinsic source polarization would contaminate the leakage measurements. Of these 10 geodetic stations, only four have the value of the leakage published and of these four, three have unfortunately been decommissioned since then.

Another early attempt to measure the leakage characteristic for geodesy, was made by Petrov in 1998[1]. Petrov added three scans to the end of the experiment Europe46 to derive leakage and conducted a dedicated experiment (BRD01) but the results were never properly published.

In these investigations the errors caused by the polarization leakage appeared to be small at that time, but are now significant compared to the target accuracy of 1 mm set as the goal for the VLBI2010 project (Niell et al 2007).

In an astronomical experiment, Massi et al (1997) measured the variation of leakage amplitude with frequency using the European VLBI Network antennas. These changes in amplitude caused a reduction in dynamic range (peak to rms ratio) in images made using these antennas compared to images made using the VLBA antennas. The measured leakage amplitudes are shown in Figure 1.1. This was a purely astronomical work and did not consider the effects of the leakage on the delay measurement. In a later work (Sorgente and Massi 1997) developed the theoretical framework showing the effects of the polarization leakage phases on VLBI observables, but without any further exploitation.

The need for new measurements arose because of increased accuracy requirements and because in the previous studies only approximate values were established. The calibrators were assumed to be unpolarized, the sources were not imaged, the bandwidth spanned for the geodetic antennas by Corey and Titus (2006) was only 360 MHz of the 720 MHz available at X-band, and some stations upgraded the receivers since when those measurements were made.

1.3 The New Project

The aim of this project was to investigate at what level the group delay measurements are affected by polarization leakage, which is one of the biggest known instrumental effects, and to develop, implement and demonstrate a procedure for the correction of polarization leakage effects. The results showed that the leakage error is smaller than the value obtained by Corey and Titus (2006) and Rogers (1991) and that there are larger sources of error that contaminate the delay that should be dealt with first.

In this study I carried out a 24 hour observing session with 16 IVS and VLBA stations and analyzed the data assuming that the observed sources could be polarized and therefore I had to produce images of the sources to determine simultaneously the source structure, the intrinsic polarization and the polarization leakage. Hence I covered the full geodetic wide-band from 8212 MHz to 8932 MHz at X-band and from 2225 MHz to 2365 MHz at S-band. I determined the polarization leakage covering the full bandwidth in 16 MHz steps, for better interpolation of the leakage vectors across the whole bands and in case the geodetic frequency sequence is changed in the future. This study established a procedure for high-quality

[1] http://astrogeo.org/petrov/projects/plrz/plrz.html

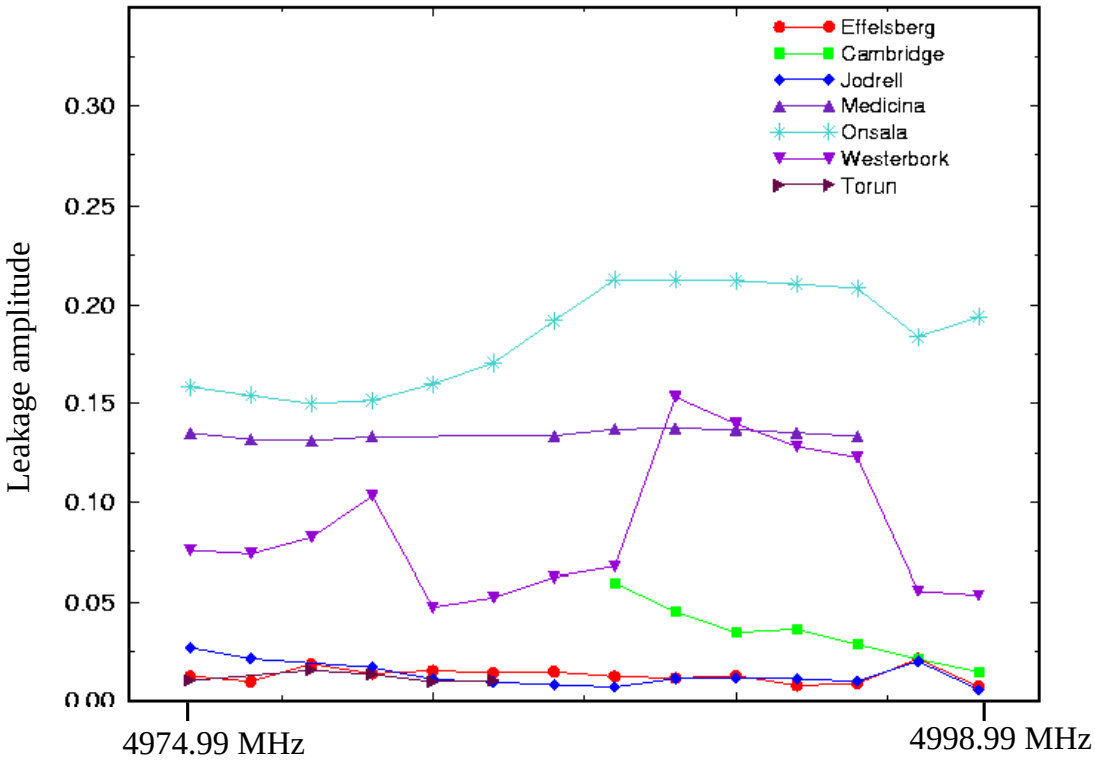

Figure 1.1: Polarization voltage leakage amplitudes of the European VLBI Network (EVN) antennas vs frequency (Massi and Aaron 1997).

measurements and correction of the leakage. It applied the corrections to a routine geodetic VLBI network observation to verify the improvement. The study is based upon a subset of antennas, but the procedure can be applied to the whole geodetic network (at a later stage).

Chapter 2

Introduction to Very Long Baseline Interferometry

2.1 VLBI Technique

The technique of very long baseline interferometry (VLBI) can be used to realize a reference frame defined by distant radio sources (quasars). Since quasars appear to be stationary with respect to the earth on the scale of a human life time, the reference frame defined by them is in good approximation inertial and it is the best known inertial frame. Geodesy requires the use of an inertial frame to measure position and motions of the earth and its long-term variation, therefore VLBI is a fundamental technique for geodesy. In VLBI widely separated radio telescopes are used to form an interferometer array that can form images or measure radio source positions with very high angular resolution. The stations have independent clocks and data are recorded for later playback and correlation. Very precise atomic clocks (hydrogen masers) are required to keep track of time to maintain coherence among the electronics of the various antennas to permit coherent integration to build up signal-to-noise ratio. They are required also because, at the correlators, the peak of the interference pattern can be searched for within a delay window of only a few microseconds (maximum 20 μs, due to hardware limitations). Since there is no physical link among the antennas, they can be located far away from each other. After recording, the data are sent to a correlator where the signals coming from the various telescopes are superimposed and the interference pattern is reconstructed. If one maps the interference pattern onto a coordinate system representing the sky, then one obtains an image of the source observed. The more telescopes that participate in the observation, the more detailed is the image. It is possible to quantify the resolution (i.e. the minimum angular distance between distinguishable points on the sky) obtained by imaging devices from the Airy formula (Airy 1835) which is

$$\sin\Theta = 1.220 \cdot \frac{\lambda}{D} \tag{2.1}$$

where Θ is the angular resolution in radians, λ is the wavelength of the radiation and D is the diameter of the lens, which in radio interferometry corresponds to the distance between the two telescopes in the array (i.e. the maximum baseline length). It is clear from Equation 2.1 that the further apart the telescopes, the higher the angular resolution. For astronomers this means more detailed images of the radio source studied, for geodesists this means higher accuracy in determining earth orientation parameters (EOP), plate tectonics, polar motion and other geophysical phenomena (Robertson 1991).

2.2 Response of an Interferometer

Two spatially separated telescopes observing a quasar receive the same wavefront at two different times due to the geometry as shown in Figure 2.1. In this paragraph I will treat the signal as quasi-monochromatic since real broad-band signals can be considered as sum of quasi-monochromatic signals. The path length, and hence the number of turns of phase, that the signal has gone through from source to antenna is different for the two antennas. After the signals have been received by the two antennas they are cross-multiplied against each other and integrated in time (the signals are cross-correlated). Before cross-multiplication the signals are $V_1 = V_0 \cos(2\pi\nu t)$ and $V_2 = V_0 \cos(2\pi\nu(t - \tau_g))$, where V_1 and V_2 are the sinusoidal voltage responses of the antennas to the incoming electric field, V_0 is the amplitude, ν is the frequency and τ_g is the geometrical delay as described in Figure 2.1. After cross-multiplication and integration the signal is

$$\langle \mathrm{V}_1 \cdot \mathrm{V}_2 \rangle = V_0^2 \cdot \cos(2\pi\nu\tau_\mathrm{g}) \tag{2.2}$$

The output of the correlator is a cosinusoid as the source moves, since the argument of the cosine involves the geometrical delay, which changes while the source is moving in the sky as visible in Figure 2.2. In the case that the argument of the cosine is $\frac{(2n+1)\pi}{2}$ where $n \in \mathbb{Z}$, then the result of Equation 2.2 is zero. Thus the information on the amplitude of the signal, which in turn is related to the source strength, is lost. To recover this information, one would build complex correlators, which split the output from each antenna into two copies and introduce a 90° shift in the signal phase in one of the two and cross correlate as above. The output of this 90° shifted correlator channel is a sinusoid as the source moves. The zeros of the sine channel are separated in phase by 90° with the zeros of the cosine channel, which guarantees no loss of information. Therefore the response of an interferometer is constituted by two terms: a sinusoid and a cosinusoid both of which are used for reconstructing the source position and its intensity.

In the real case the number of turns of phase depends not only on the geometrical delay, as considered above, but also on the tropospheric refraction, the ionospheric refraction and on telescope-based phenomena, like different cable path lengths. The total phase delay in radians, ϕ_T, can be expressed as the sum of all these terms, as

$$\phi_\mathrm{T} = 2\pi\nu(\tau_\mathrm{g} + \tau_\mathrm{n}) + \tau_\mathrm{iono}(\nu) \tag{2.3}$$

where τ_g is the geometrical delay in seconds, τ_n is the non-dispersive delay component due to the troposphere and the instrumental effects and τ_iono is the frequency-dependent delay introduced by the ionosphere (Fomalont 1999).

2.3 The Geometrical Delay: The Fundamental Geodetic VLBI Observable

The total phase delay is, unfortunately unusable for geodesy over wide angles in the sky, since this quantity is calculated by the correlator modulo 360° and has ambiguities ($\phi_\mathrm{T} = \phi_\mathrm{T} + 2n\pi$, with $n \in \mathbb{Z}$). Geodesy instead uses the group delay, τ_gd, which is the first derivative of the phase delay expressed in turns of phase with respect to frequency given by

$$\tau_\mathrm{gd} = \frac{1}{2\pi}\frac{d\phi_\mathrm{T}}{d\nu} = \tau_\mathrm{g} + \tau_\mathrm{n} + \frac{d}{d\nu}(\tau_\mathrm{iono}(\nu)) \tag{2.4}$$

where τ_gd is the group delay. In this way, the ambiguities are avoided at the expense of precision, which is higher for the phase delay that for the group delay.

The group delay still contains a dispersive contribution coming from the ionosphere that needs to be removed. Geodetic VLBI measurements are made at two frequencies, from which the ionospheric

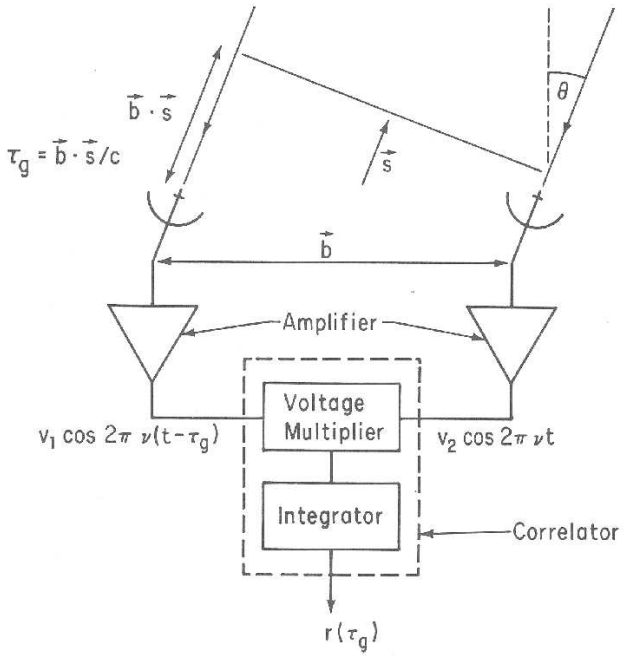

Figure 2.1: Simplified representation of an interferometer (Thompson 1999). Only the geometrical delay (τ_g) is shown, therefore the response of this interferometer, $r(\tau_g)$, is expressed as a function of the geometrical delay only. The geometrical delay is also the major contribution to the total phase delay. The correlator depicted shows only the cosine correlator channel.

contribution can be cancelled (Fomalont 1999). The term due to the troposphere is derived using the group delay measurements themselves and will be treated in more detail later as one of the major sources of error in determining precise delays.

The basic idea of how baseline length and source position are extracted from the group delay is illustrated in Figure 2.2. For simplicity I will consider only the geometrical delay. The top panel illustrates the apparent motion of the quasar above two antennas forming the baseline of length b. As the source rises, the delay is maximum. As the source transits over the telescopes the delay is zero. As the source sets in the west, the delay reaches again a maximum but with the opposite sense from that when the source rose. The geometrical delay is the scalar product $\vec{b}\cdot\vec{s}$ where $\vec{s}$ is the direction to the source and $\vec{b}$ is the vector describing the baseline. The scalar product can be expressed as a function of the angle (Θ) between the baseline and the source direction as $b\cos\Theta$. The bottom panel represents how the delay changes with time. The curve is a sinusoid: at time zero the source rises and the delay is maximum ($\cos\Theta = 1$). Six hours later, the source is at zero delay ($\cos\Theta = 0$) and 12 hours after rising, the source sets and the delay is negative maximum ($\cos\Theta = -1$). In the two dimensional case, one can find the baseline length from the amplitude of the sinusoid in Figure 2.2. From the phase of the sinusoid, one can find a combination of the source position and the baseline orientation. From the vertical offset of the sinusoid one can find the clock offset due to timing errors between the antennas. In reality one would perform more observation than the number of parameters to be estimated, in this way the problem is overdetermined and can be solved by least square parameter estimation (Sovers et al 1998).

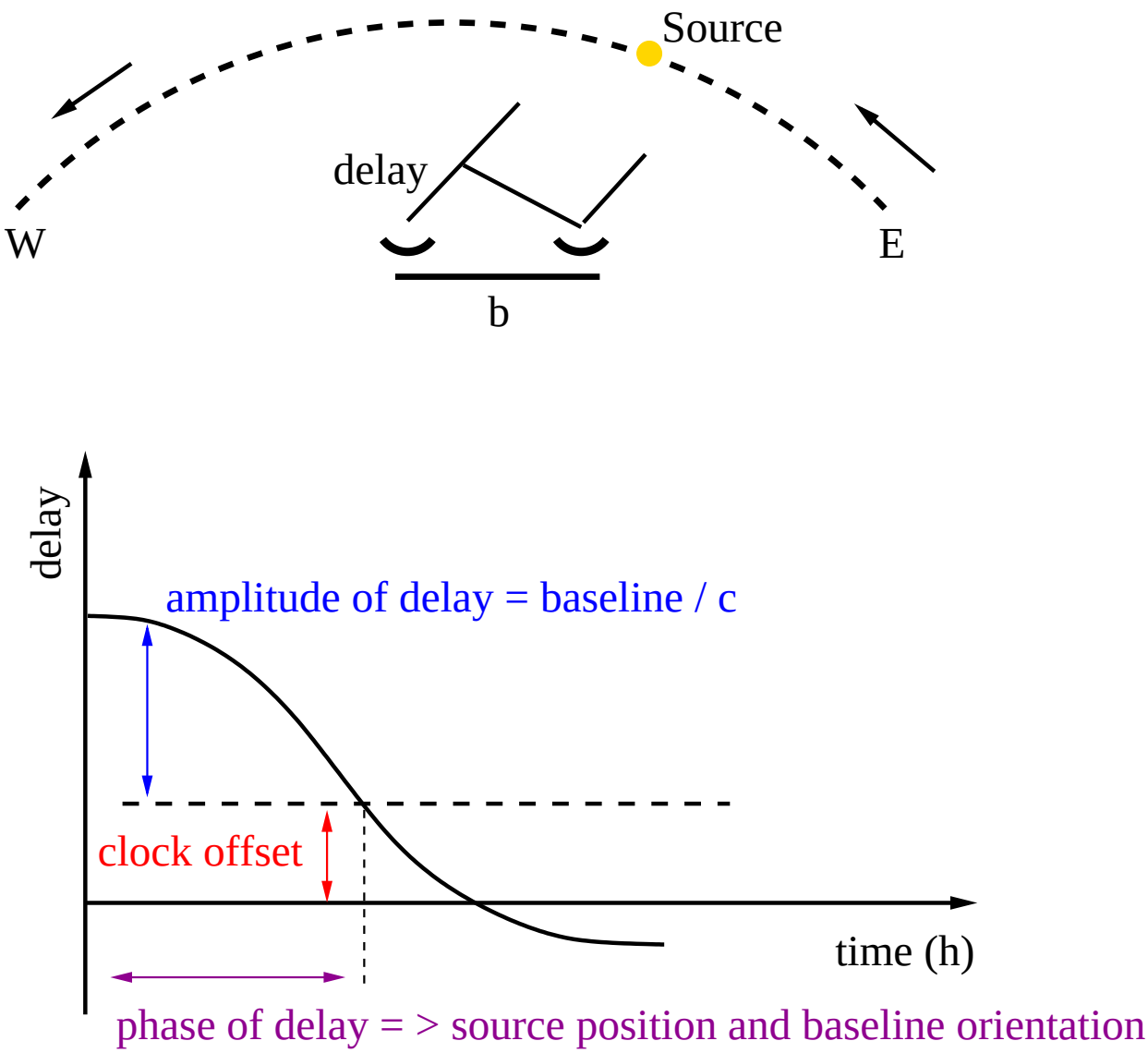

Figure 2.2: Top: motion of a source above two telescopes. Bottom: geometrical delay versus time for the situation in the top plot. The delay describes a sinusoid while the source moves over the two antennas: from the amplitude of the sinusoid it is possible to reconstruct the baseline length, from the phase of the sinusoid it is possible to reconstruct the source position and the baseline orientation and from the vertical offset of the sinusoid it is possible to reconstruct the clock model offset.

2.4 VLBI Hardware Description

In order to understand technical implications addressed in later chapters, I will shortly introduce the signal path from the antenna to the recorder. There are different kinds of VLBI hardware systems built by different groups at different times, but all are more or less compatible with each other. The most commonly used types are presently the VLBA, the Mark IV, the hybrid VLBA4 and the Japanese K5. Figure 2.3 shows the analogue signal path along with the data acquisition rack for a VLBA antenna (Thompson 1993) as representative of a typical VLBI system. The incoming electric field in free space ($\vec{E} = E_0 \cos(\omega t)$) is first converted into a voltage on cables using an antenna ($V = V_0 \cos(\omega t)$), it passes through amplifiers and bandpass filters ($V = gV_0 \cos(\omega t)$, where g is a gain factor coming from the amplification), is multiplied (mixed) against a local oscillator (LO) whose signal is ($V_{\rm LO} \cos(\omega_{\rm LO} t)$, with $\omega_{\rm LO} \approx \omega$ to become $V = \frac{V_0 V_{\rm LO}}{2}[\cos(\omega + \omega_{\rm LO}) + \cos(\omega - \omega_{\rm LO})$. Finally it passes through a low pass filter leaving $V = \frac{V_0 V_{\rm LO}}{2} \cos(\omega - \omega_{\rm LO})$.

The downconversion to lower frequencies is done because the performance of subsequent circuitry is better at low frequencies (Brophy 1990), the selectivity of filters is improved enormously since the filters at low frequency can have large fractional bandwidth unlike if filtering at the original radio frequency (RF), and the attenuation during signal transmission through cables is much reduced[1]. The part described above is in the receiver cabin at the antenna.

The signal is transported from the receiver cabin to the rack either via four IF cables (for the VLBA stations) or via two intermediate frequency (IF) cables (for the Mark IV stations). Four cables allow for two frequencies and two polarizations simultaneously, as needed for this experiment.

Upon arrival at the control room the signal passes through IF distributor modules, which amplify the signal and split it eight ways per IF cable. The Mark IV station has the additional complexity that four of those output passes through a band-pass filter leaving signals from 96 MHz to 224 MHz (IF1 low) and the other four pass through a band-pass filter leaving signals from 216 MHz to 504 MHz (IF1 high) (Clark and Rogers 1982). Another complication in the Mark IV rack is the later addition of a second IF distributor module (IF3) to expand the spanned bandwidth from 360 MHz to 720 MHz for greater precision in the delay measurement. The 8.4 GHz (X-band) IF signal is split into two signals, one of which feeds the IF1 distributor and the other feeds the IF3 distributor. The IF3 output is split four ways. From the IF distributors the signals pass to the baseband converters (BBC), where they are downconverted from IF to baseband frequencies. The downconversion is performed with sideband-separating mixers and tuneable LOs, each of which yields two outputs, one for the upper sideband and one for the lower sideband. The signal is then low-pass filtered and time sampled with one or two bit resolution, formatted into data frames with time stamps by the formatter and recorded onto magnetic discs with, e.g., Mark 5A or Mark 5B recorders.

The VLBA4 is composed of a VLBA rack and a Mark IV formatter, replacing the original VLBA formatter.

[1] attenuation proportional to the frequency to the power of two, Arndt 1996

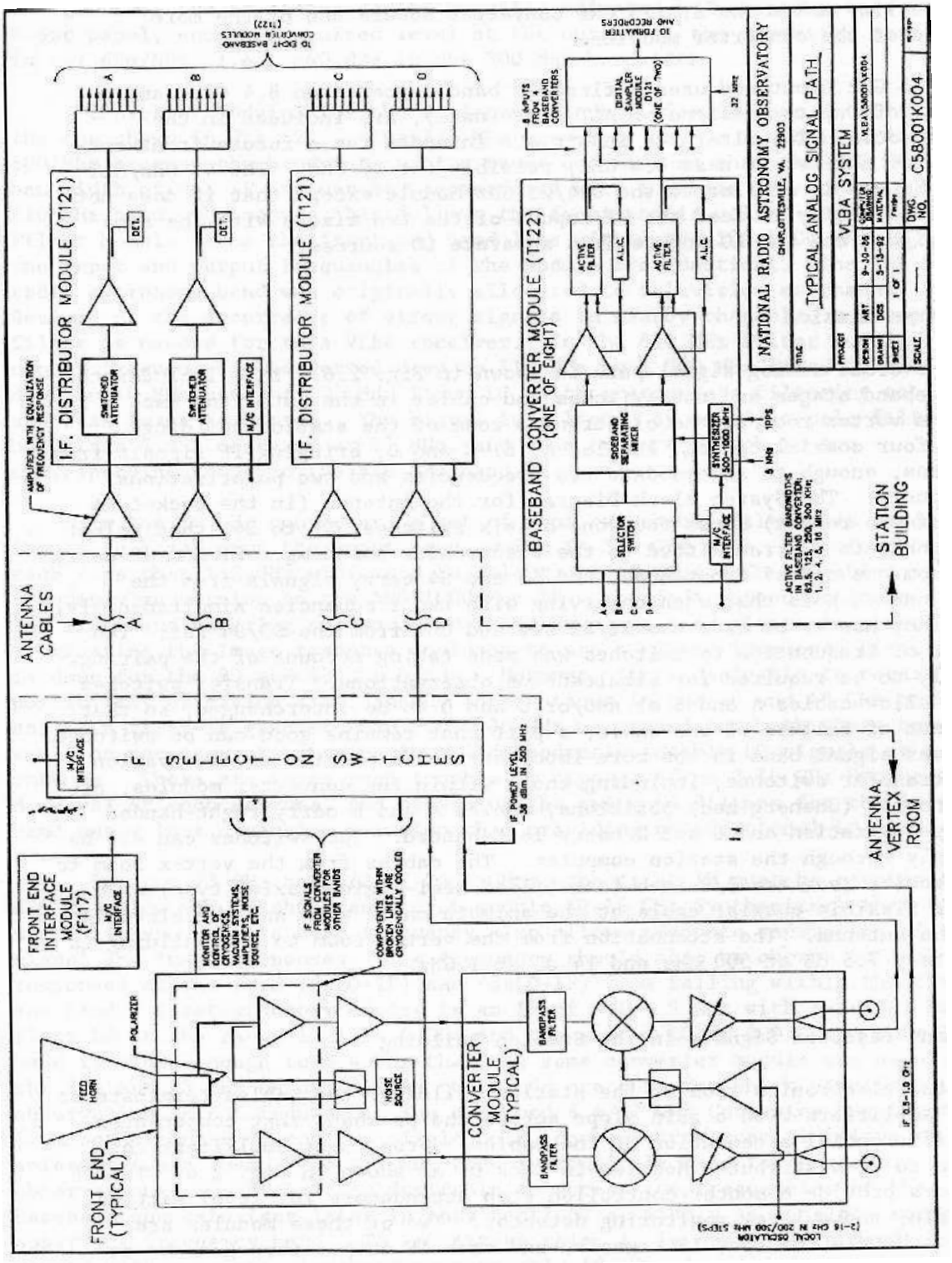

Figure 2.3: Block diagram of a VLBA analogue signal path including the data acquisition rack, at radio frequency, intermediate frequency and baseband frequency (from Thompson 1993).

Chapter 3

Polarization Leakage Effects on the Delay

3.1 Concept of Polarization

The equation describing a propagating monochromatic electromagnetic wave in space can be derived from Maxwell's equations (Jackson 1998) and is

$$\vec{\nabla}^2\vec{\mathrm{E}} = c^{-2}\frac{\partial^2\vec{\mathrm{E}}}{\partial t^2} \tag{3.1}$$

where $\vec{\mathrm{E}}$ is the electric field of the wave and c is the speed of light. I will confine myself to study only the electric field of the wave, since the receiving antennas commonly used in VLBI respond only to the electric component of the incoming electromagnetic wave. In free space, far enough from the source of the emitted radiation, one of the possible solutions of Equation 3.1 is a plane propagating wave, e.g., along the z axis:

$$\vec{\mathrm{E}}(x,y,z,t) = \vec{\mathrm{E}}_0 e^{-i(kz-\omega t+\delta)} \tag{3.2}$$

where k is the propagation constant in m^{-1}, ω is the angular frequency in rad s^{-1} and δ is a constant phase in radians. Projecting the electric vector (Equation 3.2) onto two perpendicular axes, x and y, that are perpendicular to the direction of propagation of the wave, z, we have the system:

$$\begin{cases} E_x = E_1\cos(kz-\omega t+\delta_1) \\ E_y = E_2\cos(kz-\omega t+\delta_2) \\ E_z = 0 \end{cases} \tag{3.3}$$

where $E_1^2 + E_2^2 = E_0^2$. Equation 3.3 represents the case illustrated in Figure 3.1a.

If we consider the motion of the tip of the electric vector with time at a fixed position in space, we see that the tip of $\vec{\mathrm{E}}$ describes a circle (Figure 3.1b), or oscillates along a line (Figure 3.1c), or describes an ellipse (Figure 3.1d). The formula describing the locus traced out over all time is

$$(\frac{E_x}{E_1})^2 + (\frac{E_y}{E_2})^2 - 2\frac{E_x}{E_1}\frac{E_y}{E_2}\cos(\delta_1-\delta_2) = \sin^2(\delta_1-\delta_2) \tag{3.4}$$

Equation 3.4 describes an ellipse. If $E_1 = E_2$ and simultaneously $\delta_1 - \delta_2 = \frac{\pi}{2}(2m+1)$ (with $m = 0, \pm1, \pm2, ...$), then Equation 3.4 describes a circle. If either $E_1 = 0$ or $E_2 = 0$ or $\delta_1 - \delta_2 = m\pi$ (with $m = 0, \pm1, \pm2, ...$), then Equation 3.4 describes a line (Rohlfs and Wilson 1996). More generally, the orientation of the electric vector will change randomly with time and in this case the wave is unpolarized.

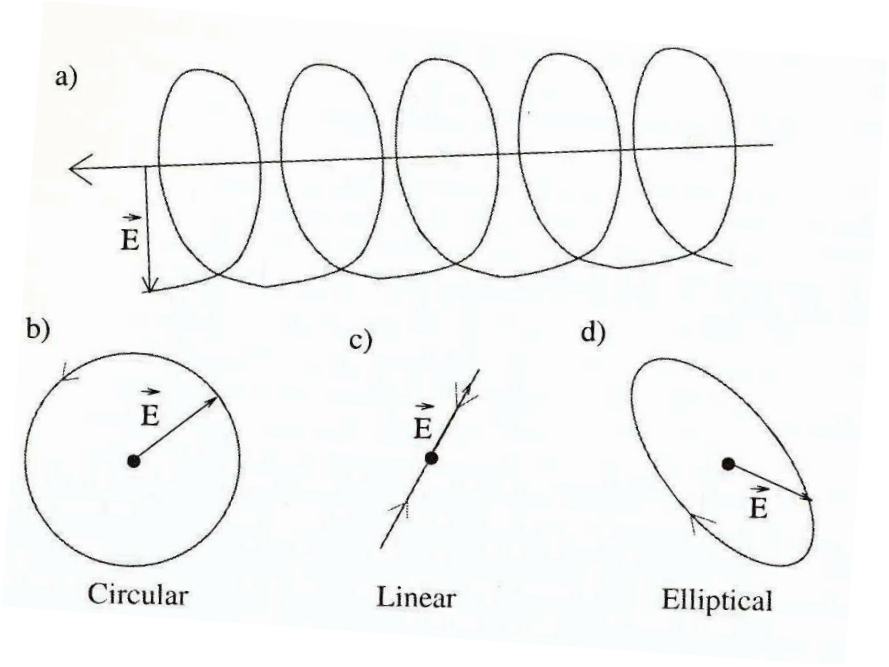

Figure 3.1: Figure (a): cartoon of the electric field component of a plane monochromatic electromagnetic wave propagating along the z direction. Panels (b), (c) and (d): movement of the tip of the electric vector drawn in (a) after having eliminated the term ωt and having held the term kz constant in the system of Equations 3.3 and representing respectively circular (b), linear (c) and elliptical (d) polarization states achieved by adjusting the phase terms δ_1 and δ_2 in Equation 3.3 (Cotton 1999).

In any of the cases above, the vector describing the electric field can be expressed as $\vec{\mathrm{E}} = E_x \cdot \hat{\imath} + E_y \cdot \hat{\jmath}$, where $\hat{\imath}$ and $\hat{\jmath}$ are unit vectors in the orthonormal base of $\mathbb{R}^2$ and E_x and E_y are the components of $\vec{\mathrm{E}}$ along the two axes described by $\hat{\imath}$ and $\hat{\jmath}$. In a simple antenna, two perpendicular dipoles lie along these two axes and define the so-called vertical and horizontal polarization states. Another simple antenna selects two perpendicular polarization states that are left circular polarization (LCP) and right circular polarization (RCP). Either system describes fully the electric field vector and are interchangeable without loss of information (Jackson 1998).

The radiation from radio astronomical sources is found to be either unpolarized or only weakly linearly polarized, which means that the radiation has either no statistical tendency or only weak statistical tendency to favour one of the two polarization states and, further, that its phase is random from one instant of time to the next.

3.2 Limitations of Geodetic VLBI: Atmosphere, Source Structure and Instrumental Effects

Group delay measurements are degraded by the presence of errors due to the ionosphere, the troposphere, the electronics of the telescopes and the structure of the source. These effects will be treated in the following sub-sections.

3.2.1 Ionosphere

The ionospheric contribution varies with frequency and changes with time of day, season and solar activity. The ionospheric contribution is dealt with by observing two widely-separated frequencies since

the ionospheric delay is proportional to the reciprocal of the second power of the frequency: $\tau_{\text{iono}} \propto \frac{1}{\nu^2}$ (Fomalont 1999).

3.2.2 Troposphere

The atmospheric contribution is of the order of 2.3 m (or 8 ns) at the zenith, of which 2.2 m are due to the dry constituents (mostly refraction due to oxygen and nitrogen molecules) and 0.1 m is due to water vapour. The atmospheric delay is estimated from the VLBI group delay measurements by fitting station-based atmospheric delay terms to the data in the form of approximately $\frac{Z}{\sin(E)}$, where Z is the zenith delay and E is the elevation angle (Carilli et al 1999).

3.2.3 Source Structure

Few sources are truly ideal point sources as required for geodesy when observed with the high resolution of VLBI (Gontier and Britzen 1994; Tornatore and Charlot 2007).

The effect of source structure on geodetic observables can be understood from the following considerations. It is possible to consider an extended source as sum of point-like sources, each of which produces a response in the correlator output that has a phase related to that component's position. The correlator performs a vectorial sum of all the visibility vectors from all the components of the source, each of which has a delay that differs slightly from that of a single point source at the core position resulting in a systematic delay measurement error.

The position of the source at the two frequencies used for geodesy has been seen during dedicated experiments to be different (Porcas 2009). This effect is not allowed for in present-day geodetic source position determinations leading to a small error that propagates into an error of the baseline length.

3.2.4 Instrumental Effects

Instrumental effects can degrade the delay determination by typically up to 17 ps (Rogers 1991), which is significant compared to the accuracy of the geodetic baseline length determination, presently of about 30 ps (1 cm) and is large compared to the target for VLBI 2010 of about 3 ps (1 mm) (Niell et al 2007). Instrumental effects that can degrade the correlator phases can be grouped into three categories: the error coming from the electronics, the error coming from the antenna and digital processing algorithmic approximations. Among the errors produced by the electronics are

- error caused by the filters, whose group delay varies with temperature,
- error caused by spurious signals, which are narrow-band signals coherent with the calibration signal used to detect and remove cable-related errors (phase cal) and having its same frequency,
- error caused by the saturation of the amplifiers, and
- error caused by the polarization leakage, which is a spurious signal entering in the signal path, but coming from the wrong polarization and since, as it will be described below, it is frequency dependent it contaminates the delay measurements.
- error caused by the algorithmic approximations, which are timing error in the correlator and quantization errors.

3.3 Polarization Leakage

The polarization leakage is described mathematically using a vector quantity called D-term, whose dimensionsless amplitude describes the fractional voltage leakage from one polarization into the other and

whose phase (in degrees) is due to the electrical length[1] of the leakage path.

The polarization leakage corrupts the true cross correlation leading to a measured cross correlation that differs from the true one and therefore the leakage corrupts the delay, as shown in figure 3.2.

The effect of polarization leakage on the parallel hand fringe visibility measurement[2] is given by the Jones matrix (Cotton 1999)

$$\begin{pmatrix} V_j^{\rm D}({\rm RCP}) \\ V_j^{\rm D}({\rm LCP}) \end{pmatrix} = \begin{pmatrix} 1 & D_j({\rm LCP}) \\ -D_j({\rm RCP}) & 1 \end{pmatrix} \begin{pmatrix} V_j({\rm LCP}) \\ V_j({\rm LCP}) \end{pmatrix} \tag{3.5}$$

where $j = 1, 2$ are the two antennas in the baseline, $V^D({\rm RCP})$ and $V^D({\rm LCP})$ are the complex time series of the voltage response of the antenna, including the leakage term from the other polarization, $V_i({\rm RCP})$ and $V_i({\rm LCP})$ are the complex uncontaminated time series and $D_i({\rm RCP}) = d_{\rm r}e^{i\phi_1}$ and $D_i({\rm LCP}) = d_{\rm l}e^{i\phi_2}$ are the D-terms, where $d_{\rm r}$ and $d_{\rm l}$ are the amplitude of the D-term and ϕ_1 and ϕ_2 are the phases of the D-terms. The second Equation of the matrix in 3.5 is analogous to the first Equation, but with opposite polarization. Since geodesy uses only RCP, I will continue describing the cross-correlation case for the RCP versus RCP.

After performing the parallel-hand cross correlation,

$$\langle V_1^{\rm D}({\rm RCP})V_2^{\rm D}({\rm RCP})\rangle = \langle V_1({\rm RCP})V_2({\rm RCP})\rangle + D_1D_2\langle V_1({\rm LCP})V_2({\rm LCP})\rangle \tag{3.6}$$

The cross terms $D_2({\rm LCP})\langle V_1({\rm RCP})V_2({\rm LCP})\rangle$ and $D_1({\rm RCP})\langle V_1({\rm LCP})V_2({\rm RCP})\rangle$ do not appear in Equation 3.6 as they equal zero for the source OQ 208 since it is unpolarized, causing $V_1({\rm RCP})$ and $V_2({\rm LCP})$ to be uncorrelated. Thus the effect on the visibility is second order in D_j and since the typical values of the D-term amplitude for this experiment range between 0.01 and 0.1 the effect of the leakage is quite small. Expanding Equation 3.6 using the phases and the amplitudes, following (Sorgente and Massi 1997)

$$\langle V_1^{\rm D}({\rm RCP})V_2^{\rm D}({\rm RCP})\rangle = v_1v_2e^{i(\psi_1-\psi_2)}[1 + D_1D_2^*e^{-2i(\psi_1-\psi_2)}] \tag{3.7}$$

where v_1 and v_2 are the voltage amplitudes, ψ_1 and ψ_2 are the parallactic angles of the source as seen from the two antennas and D is the D-term. The '*' represents the complex conjugate. The term of interest for geodesy is the visibility phase, but what is measured is corrupted by the presence of the D-term. The corrupting term in Equation 3.7 is the second term in square parentheses, and can be further expanded as

$$[D_1D_2^*e^{-2i(\psi_1-\psi_2)}] \approx (d_1d_2\cos[(\phi_1-\phi_2) - 2(\psi_1-\psi_2)])e^{id_1d_2\sin[(\phi_1-\phi_2)-2(\psi_1-\psi_2)]} \tag{3.8}$$

(Massi et al 1997). From Equation 3.8, it is possible to quantify the corrupting visibility phase rotation angle, θ_{12}, as

$$\theta_{12} = d_1d_2\sin[(\phi_1-\phi_2) - 2(\psi_1-\psi_2)] \tag{3.9}$$

where d_1 and d_2 are the amplitudes of the D-term respectively of antenna 1 and antenna 2 and ϕ_1 and ϕ_2 are the D-term phases. This is the angle that the visibility phases must be de-rotated to undo the effects of polarization leakage.

The leakage varies with frequency and so the corruption of the visibility phase varies with frequency which in turn corrupts the delay.

Among the errors produced by the antenna and the feed, the largest not yet corrected is produced by the polarization leakage. Under certain assumptions about feed performance, Rogers (1991) estimated

[1] To explain electrical length one can draw a parallel to multi-pathing in GPS, in which the signal enters the antenna along the direct line of sight and also along indirect lines of sight due to reflections off surrounding objects. The signal arriving along the reflected path has travelled a greater distance or equivalently has travel along a path with a greater electrical length and so comes in with a different phase relative to that of the signal arriving along the direct path

[2] Parallel hand fringe visibility is a VLBI termonology to describe the cross-correlation between the RCP-RCP signals and LCP-LCP signals. The cross-correlation between RCP-LCP and LCP-RCP is the measurement between cross hand fringe visibility.

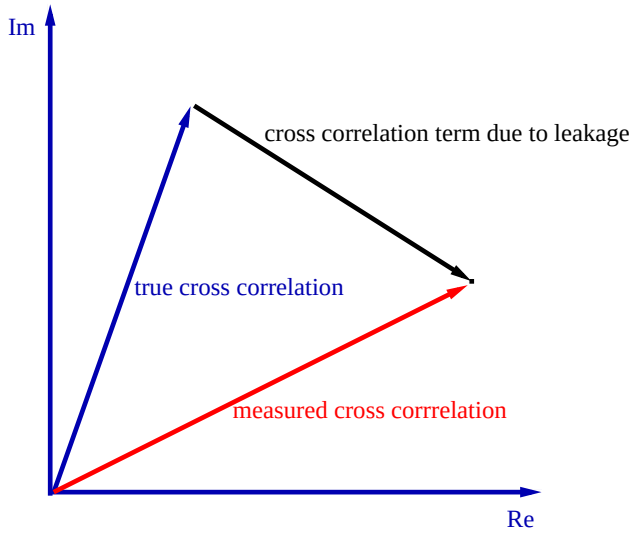

Figure 3.2: Plot of visibility in the real vs imaginary plane, for one scan. The vector labelled 'measured cross correlation' represents the measured visibility at the correlator, which is corrupted by the polarization leakage. The vector labelled 'cross correlation term due to leakage' is the leakage term. The vector labelled 'true cross correlation' is the true visibility - the one that is wanted.

a group delay measurement error from polarization leakage of the order of 14 ps. In contrast, the few values measured to date are typically in the range 2 ps to 9 ps at 8.4 GHz (X-band) (Corey and Titus 2006). Even at this lower level, the leakage error is still a major contributor, if not the dominant one, to the total instrumental error in geodetic VLBI.

3.4 Phase Closure

Before entering into the detail of the effects of polarization impurities on the geodetic observable, it is important to define the phase closure since they will be used in the later treatment. The signal coming from one antenna can be expressed in exponential form as V= $Ae^{i\gamma}$, where V is the signal in volt, A is the amplitude in volt and γ is the phase in radians (similar expressions hold for antennas B and C). If we consider a triangle of antennas, the cross-correlation products between the signals from each pair of antennas will be

$$\langle \mathrm{V}_A \cdot \mathrm{V}_B \rangle = ABe^{i(\gamma_\mathrm{A}-\gamma_\mathrm{B})} \tag{3.10}$$
$$\langle \mathrm{V}_B \cdot \mathrm{V}_C \rangle = BCe^{i(\gamma_\mathrm{B}-\gamma_\mathrm{C})} \tag{3.11}$$
$$\langle \mathrm{V}_C \cdot \mathrm{V}_A \rangle = CAe^{i(\gamma_\mathrm{C}-\gamma_\mathrm{A})} \tag{3.12}$$

where A, B and C represent the three different antennas, as illustrated in Figure 3.3. Considering the three baselines and considering only the cross-correlation phases of Equations 3.10, 3.11 and 3.12

$$\gamma_\mathrm{AB} = \gamma_\mathrm{A} - \gamma_\mathrm{B} \tag{3.13}$$
$$\gamma_\mathrm{BC} = \gamma_\mathrm{B} - \gamma_\mathrm{C} \tag{3.14}$$
$$\gamma_\mathrm{CA} = \gamma_\mathrm{C} - \gamma_\mathrm{A} \tag{3.15}$$

If I sum these baseline phases around the triangle, ABC, I obtain the closure phase

$$\gamma_\mathrm{AB} + \gamma_\mathrm{BC} + \gamma_\mathrm{CA} = (\gamma_\mathrm{A} - \gamma_\mathrm{B}) + (\gamma_\mathrm{B} - \gamma_\mathrm{C}) + (\gamma_\mathrm{C} - \gamma_\mathrm{A}) = 0 \tag{3.16}$$

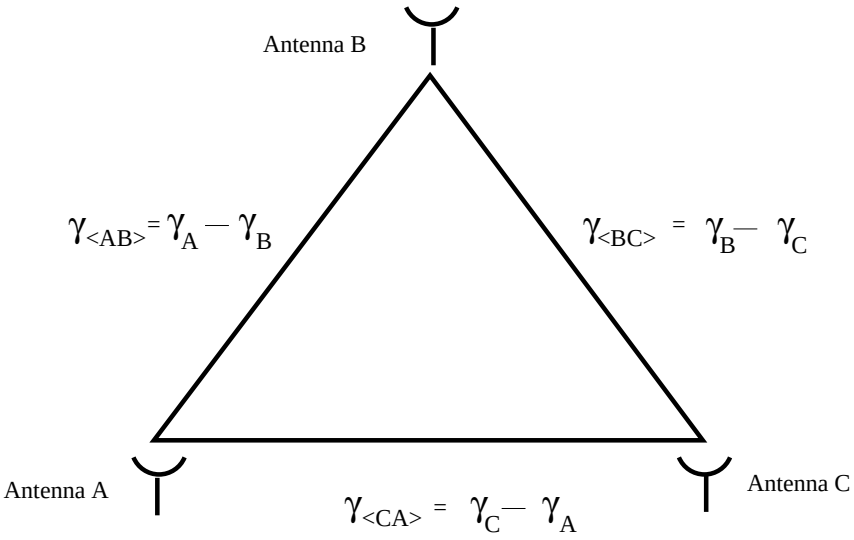

Figure 3.3: Schematic diagram illustrating phase closure.

from which one can see that all the station-based phase errors cancel in the closure because they contribute in a positive direction on one baseline and a negative direction on the other baseline. Station-based errors that close are, for example, atmosphere and clock offsets. Phase errors that do not close are caused by source structure, bandpass mismatch errors and polarization leakage. I will demonstrate now why the polarization leakage does not close since the determination of the leakage is the main goal of this thesis, and the same mathematics applies to non-closure due to source structure and bandpass missmatch. For simplicity I will consider an unpolarized source. Suppose that the observer wants to use only the signal coming from the right circular polarization (RCP) channel, then in the presence of leakage the signal can be expressed as

$$\mathrm{V} = V^{\mathrm{RCP}} + V^{\mathrm{LCP}} \tag{3.17}$$

where V^{RCP} is the signal and V^{LCP} is the unwanted polarization leakage coming from the left circular polarization (LCP). If neither, or only one of the antennas on a baseline is affected by the polarization leakage, then the cross-correlation coefficients will not be affected, but if two antennas are affected by leakage, then the closure phase will no longer be zero. To see this, suppose that the antenna signals are

$$\mathrm{V_A} = V_{\mathrm{A}}^{\mathrm{RCP}} + \vec{d}_{\mathrm{A}} \cdot V_{\mathrm{A}}^{\mathrm{LCP}} \tag{3.18}$$

$$\mathrm{V_B} = V_{\mathrm{B}}^{\mathrm{RCP}} + \vec{d}_{\mathrm{B}} \cdot V_{\mathrm{B}}^{\mathrm{LCP}} \tag{3.19}$$

$$\mathrm{V_C} = V_{\mathrm{C}}^{\mathrm{RCP}} + 0 \cdot V_{\mathrm{C}}^{\mathrm{LCP}} \tag{3.20}$$

where $\vec{d}_{\mathrm{A}}$ and $\vec{d}_{\mathrm{B}}$ are the vectors describing the non-zero leakage terms respectively for antenna A and B (D-terms). In this example I assume that antenna C has no polarization leakage (i.e. $\vec{d}_{\mathrm{C}} = 0$). The cross-correlation product between antennas A and B is

$$\langle \mathrm{V_A} \cdot \mathrm{V_B} \rangle = \langle V_{\mathrm{A}}^{\mathrm{RCP}} \cdot V_{\mathrm{B}}^{\mathrm{RCP}} \rangle + \langle V_{\mathrm{A}}^{\mathrm{RCP}} \cdot \vec{d}_{\mathrm{B}} \cdot V_{\mathrm{B}}^{\mathrm{LCP}} \rangle + \langle V_{\mathrm{B}}^{\mathrm{RCP}} \cdot \vec{d}_{\mathrm{A}} \cdot V_{\mathrm{A}}^{\mathrm{LCP}} \rangle + \langle \vec{d}_{\mathrm{A}} \cdot V_{\mathrm{A}}^{\mathrm{LCP}} \cdot \vec{d}_{\mathrm{B}} \cdot V_{\mathrm{B}}^{\mathrm{LCP}} \rangle \tag{3.21}$$

of which:

$$\langle V_{\mathrm{A}}^{\mathrm{RCP}} \cdot V_{\mathrm{B}}^{\mathrm{RCP}} \rangle \tag{3.22}$$

is the true cross-correlation and

$$\langle V_{\mathrm{A}}^{\mathrm{RCP}} \cdot \vec{d}_{\mathrm{B}} \cdot V_{\mathrm{B}}^{\mathrm{LCP}} \rangle = \langle V_{\mathrm{B}}^{\mathrm{RCP}} \cdot \vec{d}_{\mathrm{A}} \cdot V_{\mathrm{A}}^{\mathrm{LCP}} \rangle = 0 \tag{3.23}$$

because there is no statistical coherence between RCP and LCP channels, but

$$\langle \vec{d}_{\rm A} \cdot V_{\rm A}^{\rm LCP} \cdot \vec{d}_{\rm B} \cdot V_{\rm B}^{\rm LCP} \rangle \neq 0 \tag{3.24}$$

Equation 3.21 can be written for every permutation of the three antennas. Considering only the phases, from Equation 3.21 I have

$$\gamma_{\langle \rm AB \rangle} = \gamma_{\langle \rm AB \rangle}^{\rm RCP} + \phi_{\langle \rm AB \rangle}^{\rm leak} \tag{3.25}$$

$$\gamma_{\langle \rm AC \rangle} = \gamma_{\langle \rm AC \rangle}^{\rm RCP} \tag{3.26}$$

$$\gamma_{\langle \rm BC \rangle} = \gamma_{\langle \rm BC \rangle}^{\rm RCP} \tag{3.27}$$

where the phase labelled 'leak' is the unwanted contribution from the leakage term. Equations 3.26 and 3.27 do not carry any leakage terms because antenna C is leakage free. The closure phase is non zero leading to an error in the determination of the group delay. This demonstration holds also for the signals coming from the LCP channel and leaking into the RCP channel. Each phase measurement on each baseline gives a position circle on the sky on which the source lies (this concept is similar to that for GPS, or sextant position determination except that the position circle is on the Earth instead of on the sky). The circles should intercept at a point that corresponds to the source position, but if non-closing errors are present, then one or more of the circles will be slightly displaced from the correct position causing the intersection not to occur at a point but rather in a position triangle whose area represent a position uncertainty of the source which propagates into an error in the baseline length.

Effects that produce station based offsets and close around a triangle do not affect the position triangle since they are estimated during the geodetic analysis during the fit for the clock offset (see Figure 2.2). The effect of polarization leakage does not close around a triangle and so it cannot be absorbed in the estimate of the clock offset and needs to be corrected. The lack of corrections would lead to systematic errors.

3.5 Polarizers and their Effects on the Geodetic Observables

VLBI, like most forms of interferometry, needs to preserve both the phase and the amplitude of the incoming radiation to perform a measurement (Thompson et al 2001a). In radio astronomy there are several kinds of receiving systems that can be used. Some of these systems preserve only the amplitude information of the incoming radiation (like the bolometers), and some others preserve both amplitude and phase of the incoming radiation (like a dipole antenna). Like GPS antennas, also VLBI antennas couple the radiation coherently to the amplifiers and receiver.

A dipole responds to linear polarization (Hertz 1889), therefore by using only one dipole, one would receive in general only part of the incoming electric field. By using two dipoles, one can reconstruct the whole information of the incoming electric field, and so maximize the signal-to-noise ratio (SNR).

Since any device that separates out two polarization states is called a polarizer, the case of two dipoles is the most simple form of polarizer that one can build.

However, the linear polarizer is not well suited for VLBI because dipoles at a station are generally not parallel to the dipoles at another distant station (Figure 3.4). The lack of parallelism causes loss of SNR in the cross-correlation. To avoid this situation, VLBI uses circular polarization (CP) instead, since the lack of parallelism introduces simply a phase rotation of the cross-correlation coefficients, which can be removed in the post-correlation data analysis.

One out of the various kinds of polarizers in use in VLBI is the septum polarizer. I will, for simplicity, consider the incoming radiation as pure RCP, thus having the same amplitude in the x and y directions and a 90° phase shift between the x and the y component of the wave. The wave encounters the septum polarizer, which contains a metal fin within the waveguide as shown in Fig. 3.5. The component of the electric field perpendicular to the fin (E_x) is divided, due to the boundary conditions on the conducting

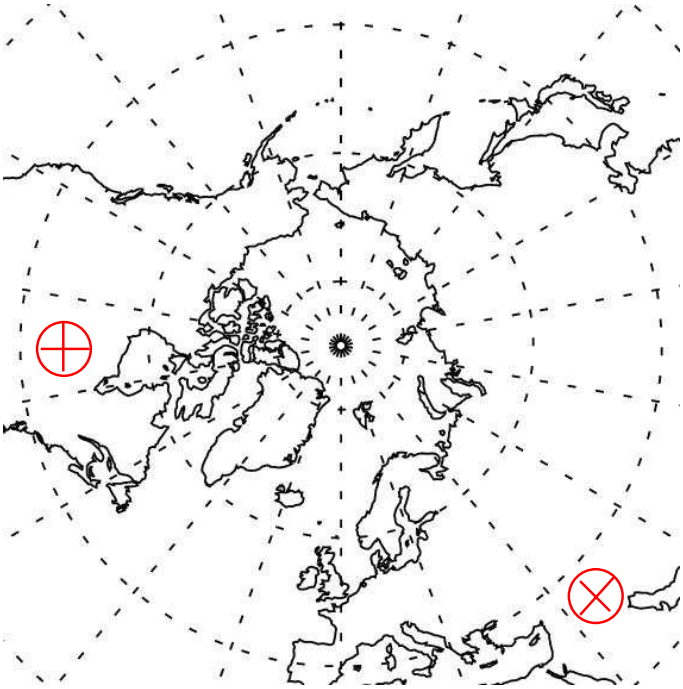

Figure 3.4: Sketch of two fictitious telescopes (red circle) and their dipoles (red perendiculars lines) as seen from an observer located in space. Linear dipoles will generally not remain parallel throughout the array (unless the dipoles can be rotated axially).

fin, into two electric field regions which have the same intensity and orientation as E_x. The component of the electric field parallel to the fin (E_y) is divided, due to the boundary conditions on the conducting fin, into two electric field regions which have the same intensity as E_y but the orientations are rotated into the horizontal plane in the clockwise direction in one region and in the counterclockwise direction in the other region. The phase velocities of the E_x and E_y components differ from each other while propagating from the polarizer input to the dipole because the septum divides the waveguide into regions that have different dimensions in the x and y directions (x is halved, y remains the same). These dimensions and the length of the septum are chosen to introduce a 90° phase shift between the E_x and E_y components. When those fields (i.e. E_x and the rotated E_y fields with 90° phase shift) superimpose at the dipoles, they interfere constructively at one dipole and destructively at the other dipole. This logic can be repeated for pure LCP and the output power will appear at the other dipole. The general case is a mixture of RCP and LCP input, which will be separated to produce outputs on both dipoles. In the real case, a band of frequencies is observed and, as developed in Fig. 3.6, the theoretical phase difference inserted by the polarizer between the two linear polarizations measured at one dipole output is an accurate 90° at only two frequencies. In this broad-band case, the septum polarizer will not separate the two polarizations with perfect purity at most frequencies and some contamination from the unwanted polarization will add algebraically to the signal.

The effect of leakage is to perturb the visibility phase in one polarization with a small amount of signal leaking from the other polarization. The leakage and hence the phase perturbation is frequency dependent and so perturbs the delay (Equation 3.28). For reference, delay is related to phase and frequency by:

$$\tau = \frac{d\phi}{d\nu} \tag{3.28}$$

where τ is the group delay in second, ϕ is the phase in turns and ν is the frequency in hertz.

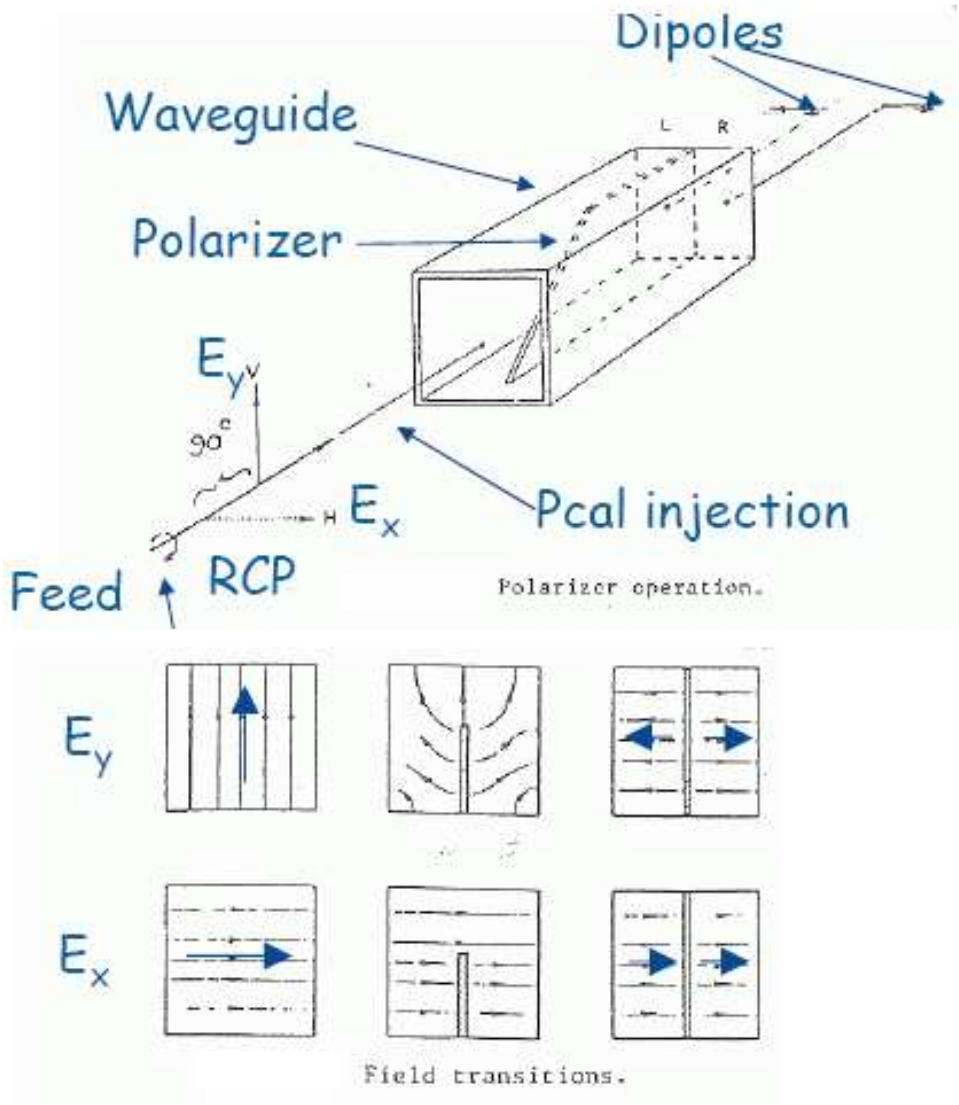

Figure 3.5: Top: schematic diagram of a septum polarizer. Bottom: the field pattern in cross section across the septum polarizer at the input, half way and at the output, courtesy of S. Srikanth.

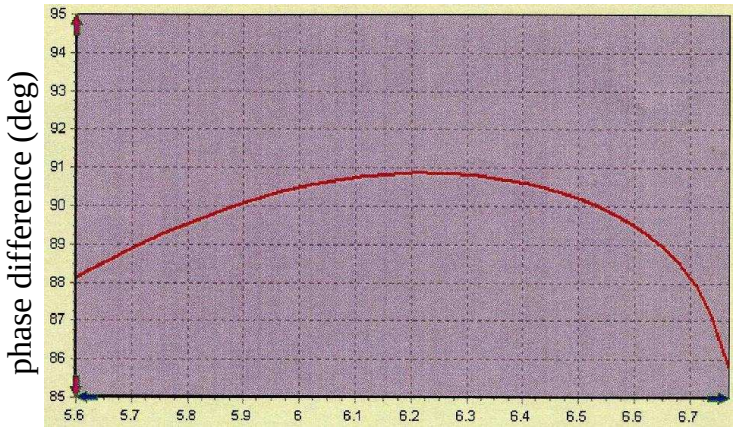

Figure 3.6: Modelled phase response of an MPIfR septum polarizer vs frequency, courtesy R. Keller. The figure shows the difference in phase length between input and output for the x and y fields, that is the relative phase of the E_x and rotated E_y field components at the output dipole, given E_x and E_y fields injected in phase with each other at the polarizer input. A perfect system should deliver a constant 90°, however deviations of up to 4° are caused by the changing wavelength across the band causing an imperfect 90° phase shift. The curvature allows one to optimize the design to produce a 90° phase shift at two frequencies. The largest fractional bandwidth achievable with such polarizer is 16 %.

3.6 How to Measure the Leakage

Leakage is detected by the following procedure. In the absence of leakage the signals received in the LCP channel and RCP channel are uncorrelated Gaussian noise processes and cross correlation between them will yield no coherence. If leakage is present then some of the signal in one polarization channel will add to the signal in the other polarization channel. By cross-correlating the contaminated LCP channel at one antenna and the contaminated RCP channel at the other antenna one will find coherence caused by the LCP in the LCP channel correlating against the LCP that leaked into the RCP channel at the other antenna.

To disentangle the intrinsic polarization of a source and the polarization leakage terms, one needs a wide parallactic angle coverage because the electric vector intrinsic to the source will not rotate as the dipoles rotates whilst the vectors describing the leakage terms will rotate with the dipoles. The parallactic angle is explained in Figure 3.7.

In the case of unpolarized sources, the argument above is not so important, as there is no source polarization to be disentangled from the polarization leakage.

Geodetic stations mostly have only RCP, but measurements of the leakage for these stations are still possible if the antenna at the other end of the baseline has dual-polarization receivers. Therefore, I used the 10 VLBA antennas since they are among the few antennas that have dual polarization capability at S-band and X-band and their hardware is carefully designed for VLBI observation plus 10 geodetic antennas to measure the polarization leakage. Correlation was performed between all possible combinations of polarization (i.e. RCP against RCP, LCP against LCP, RCP against LCP and LCP against RCP). The appearence of the leakage in the data and the method used to correct for them will be given in the chapter Data Reduction.

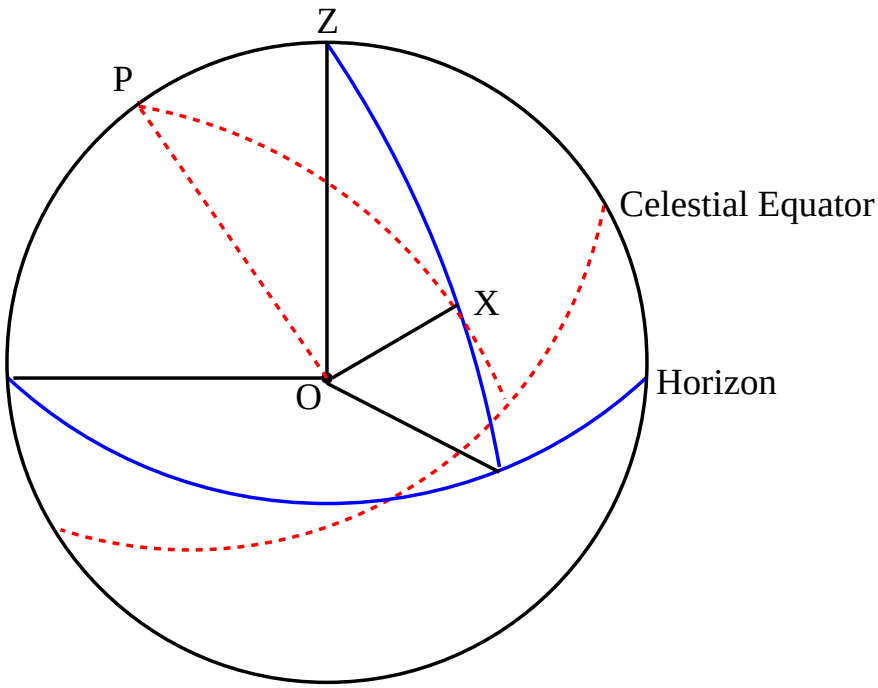

Figure 3.7: The parallactic angle is the angle $P\hat{X}Z$ and is the angle between the line joining the source to the north celestial pole (P) and the line joining the source to the zenith at the antenna (Z) where O is the observer and X is the source on the celestial sphere. The parallactic angle varies as the Earth rotates.

Chapter 4

Observation to Measure the Leakage

4.1 Project Overview

To measure the leakage characteristic, one needs dual-polarization receivers, as explained in the previous chapter, and to achieve that I used the VLBA antennas. To use the VLBA antennas one must write an observing proposal, containing a detailed explanation of why the observation is scientifically relevant, a plan of how the observation must take place, and which results can be drawn from the observation. This proposal undergoes external review, and only if the four referees agree on the scientific relevance of the project and robustness of the observing technique, the observing time is granted. Requests for usage of the geodetic antennas are addressed to the international VLBI service (IVS) observing programme committee. I wrote an observing proposal for time on the VLBA and IVS antennas and it was granted 24 hours.

The proposal's aim was to measure the D-term variations over the wide X-band and the 2.3 GHz band (S-band) for both IVS and VLBA antennas. I proposed to observe 10 sources during the 24 hours, of which two main target sources were to measure the D-terms (one for the first 12 hours and one for the second 12 hours), five backup target sources in case the first two did not deliver usable data and three polarization position angle-calibrators. The position angle calibrators have known polarization position angle and are required for calibrating the absolute phase offset between the two polarization channels at the stations, if one wants to study source intrinsic polarization. The aim of this project, which was called RD0705, was to measure polarization leakage, therefore I needed only the relative phase offset between the two polarization channels and not the absolute phase offset. Nevertheless those sources were observed for future possible study on the polarization of the target sources. Twelve hours per main target source are required for sampling a wide range of parallactic angles. Although RD0705's target sources were selected to be unpolarized, I nevertheless scheduled complete parallactic angle coverage to encompass the possibility that the target sources turned out to have detectable linear polarization, in which case having the measurements span a range of parallactic angle would permit the separation of leakage effects from source polarization effects.

The frequency scheme selected was to use 8 MHz baseband filters for both sidebands (for a total of 16 MHz per BBC), dual polarization (at the VLBA stations), and a total of eight BBCs (since that is the number of BBCs available at each VLBA station). Thus I could observe eight frequencies and two polarizations simultaneously: four BBCs were connected to the RCP channel and, in the case of the VLBA, four BBCs were connected to the LCP channel. For the Mark IV stations all the eight BBCs used were connected to the RCP channel and their frequencies were set to be the same as the VLBA stations. I proposed to sample completely the 720 MHz radio frequency (RF) bandwidth at X-band and 140 MHz RF bandwidth at S-band since these bandwidths are the ones spanned in the wide-band geodetic experiments. This could be done using nearly 60 frequencies spaced 16 MHz apart in X-band

and 10 MHz apart in S-band for a total of 15 frequency setups each of which observed four frequencies at a time.

I proposed only a single epoch observation since time variability of the D-terms is not expected and indeed leakage has been found to be stable over a period of 1.3 years (Gomez 2002). Further, data from some VLBA monitoring programs suggest that the D-terms do not change much unless, station hardware is changed.

I proposed to use the antennas listed in Table 4.1. This proposal was accepted and the observation took place on day 11 of July, 2007.

The locations of the stations is shown in Figure 6.5.

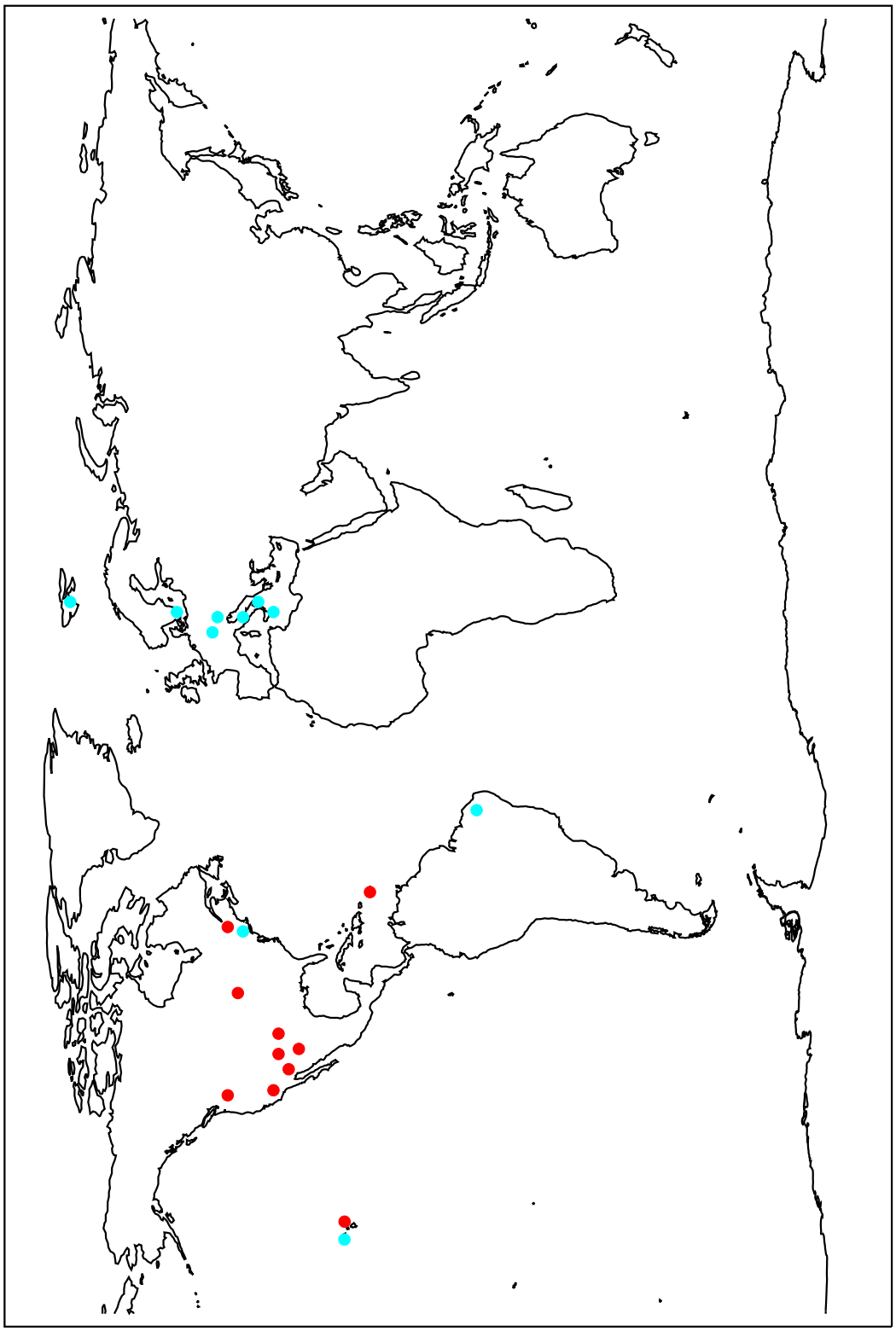

Figure 4.1: Station locations for those stations involved in RD0705. The red dots represent the VLBA antennas and the cyan dots represent the geodetic antennas.

antenna name	Location	DAR	Network
Pie Town (Pt)	New Mexico	VLBA	NRAO
Los Alamos (La)	New Mexico	VLBA	NRAO
Brewster (Br)	Washington	VLBA	NRAO
Fort Davies (Fd)	Texas	VLBA	NRAO
Saint Croix (Sc)	Virging Islands	VLBA	NRAO
North Liberty (Nl)	Iowa	VLBA	NRAO
Owens Valley (Ov)	California	VLBA	NRAO
Mauna Kea (Mk)	Hawaii	VLBA	NRAO
Hanckock (Hh)	New Hampshire	VLBA	NRAO
Medicina (Mc)	Italy	Mark IV	EVN, IVS
Noto (Nt)	Italy	VLBA4	EVN, IVS
Onsala60 (On)	Sweden	Mark IV	EVN, IVS
Effelsberg (Eb)	Germany	Mark IV	EVN
Wettzell (Wz)	Germany	Mark IV	IVS
Kokee (Kk)	Hawaii	VLBA4	IVS
Fortaleza (Ft)	Brazil	Mark IV	IVS
Matera (Ma)	Italy	Mark IV	IVS
Westford (Wf)	New Hampshire	Mark IV	IVS
Ny Alesund (Ny)	Svalbart Islands	Mark IV	IVS

Table 4.1: Antennas that were planned in RD0705, their data acquisition rack and the network for which the antennas observe.

Chapter 5

Scheduling, Observation and Correlation

5.1 Chapter Overview

In this chapter I will explain in detail how the VLBI observation are planned, observed and correlated. Figure 5.1 shows graphically the process steps.

5.2 Concept of Scheduling

To prepare a radio astronomical observation using VLBI, it is required to produce a schedule file containing the information needed by the telescope operators and the telescope control computers to conduct the observation. The schedule file is produced using either the NRAO *sched* (Walker 2009) or the IVS *sked* (Vandenberg 1999) program. The schedule file contains important information about the sources to be observed and technical setup information tailored to the individual antennas. The following issues must be considered when preparing the schedule.

- Source selection: target sources and calibrators must be visible at all the stations simultaneously.
- Time of the observation: all astronomical objects rise and set at different times for observers at different locations on the Earth, and therefore they are not always visible to the telescopes and not necessarily simultaneously.
- Source coordinates: the Earth precession and nutation causes the apparent source coordinates to change and therefore the coordinates must be given at a defined epoch[1] and need to be as precise as possible (ideally to the milliarcsecond) to provide a priori accurate information for the correlator. The coordinate system used is equatorial (right ascension (RA) and declination (dec)).
- Length of the observation: how long should the telescopes observe each source? This is a fundamental issue to guarantee that one detects the observed source: if the integration time chosen is too short, this can lead, together with other factors, to low SNR or even to non-detections. This requires the calculation of minimum flux density (expressed in the unit of jansky, 1 Jy $= 10^{-26} \frac{\mathrm{W}}{\mathrm{Hz \cdot m^2}}$) that can be detected on a single baseline. The minimum flux density depends on the sensitivity of the antennas, which in turn depends on the collecting area of the antennas, the thermal noise from the first amplifier and from the environment and from the bandwidth and the number of bits

[1] e.g. J2000: source positions are given at the date of the 1st of January 2000 and are precessed to the date of observation using a defined precession and nutation model

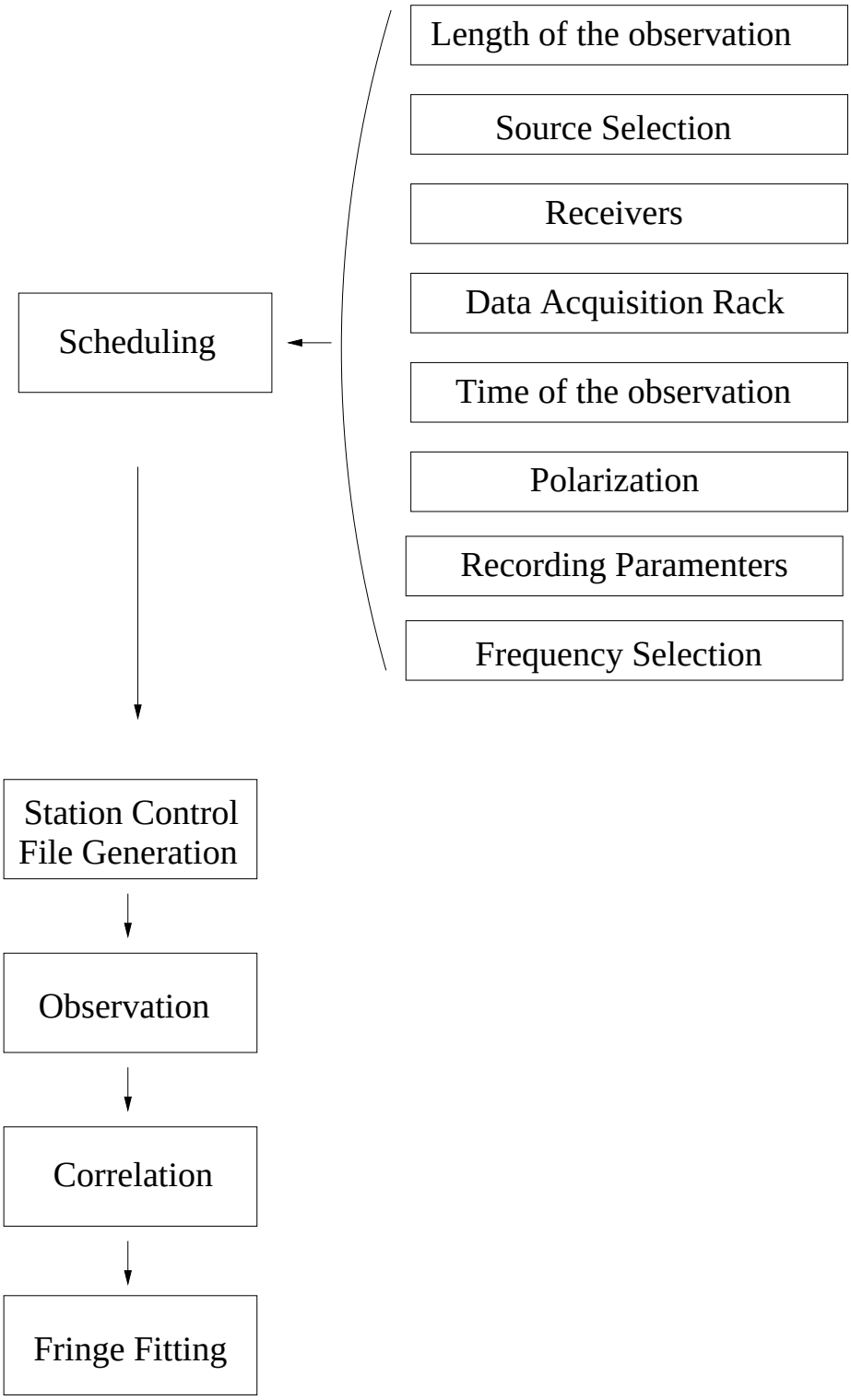

Figure 5.1: Cartoon describing the work flow described in this chapter.

recorded. The sensitivity of an antenna is conveniently expressed in terms of its system equivalent flux density (SEFD). This parameter is well known and is tabulated for each station.

- Repetition and order of the observation on selected sources: how many times will the telescopes observe each source during the period of the whole observation.
- Receivers. The frequency bands that can be observed are generally not the same at all stations since, by their design, some receivers have narrower bandwidth or different centre frequency than others.
- Data Acquisition Rack. The most commonly used rack types are presently the VLBA, the Mark IV, the hybrid VLBA4 and the K5. These racks have differences in detail that need to be taken into account while scheduling. Specifically, the various racks can have a different number of frequency channels that can be observed simultaneously, the way they are connected via IF cables to the front-end is sometimes under software control and at other times requires reconnecting cables by hands (re-patching). In addition the bandwidth capabilities can differ and need to be known.
- Polarization. Some receivers have the possibility of observing dual polarizations simultaneously and others not. The schedule must specify which polarization mode is intended to be used (right circular, left circular or both).
- Recording parameters. The sample rate and the number of bits per sample (one or two) must be selected. These parameters influence the sensitivity and the amount of recording media that needs to be sent to the stations for the observations.

Most of the information about station sensitivities, equipment capabilities, source positions and source strengths is collected in regularly updated catalogues that are part of the *sched* or *sked* packages. Still, the design of the experiment, including selections of the desired parameters is done by the observer.

5.3 Generation of the Schedule File for RD0705

To obtain the best results possible, I pushed the Mark IV stations beyond their standard usage. This effort cost a huge amount of thinking, required some extension to *sched* and testing with the help of Wettzell and Medicina before a working schedule file was produced. The preparation of the file required a deep understanding of the VLBI data acquisition racks and their capabilities. The process of preparing a schedule file requires in the worst case, about two days. The schedule of RD0705 demanded two months of intense work with the support of highly qualified astronomers and geodesists. The preparation of the key file[2] which is normally done by hand editing, was only feasible, due to its complexity and length, by writing dedicated C-programs.

5.3.1 Hardware Constraints

The production of the schedule file was made quite complicated by some tuning limitations and constraints in connecting IF cables to the BBCs (patching) at both the VLBA and geodetic antennas. Whilst the geodetic stations have 14 BBCs, the VLBA antennas are limited to eight BBCs and I paired those at the same frequency, to get both hands of polarization (four LCP and four RCP). Instead of using only four BBCs at the geodetic stations, since they can observe only RCP, I used all 14 for simplicity of scheduling, providing redundant frequency coverage as backup in the case of a BBC problem, though with the risk of increased crosstalk between BBCs, in which the signal of one BBC is contaminated by a spurious signal induced by the neighbouring BBC tuned at the same frequency. An example of how the VLBA and Mark IV BBCs were paired is shown on Figure 5.2

[2] input file for *sched* containing the frequency settings, LO tuning, the sources and scan lengths

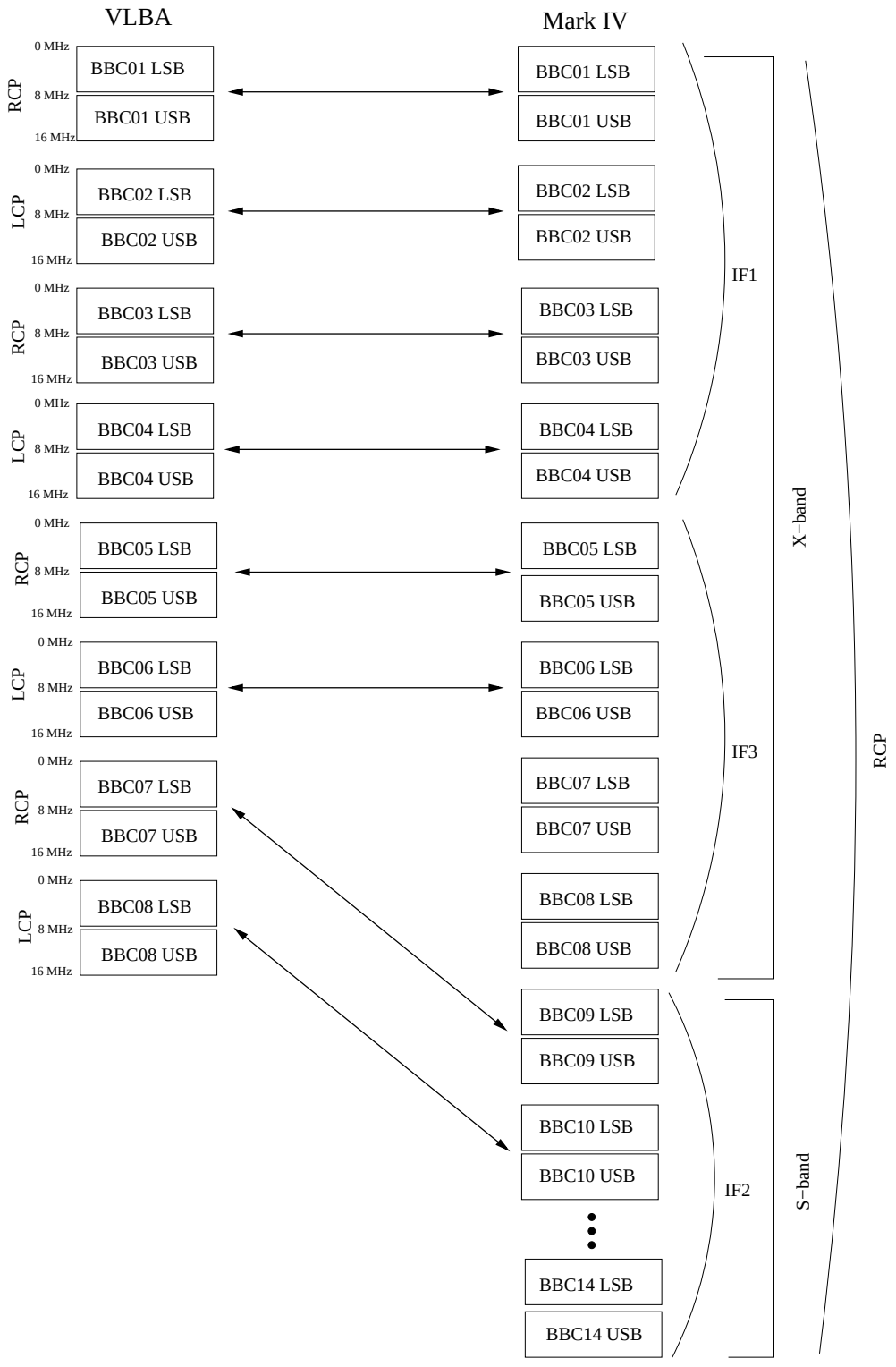

Figure 5.2: Cartoon describing how the VLBA and Mark IV BBCs were paired in one of the setups. For every setup, depending on the tunability of the BBCs at the Mark IV stations, the BBC paring changed as is described in Tables 5.3.2 and 5.3.2. Left: VLBA BBCs. The frequency agility of the VLBA permit to patch all the four IFs to all the BBCs. The selection is done by the scheduler and is controlled by the antenna software and can change while observing. Right: Mark IV BBCs. The Mark IV do not have the same capability as the VLBAs. The patching can be changed, but require manual intervention, therefore is not doable during an observation.

The ellipsoidal reflector that enables simultaneous S-band and X-band observing at the VLBA stations remains deployed only when at least one BBC is tuned to X-band and at least one BBC is tuned to S-band, otherwise it is automatically retracted by the station control software. Thus, I needed to observe with at least one BBC in each band at all times. The retraction of the ellipsoidal reflector would have changed the optical properties of the signal path and therefore would have changed the leakage characteristic between the setups in this experiment biasing the results.

The Mark IV data acquisition racks have three IF inputs, each with their own band-limiting filters (Clark and Rogers 1982 and Corey and Clark 1991) that leave a gap between 8580 MHz and 8680 MHz that cannot be observed.

To have a SNR as high as possible, I observed the first 12 h at 512 Mbit/s with 2 bit sampling and switched among the 15 frequency setups. Clearly observations done at 1 GB/s would lead to even higher SNR, but presently the VLBA antennas are not capable of such a high data rate. This configuration had never been used for geodetic experiments prior to this observation and, although the data acquisition rack and receivers at the geodetic antennas are nominally capable of observing such mode, it had never been tested before. Therefore, prior to the observation, I asked the stations to test whether the BBC LOs remained coherent with the station hydrogen maser (i.e. the BBCs were locked) when generating the required frequencies. The second 12 h were observed using the frequencies used for the weekly geodetic experiments conducted for calculating the earth orientation parameters (so called R1 sessions) at 256 Mbit/s, 1 bit sampling, which could be observed by switching among four frequency setups. The change of strategy was forced on me because I did not know that the VLBA had granted us 24 hours until after the recording media were sent to the stations. Therefore I had to reduce the total number of bits recorded to fit the last 12 hours on the available media. The change in recording speed and bit sampling gave confidence that, had the first 12 hours not been usable due to the very complicated setups, I still would have had 12 hours of good data recorded in the usual way that the geodetic antennas perform routine geodetic sessions.

5.3.2 Frequency Selection

Nearly 60 frequencies spaced 16 MHz apart in X-band and 10 MHz apart in S-band needed to be observed to sample completely the 720 MHz RF bandwidth at X-band and 140 MHz at S-band with three frequency channels in X-band and one frequency channel in S-band due to the constraints mentioned in the previous paragraph.

Those were observed four at a time in parallel leading to the set of 15 frequency sequences in Tables 5.3.2, 5.3.2 and 5.3.2. Those satisfied the frequency and patching limitations at the Mark IV sites and required no manual cable re-patching between sequences. Table 5.3.2 lists the observed X-band frequencies and, for each one, which IFD or IF3 output can supply the IF signal in a Mark IV system. The frequencies listed in Table 5.3.2 have the following properties.

- Cover 8212.99 MHz to 8932.99 MHz, which is the frequency span of the so-called geodetic wideband sequence.
- Space frequencies 16 MHz apart, and record both 8-MHz bandwidth sidebands.

Tables 5.3.2 and 5.3.2 give the frequency sequences, including BBC assignments respectively for the VLBA and Mark IV sites. The features of the sequences are as follows.

- First LO frequency changes are required only at the VLBA since some of the Mark IV stations do not have this capacity.
- At the Mark IV sites, all frequencies satisfy the restrictions imposed by the standard geodetic patching, as outlined in the Table 5.3.2.

- Need to observe three X-band and one S-band frequency per frequency sequence as required to keep the VLBA dichroic mirror deployed.
- To cover 8212.99 MHz to 8932.99 MHz completely requires $720/16 = 45$ individual frequencies, or 15 sequences. I dropped one of the frequencies not accessible at the Mark IV stations (namely, 8628.99 MHz) and added in its place the frequency 8932.99 MHz.
- At the two sites with VLBA4 racks (Kokee Park and Noto) the same BBC frequency assignments were used as at the Mark IV sites. However, Noto X-band receiver is, by design, narrowband, so it could not observe frequencies above 8484.99 MHz.
- At the non-VLBA sites, every frequency was observed using two or more BBCs, to provide redundancy in the event of a BBC problem. Crosstalk may be an issue when many BBCs are at the same frequency, in which case it may be better to reduce to no more than two BBCs at the same frequency (Walker 2007, private communication).

For S-band, I had 15 frequencies spaced 10 MHz apart, accepting an overlap in frequency between settings, spanning 2225.99 MHz to 2365.99 MHz with dual, 8-MHz-bandwidth sidebands and with repetition of 2325.99 MHz. The total frequency span did not completely cover the standard geodetic frequencies. The frequency setup used by the geodetic experiments conducted for measuring the intra-European plate stability go down to 2212.99 MHz, and the frequency sequence for the research and developement sessions made using the VLBA antennas goes up to 2372.99 MHz, whereas the lowest and highest frequencies in this experiment were 2221.99 MHz and 2369.99 MHz. The S-band frequencies observed covered also the frequencies used by digital audio satellites (whose frequencies lie between 2320 MHz and 2345 MHz), which caused strong radio frequency interference (RFI).

5.3.3 Source Selection

Target sources were OQ 208 and 3C 84 as they are known to be nearly unpolarized (Stanghellini et al 1996, Jackson et al 2007). In addition I selected a few circumpolar sources as backup sources for measuring the D-terms. In this way I had a good parallactic angle coverage at both the VLBA and the European stations. I selected also two sources at low declination for visibility from Fortaleza (coordinates $3°46'$ S $38°34'$ W, Brazil). The sources that were used for this experiment, their flux densities and their coordinates are reported in Table 5.3.3. The mutual coverage of the main target sources at the various sites, their elevations as a function of the universal time (UT) and the parallactic angle coverage in function of UT calculated by *sched* for the epoch of the observation are shown in Figure 5.3 and Figure 5.4. This exercise was done to check whether the selection of the sources was good, and was repeated for all the sources reported in Table 5.3.3.

By looking at the plots shown in the right panels of Figure 5.3, I decided to observe OQ 208 between 19:00 UT and 04:19 UT and to observe 3C 84 between 09:40 UT and 16:18 UT. Both sources had a good parallactic angle coverage, as shown in Figure 5.4.

BBC 1-2	IF1 low	8180 MHz to 8300 MHz
BBC 3-4	IF1 high	8300MHz to 8580 MHz
BBC 5-8	IF3	8680 MHz to 8980 MHz or 8280 MHz to 8580 MHz
BBC 9-10	IF2 low	2120 MHz to 2240 MHz
BBC 11-14	IF2 high	2240 MHz to 2520 MHz

Table 5.1: Geodetic patching at the Mark IV stations.

Freq	Mark IV station accessibility
8212.99 MHz	IF1 low
8228.99 MHz	IF1 low
8244.99 MHz	IF1 low
8260.99 MHz	IF1 low
8276.99 MHz	IF1 low or IF3
8292.99 MHz	IF1 low or IF3
8308.99 MHz	IF1 high or IF3
8324.99 MHz	IF1 high or IF3
8340.99 MHz	IF1 high or IF3
8356.99 MHz	IF1 high or IF3
8372.99 MHz	IF1 high or IF3
8388.99 MHz	IF1 high or IF3
8404.99 MHz	IF1 high or IF3
8420.99 MHz	IF1 high or IF3
8436.99 MHz	IF1 high or IF3
8452.99 MHz	IF1 high or IF3
8468.99 MHz	IF1 high or IF3
8484.99 MHz	IF1 high or IF3
8500.99 MHz	IF1 high or IF3
8516.99 MHz	IF1 high or IF3
8532.99 MHz	IF1 high or IF3
8548.99 MHz	IF1 high or IF3
8564.99 MHz	IF1 high or IF3
8579.99 MHz	IF1 high or IF3 **
8596.99 MHz	Not accessible
8612.99 MHz	Not accessible
8644.99 MHz	Not accessible
8660.99 MHz	Not accessible
8676.99 MHz	Not accessible
8692.99 MHz	IF3
8708.99 MHz	IF3
8724.99 MHz	IF3
8740.99 MHz	IF3
8756.99 MHz	IF3
8772.99 MHz	IF3
8788.99 MHz	IF3
8804.99 MHz	IF3
8820.99 MHz	IF3
8836.99 MHz	IF3
8852.99 MHz	IF3
8868.99 MHz	IF3
8884.99 MHz	IF3
8900.99 MHz	IF3
8916.99 MHz	IF3
8932.99 MHz	IF3

Table 5.2: X-band frequency coverage of RD0705, listing the 45 X-band frequencies that satisfy the constraints given in the text along with the Mark IV rack IF input(s) that can supply each frequency. The frequency marked with '**' should be 8580.99 MHz to conform to 16 MHz spacings. However it is not accessible at Mark IV stations as it would require the BBC LO to be set to 500.99 MHz which is above their maximum frequency of 500 MHz. Instead 8579.99 MHz is accessible and is only 1 MHz lower.

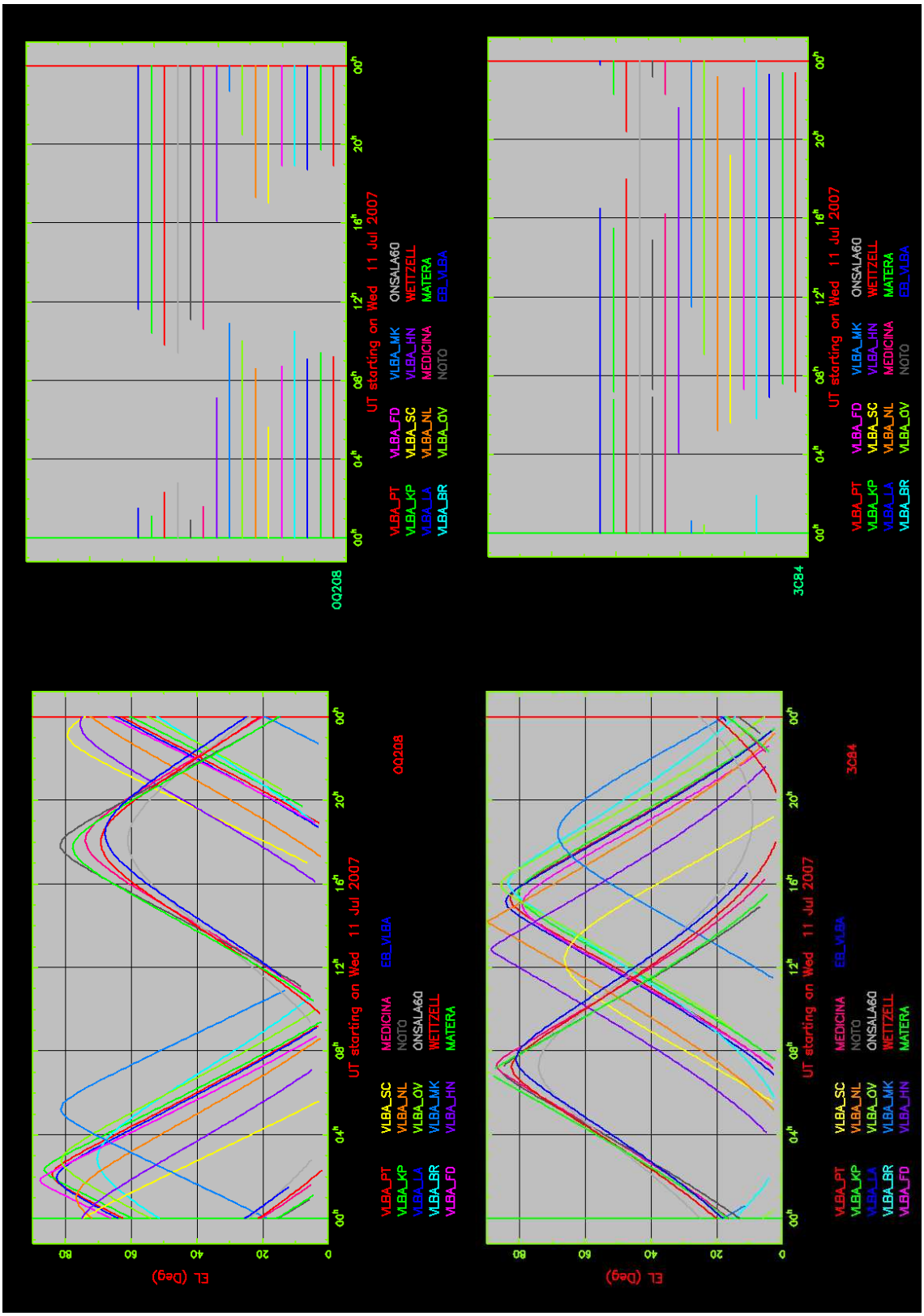

Figure 5.3: Top: periods of time when OQ 208 (top left) and 3C 84 (top right) are above the horizon at each telescope. OQ 208 was observed between 19:00 UT and 04:19 UT on the first day of observation, and 3C 84 was observed between 09:40 UT and 16:18 UT on the second day of observation. Bottom: elevation of OQ 208 (bottom left) and 3C 84 (bottom right) as a function of UT. Both sources are visible for the VLBA and European antennas simultaneously, within a limited range of UT.

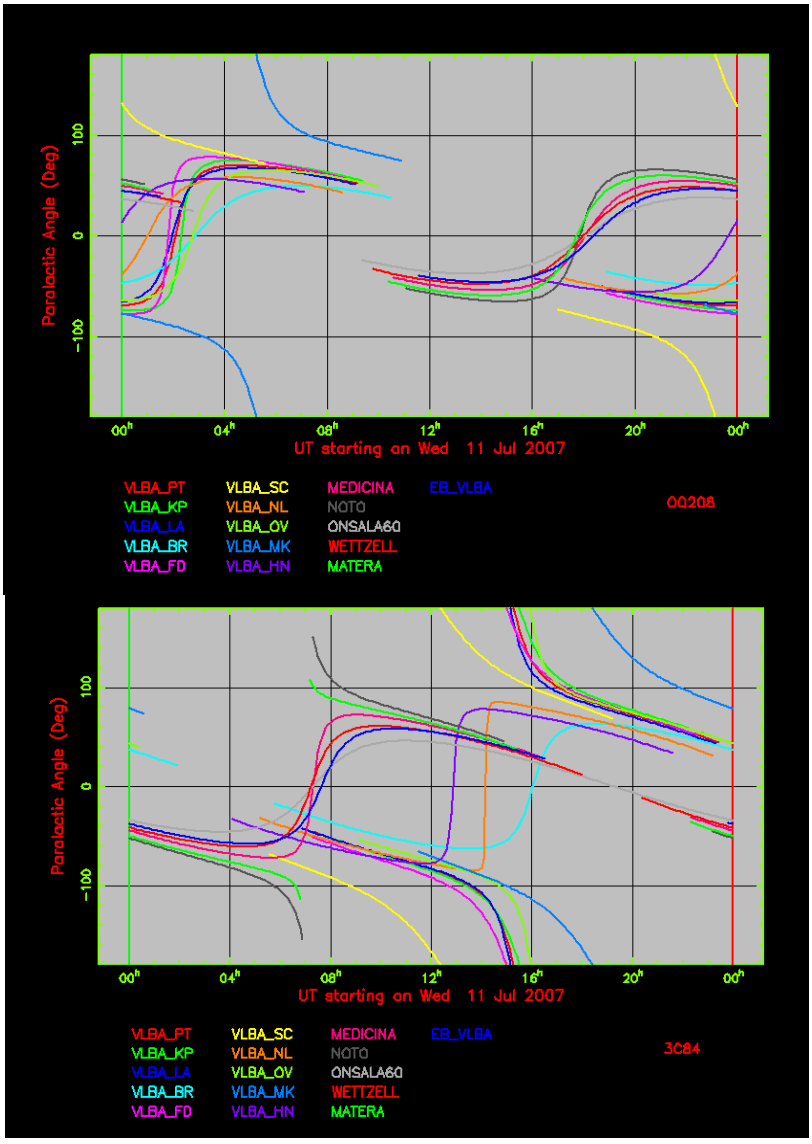

Figure 5.4: Top: parallactic angle coverage for OQ 208 as a function of UT. Bottom: parallactic angle coverage for 3C 84 as a function of UT.

setup name	X-band	X-band	X-band	S-band
sx_1	8212.99 MHz	8308.99 MHz	8324.99 MHz	2225.99 MHz
sx_2	8228.99 MHz	8340.99 MHz	8356.99 MHz	2235.99 MHz
sx_3	8244.99 MHz	8372.99 MHz	8388.99 MHz	2245.99 MHz
sx_4	8260.99 MHz	8404.99 MHz	8420.99 MHz	2255.99 MHz
sx_5	8276.99 MHz	8436.99 MHz	8452.99 MHz	2265.99 MHz
sx_6	8292.99 MHz	8468.99 MHz	8484.99 MHz	2275.99 MHz
sx_7	8500.99 MHz	8692.99 MHz	8708.99 MHz	2285.99 MHz
sx_8	8516.99 MHz	8724.99 MHz	8740.99 MHz	2295.99 MHz
sx_9	8532.99 MHz	8756.99 MHz	8772.99 MHz	2305.99 MHz
sx_10	8548.99 MHz	8788.99 MHz	8804.99 MHz	2315.99 MHz
sx_11	8564.99 MHz	8820.99 MHz	8836.99 MHz	2325.99 MHz
sx_12	8579.99 MHz	8852.99 MHz	8868.99 MHz	2325.99 MHz
sx_13	8596.99 MHz	8884.99 MHz	8900.99 MHz	2345.99 MHz
sx_14	8612.99 MHz	8916.99 MHz	8932.99 MHz	2355.99 MHz
sx_15	8644.99 MHz	8660.99 MHz	8676.99 MHz	2365.99 MHz

Table 5.3: Frequency sequences during RD0705, for the VLBA sites. The VLBA observed both LCP and RCP. Frequencies shown are for odd- or even-numbered BBCs. Frequencies for other four BBCs are the same – they just have the opposite polarization.

5.3.4 Integration Time

The integration time per scan was calculated using the radiometer equation (Wrobel and Walker 1999), given the bandwidth, source strength and antenna sensitivities.

$$\Delta \mathrm{S} = \frac{1}{\eta_{\mathrm{eff}}} \cdot \frac{\sqrt{\mathrm{SEFD}_1 \cdot \mathrm{SEFD}_2}}{\sqrt{2 \cdot \Delta\nu \cdot \tau_{\mathrm{int}}}} \tag{5.1}$$

where SEFD_1 and SEFD_2 are the system equivalent flux densities expressed in jansky for the two antennas, η_{eff} is the correlation efficiency (equal to 0.5 for 1 bit/sample and equal to 0.7 for 2 bit/sample), $\Delta\nu$ is the bandwidth in hertz, τ_{int} is the integration time in second, and ΔS is the root mean square (rms) thermal noise fluctuations expected in the measurement, in jansky. The SEFDs of the antennas used in this experiment are shown in Table 5.3.4. Knowing the SEFDs and the flux densities of the sources, I calculated the SNR using

$$\mathrm{SNR} = \frac{\mathrm{S}}{\Delta \mathrm{S}} \tag{5.2}$$

where S is the source flux density (Wrobel and Walker 1999).

During the first 12 hours, one target source (OQ 208) was observed using 15 frequency setups (as described in Section 5.2.1) plus two backup targets (1308+326 and 1357+769). In addition one position angle calibrator (3C 454.3) was observed using four frequency setups covering the 720 MHz band used in the geodetic wideband sequence.

Being satisfied with the source selection, integration time planning and considering that the telescope systems need gaps between scans for slewing to the new source, I decided to observe the target source for 3.7 minutes per scan. The X-band SNR for OQ 208 with a 16 MHz bandwidth, was $\mathrm{SNR}_x = 17$ on the least sensitive baseline and $\mathrm{SNR}_x = 33$ on the most sensitive baseline; the S-band SNR for OQ 208 with a 16 MHz bandwidth, was $\mathrm{SNR}_s = 22$ on the least sensitive baseline and $\mathrm{SNR}_s = 46$ on the most sensitive baseline. The calibrators were observed for 2.3 minutes per scan. The X-band SNR for the calibrators with a 16 MHz bandwidth, was $\mathrm{SNR}_x = 7$ on the least sensitive baseline and $\mathrm{SNR}_x = 70$ on the most

BBC no.	BBC1	BBC2	BBC3	BBC4	BBC5	BBC6	BBC7	BBC8	BBC11
IF no.	IF1	IF1	IF1	IF1	IF3	IF3	IF3	IF3	IF2
Band	X-band	X-band	X-band	X-band	X-band	X-band	X-band	X-band	S-band
sx_1	8212.99 MHz	8212.99 MHz	8308.99 MHz	8308.99 MHz	8324.99 MHz	8324.99 MHz	8308.99 MHz	8324.99 MHz	2225.99 MHz
sx_2	8228.99 MHz	8228.99 MHz	8340.99 MHz	8340.99 MHz	8356.99 MHz	8356.99 MHz	8340.99 MHz	8356.99 MHz	2235.99 MHz
sx_3	8244.99 MHz	8244.99 MHz	8372.99 MHz	8372.99 MHz	8388.99 MHz	8388.99 MHz	8372.99 MHz	8388.99 MHz	2245 MHz
sx_4	8260.99 MHz	8260.99 MHz	8404.99 MHz	8404.99 MHz	8420.99 MHz	8420.99 MHz	8404.99 MHz	8420.99 MHz	2255.99 MHz
sx_5	8276.99 MHz	8276.99 MHz	8436.99 MHz	8436.99 MHz	8452.99 MHz	8452.99 MHz	8436.99 MHz	8452.99 MHz	2265.99 MHz
sx_6	8292.99 MHz	8292.99 MHz	8468.99 MHz	8468.99 MHz	8484.99 MHz	8484.99 MHz	8468.99 MHz	8484.99 MHz	2275.99 MHz
sx_7	ntf	nft	8500.99 MHz	8500.99 MHz	8692.99 MHz	8692.99 MHz	8708.99 MHz	8708.99 MHz	2285 MHz
sx_8	ntf	nft	8516.99 MHz	8516.99 MHz	8724.99 MHz	8724.99 MHz	8740.99 MHz	8740.99 MHz	2295 MHz
sx_9	ntf	ntf	8532.99 MHz	8532.99 MHz	8756.99 MHz	8756.99 MHz	8772.99 MHz	8772.99 MHz	2305.99 MHz
sx_10	ntf	ntf	8548.99 MHz	8548.99 MHz	8788.99 MHz	8788.99 MHz	8804.99 MHz	8804.99 MHz	2315.99 MHz
sx_11	ntf	ntf	8564.99 MHz	8564.99 MHz	8820.99 MHz	8820.99 MHz	8836.99 MHz	8836.99 MHz	2325.99 MHz
sx_12	ntf	ntf	8579.99 MHz	8579.99 MHz	8852.99 MHz	8852.99 MHz	8868.99 MHz	8868.99 MHz	2325.99 MHz
sx_13	ntf	ntf	ntf	ntf	8884.99 MHz	8884.99 MHz	8900.99 MHz	8900.99 MHz	2345.99 MHz
sx_14	ntf	ntf	ntf	ntf	8916.99 MHz	8916.99 MHz	8932.99 MHz	8932.99 MHz	2355.99 MHz
sx_15	ntf	ntf	ntf	ntf	ntf	ntf	ntf	ntf	2365.99 MHz

Table 5.4: Frequency sequences used in RD0705 for the Mark IV sites. Frequencies shown are for first 8 BBC/BBCs in a Mark IV rack. The frequencies for the S-band for the Mark IV were the same as the single S-band frequency in the VLBA setup of the same name in Table 5.3.2. nft = no tunable frequency in IF1 low range and or IF3 and that BBC could be set to any value. Setup sx_15 was observed for the VLBA stations, since they are also interested in the leakage characteristic of their receivers. BBC9, BBC10, BBC12, BBC13 and BBC14 were unused.

IVS name	RA (J2000) [hh:mm:sec]	Dec (J2000) [deg:arcmin:arcsec]	flux density (8.4 GHz)	flux density (2.3 GHz)	Type
OQ 208	14:07:00.394414	+28:27:14.69021	0.48 Jy	0.65 Jy	target
1357+769	13:57:55.371532	+76:43:21.05103	0.77 Jy	0.66 Jy	backup target
1308+328	13:10:59.4027290	+32:33:34.449600	1.20 Jy	0.54 Jy	backup target
3C 454.3	22:53:57.747942	+16:08:53.56087	1.21 Jy	–	position angle calibrator
0016+731	00:19:45.786416	+73:27:30.01749	1.02 Jy	0.12 Jy	position angle calibrator
0552+398	05:55:30.805615	+39:48:49.16500	1.76 Jy	2.45 Jy	backup target
1803+784	18:00:45.683908	+78:28:04.01844	1.16 Jy	1.08 Jy	backup target
1849+670	18:49:16.072284	+67:05:41.68029	0.43 Jy	0.16 Jy	backup target
3C 84	03:19:48.1601	+41:30:42.106	1.11 Jy	1.76 Jy	main target
OJ 287	08:54:48.874930	+20:06:30.64086	1.36 Jy	1.06 Jy	position angle calibrator

Table 5.5: Sources observed and their coordinates taken from Kovalev et al (2007) apart from 3C 84 whose flux density was taken from: http://www.vlba.nrao.edu/astro/calib/vlbaCalib.txt.

Station	SEFD (8.4 GHz)	SEFD (2.3 GHz)
VLBA (all)	337 Jy	407 Jy
Onsala	1530 Jy	1663 Jy
Westford	1785 Jy	1595 Jy
Wettzell	1115 Jy	750 Jy
Medicina	420 Jy	285 Jy
Noto	900 Jy	1000 Jy
Matera	407 Jy	1337 Jy
Effelsberg	18 Jy	306 Jy

Table 5.6: SEFD at both S- and X-band of the antennas involved in this project as at July 2007, taken from the schedule catalogue file (ftp://gemini.gsfc.nasa.gov/pub/sked/catalogs/equip.cat) as it was in 2007 before the observation. Since SEFD values can change (with receiver upgrades, warm amplifiers and so on), the values in the catalogues as at 2010 may differ from those in this table.

sensitive baseline; the S-band SNR for the calibrators with a 16 MHz bandwidth, was $SNR_s = 3$ on the least sensitive baseline and $SNR_s = 35$ on the most sensitive baseline. The gap between scans was set to be 41 seconds.

5.3.5 Station Control File Generation

The control file is a station-specific low-level command file required to configure the station systems and send commands to the telescope control computer during the observation. For VLBA stations, *sched* produced the control file. For the Mark IV stations an additional step is required and is performed running a program called *drudg* (Vandenberg 1997). Since *drudg* is normally run at the station shortly before the observations, I would not know whether errors occurred for RD0705, hence I ran *drudg* to ensure that the stations would not encounter unexpected problems. I also invited the participating stations to run it and send back the results. Fortunately *drudg* ran to completion, however with many warnings. In this way I detected some subtle bugs in the *sched* code extensions that had been written for this observation. These bugs would have prevented the telescope software from understanding the commands. The command files prepared for the Mark IV stations were missing the IF3-related commands, since *sched* requires IF3 to be called '3' and not '3N' as *drudg* expected. This was easily solved by changing the *sched* code to accept '3N'. For the Mark IV stations *drudg* complained about one frequency setting, that was 0.01 MHz away from the settable limit, but *drudg* still generated the correct commands. Therefore I ignored the warning and asked the stations to check that the BBC in question locked at the selected frequency. After I had dealt with all the warnings, I asked Medicina to run *drudg* on the schedule file again as a check and they encountered no problems. The schedule file was then submitted to the stations with recommendations about how to deal with the known warnings and how to skip them, along with some further instructions.

5.4 Observation

The observation took place on day 11 of July, 2007 from 18:00 UT and lasted 24 hours. The station personnel took care of the observation as normal. No input was required from the principal investigator (I) during observing beyond that provided prior to observing by sending the schedule file.

Ny Alesund was not scheduled in the end due to a manpower limitation and the VLBA station at Hancock did not observe since it was down for repairs. This reduced the number of antennas in the experiment, from 19 to 17.

5.5 Correlation and Fringe Fitting in HOPS

The data were correlated using the Bonn MPIfR/BKG Mark IV correlator (Whitney 2000 and Whitney et al 2004). Before starting the correlation, I prepared the files that initialized the correlator and gave the parameters concerning the experiment, the stations, and the scans. All control files are ASCII format and use the VEX (VLBI EXperiment) language developed for VLBI observation[3]. Correlation of the experiment started in October 2007 and lasted about two months. Since the correlator had eight Mark 5A playback units and I had a total of 16 stations, I ran the correlation in six passes to form all the baselines. Correlation was performed between all possible combinations of polarization (i.e. RCP against RCP, LCP against LCP, RCP against LCP and LCP against RCP) as required to determine the polarization leakages. The correlator can find cross-correlation if this is present in a very small interval of delay (typically 2μs) due to computational power. The propagation delay across the earth is up to 42 ms whcih is much larger than the correlator can search, and so the bulk geometric delay is removed by pre-shifting the data during the correlation. The bulk delay is calculated using a model called CALC 8 (Sovers et al 1998), which includes effects such station positions, earth rotation, tides. Due to effects

[3]http://www.vlbi.org/docs/vex%20definition%2015b1.pdf

that are not modelled in CALC 8, like wet atmosphere and ionosphere, the correlator output phases show unwanted residual changes versus time and versus frequency. These residual slopes are removed by the post-correlation software which uses the algorithm described in Clark et al (1985). The results of the correlation of this experiment were checked using the Haystack Observatory Postprocessing System (HOPS, http://www.haystack.mit.edu/tech/vlbi/hops.html) and found that most setups yielded good quality data, though some were degraded by radio frequency interference (RFI), especially in S-band. Fringes were visible to the VLBA antennas and to most of the geodetic antennas. Unfortunately I lost Kokee Park and Fortaleza due to technical reasons, which reduced the number of antennas in the experiment to 15. Examples of the fringe-fitted data are shown in *fourfit* plots in Figures A.1, A.2 and A.3. Figure A.1 is the cross-correlation between Westford (Wf) and North Liberty (Nl) on one scan (220 s long), RCP against RCP for the target source OQ 208. OQ 208 and the calibrators yielded good fringes in both polarizations. Since OQ 208 is unpolarized, one would not expect to see fringes between RCP at the geodetic antenna and LCP at the VLBA antenna, however fringes are nevertheless visible. This is a first evidence for the presence of polarization leakage. The SNR is, in this case, much lower ($\mathrm{SNR}_{\mathrm{S-band}} \approx 11$ and $\mathrm{SNR}_{\mathrm{X-band}} \approx 16$) than the SNR of the fringes in the RCP-RCP cross-correlation ($\mathrm{SNR}_{\mathrm{S-band}} \approx 86$ and $\mathrm{SNR}_{\mathrm{X-band}} \approx 78$). To help the reader with understanding, the complete *fourfit* plots are explained in Appendix A.

After the data were fringe fitted with HOPS, the data reduction and the determination of the polarization leakage proceeded using AIPS (Astronomical Image Processing System), which is one of the most widely used interferometric data reduction packages for radio astronomy.

Chapter 6

Data Reduction to Determine Polarization Leakage

6.1 Introduction

The determination of polarization leakage requires amplitude and phase calibration, fringe fitting, imaging, deconvolution, self-calibration and leakage determination solving simultaneously for source polarization. For this purpose, the Astronomical Image Processing System (AIPS) package was chosen because it implements the algorithms required to calculate the polarization leakage. Figure 6.1 is a cartoon describing the work flow described in this chapter.

AIPS was developed by the National Radio Astronomy Observatory (NRAO) in the USA for processing the data collected by the Very Large Array (VLA) in New Mexico and was subsequently enhanced to accommodate the needs of VLBI data reduction. RD0705 correlated data were imported into AIPS and processed up to and including the determination of the polarization leakage.

6.2 From Correlator Output Format to AIPS Format: MK4IN

The Mark IV correlator output is not directly readable into AIPS because it consists of lag-based complex numbers in delay space, whilst AIPS reads data in the frequency domain (Romney 1999). To transform the correlatior raw data into frequency domain, I processed them using the *fourfit* program in HOPS, since it performs a Fourier transform from lag domain to frequency domain in addition to fringe fitting (for proof of the Fourier transform relationship see Romney 1999).

The program MK4IN (Alef and Graham 2002) uses the HOPS input/output routines to read the cross-spectral output created by *fourfit* and converted the calibrated data into AIPS internal format along with ancillary information which was read from the correlator control files together with the station coordinates, frequencies observed and other parameters that will be described in the next section. After running MK4IN the data were in AIPS, ready for processing.

6.3 Astronomical Image Processing System (AIPS)

Before explaining the data reduction pipeline, I briefly summarize here the AIPS data structure and philosophy, since it is relevant for the understanding of the following sections in this chapter. AIPS reads in the correlation output in the form of amplitude and phase, also called fringe visibilities, and stores them in binary format with their time stamps, a number that represents an antenna uniquely (i.e. every antenna in the array has one number), and the baseline length. This information is stored for

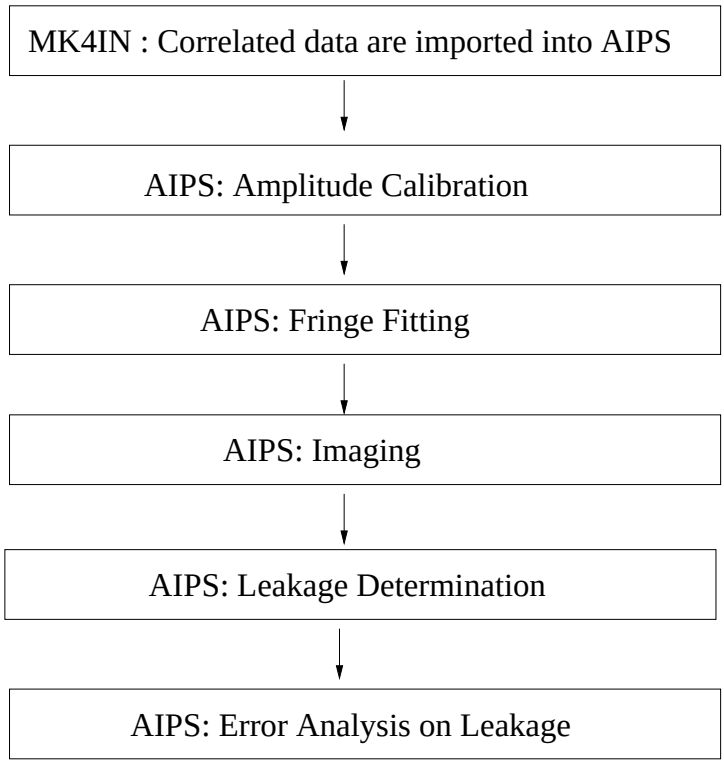

Figure 6.1: Cartoon describing the data reduction flow.

every accumulation period (i.e. for RD0705, 2 s) and the correlator amplitudes and phases are stored for every spectral channel of every BBC channel and for every polarization. Attached to these visibility measurements are the following ancillary tables.

- Antenna Table: contains the name of the antennas, their mount type, their coordinates, axis offset and a free space to insert the polarization leakage phases and amplitudes.
- Source Table: contains among other things, the name, the coordinates and their epoch for every observed source.
- Frequency Table: lists the observed sky frequency for each BBC, along with the BBC bandwidth in kHz and the bandwidth of the single spectral channel.
- System Temperature Table: contains the value of the system temperature ($T_{\rm sys}$) [1] . They are read separately into AIPS and are attached to the data.
- Gain Table: contains the antenna gains[2] and their dependence on elevation.
- Calibration Table (CL): AIPS does not alter the original visibility measurements during the calibration, but keeps the phases and amplitude corrections in this table.
- Solution Table (SN): contains incremental calibration that will be added vectorially to the previously generated CL table to improve the calibration.

[1] System temperature is the temperature of a fictitious resistor that would emit the same power as does the sum of all the noise contributions (the source, sky, ground pickup, and mostly receiver), referenced to the antenna terminals.

[2] the gain is a measure of the sensitivity of the antenna in K/Jy

Since AIPS does not alter the original visibility measurements during the calibration, one can always go back to the original data, which will never be corrupted by bad calibration. The first CL table contains unity amplitude corrections and zero phase corrections as so has no effect if applied to the data. Fringe fitting the data, for example, will produce an SN table that will be added vectorially to the previously generated CL table (i.e. the phases will be summed and the amplitudes multiplied) to create a second version of the CL table. In this way it is possible to make incremental improvements to the calibration or to go back a step or more in the data reduction in case of errors.

AIPS has a collection of routines called *tasks*, that can perform a wide variety of operations on the data and are controlled by setting the values of a group of *adverbs* prior to execution to perform a step in the data reduction. For example, fringe fitting is performed by a task called FRING, and an adverb to FRING is, for example, a parameter to control the fringe fitting, like the width of the multiband delay window.

6.4 Data Reduction Pipeline

For practical reasons, I reduced first the data for a frequency setup in S-band at 2225 MHz (S1) because it was particularly simple as it contained only one BBC. The reduction of this setup served as a pilot for implementing a Python script to automate the whole data reduction and data quality checking. Since the data reduction is very similar for all setups, I describe here only the data reduction of the setup at 2225 MHz.

The data were imported into AIPS and a priori amplitude calibration was performed to convert between correlator amplitude and flux density in jansky, based on $T_{\rm sys}$ measurements at the stations in each polarization and on the knowledge of the sensitivity of the antennas possibly as a function of elevation for each polarization.

6.4.1 Amplitude Calibration

In a first step, I performed amplitude calibration since I needed to image the sources for robust D-term determination in the presence of possible intrinsic source polarization. Amplitude calibration is fundamental for imaging since, as will be described later on in this section, the Fourier transform relationship between fringe visibility and sky brightness distribution is a complex transform, requiring accurate phase and amplitude measurements. Errors on either quantity degrade the image quality and can be detected from the ratio of peak signal to root mean square noise (i.e. the SNR or dynamic range) of the resulting image. Figure 6.2 shows the visibility amplitudes on OQ 208 before and after a priori amplitude calibration as a function of baseline length measured in wavelengths. Before the calibration the amplitudes are still expressed as correlator amplitude and have not yet been linked to the amplitude of the flux density of the observed source. After calibration there is good consistency between baselines, with the amplitude being higher on short baselines and lower on longer baselines, as expected, due to source structure. As comparison, the case of a point-like source posed at the phase centre would give, after calibration, a straight line parallel to the x-axis with amplitude equal to the source flux density. Since the point source remains unresolved on all baseline lengths, all baselines see the full flux density. The a priori amplitude calibration contained large systematic errors because the purely geodetic stations did not provide their elevation-dependent gain curves and many did not provide their SEFD values and their variations with frequency. The gain curves were assumed to be valid for the whole band which is expected to be a good assumption for all stations. The remaining amplitude calibration errors could be corrected later by applying amplitude self calibration after imaging the source.

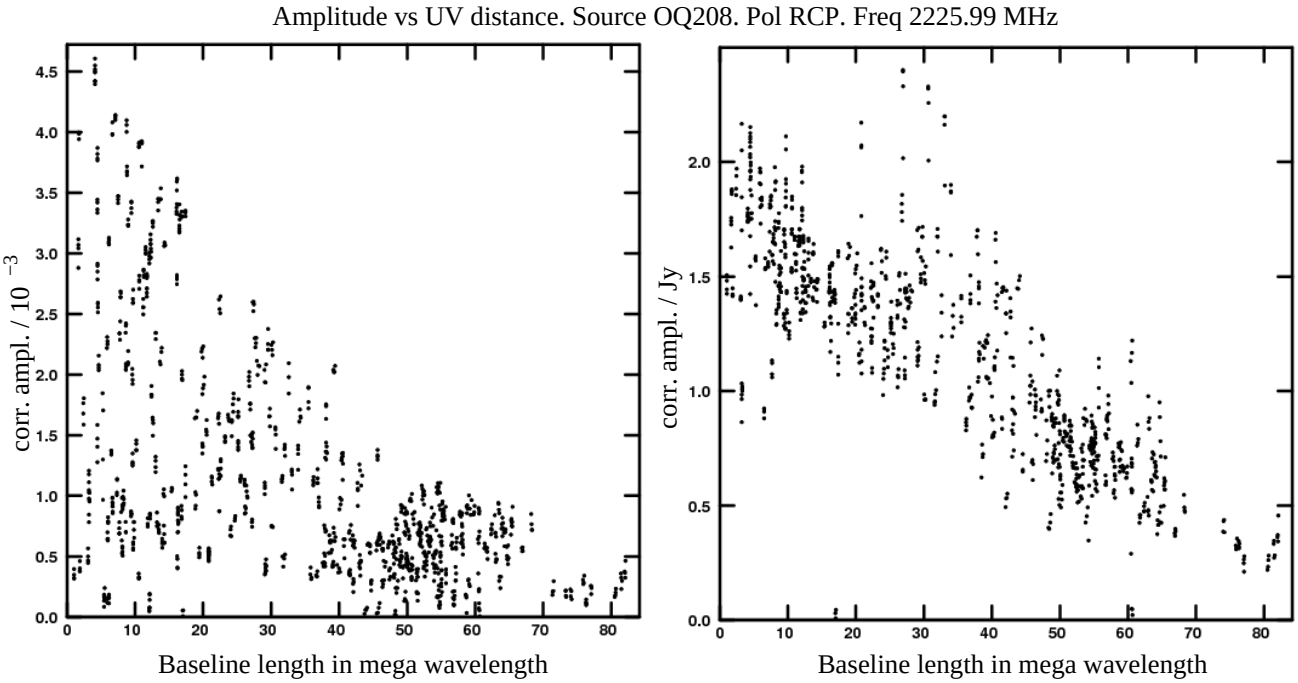

Figure 6.2: Calibration of the amplitude scale from SNR (correlator output) (left) to jansky (right) using a priori amplitude calibration based on $T_{\rm sys}$ and SEFD.

6.4.2 Fringe Fitting

After a priori amplitude calibration I performed phase, delay, and delay-rate calibration by fringe fitting the parallel hands of polarization (RCP-RCP and LCP-LCP) in AIPS. The AIPS fringe-fit algorithm is global (Schwab and Cotton 1983), i.e. it uses all constraints from the baselines when determining a delay solution for an antenna and potentially gives better SNR compared to the baseline-based fringe fit algorithm used by HOPS. Therefore I discarded the results of *fourfit* solutions and re-fringe fitted the data in AIPS. As an example, the phase and the amplitude of the data for one scan and one baseline before and after the fringe fit are illustrated in Figure 6.3. The top left panel of Figure 6.3 shows the uncalibrated phase vesrus frequency, it rotates from 0° to −180° wraps to 180° and rotates to 100° across the 16 MHz band. The top right panel shows the phase versus frequency after the data have been fringe fitted to remove the residual delay. In this panel the phase lie on a horizontal line close to 0° as one would expect in cases of good calibrated data. The bottom panels of Figure 6.3 show the amplitudes versus frequency in jansky before (left) and after (right) fringe fitting the data. As one can notice they are identical because fringe fit does not touch the amplitudes.

6.4.3 Imaging

The third step was to produce an image from the visibility data. Since there is no spatial coherence between electric fields generated by two surface elements within a radio source, their cross-correlation function is equal to the Fourier transform of the brightness distribution of the source, for quasi-monochromatic waves (Van-Cittert-Zernike theorem; Born and Wolf 1999)

$$V_\nu(\vec{r}_1,\vec{r}_2) \approx \int\int A(\vec{s})I_\nu(\vec{s})e^{\frac{-2\pi i\nu\vec{s}\cdot(\vec{r}_1-\vec{r}_2)}{c}}d\Omega \tag{6.1}$$

where $V_\nu(\vec{r}_1) = \langle\vec{E}_\nu(\vec{r}_1)\vec{E}^*_\nu(\vec{r}_2)\rangle$ is the cross-correlation function between the electric fields of two surface elements, '*' indicates the complex conjugate, $\vec{r}_1-\vec{r}_2$ is the vector separation between the two antennas,

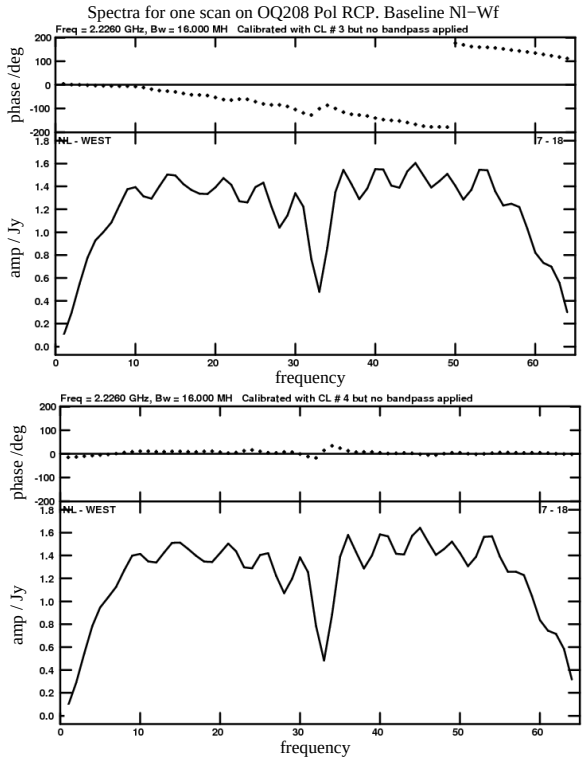

Figure 6.3: Example spectra on the North Liberty (VLBA) - Westford (IVS) baseline at 2225 MHz on OQ 208 showing amplitude in jansky vs frequency and phase in degrees vs frequency. Left: phase and amplitude without calibration: the phases rotates from 0° to -180° wraps to 180° and rotates to 100° across the 16 MHz band. Right: the phases are now corrected by fringe fitting the data to remove a residual delay and now lie on a horizontal line close to 0°.

$A(\vec{s})$ is the effective collecting area, $I_\nu(\vec{s})$ is the brightness distribution, $\vec{s}$ is the unit vector toward the source and $d\Omega$ is an element of solid angle subtended by the source as visible from the antennas.

For imaging, it is more convenient to express the baseline length in terms of wavelengths at the centre frequency of the RF band in the direction toward the East (coordinate u) and the North (coordinate v). The plane defined by this coordinate system is called the (u, v) plane and each antenna pair measures a point in the (u, v) plane (Clark 1999 and Thompson 1999). In this coordinate system,

$$\frac{\nu\vec{s}\cdot(\vec{r}_1-\vec{r}_2)}{c} = ul + vm \tag{6.2}$$

$$d\Omega = \frac{dldm}{\sqrt{1-l^2-m^2}} \tag{6.3}$$

where l and m are the source coordinates expressed as direction cosines in this reference frame. Figure 6.4 shows this coordinate system. In case of a source whose extension is small (like for geodesy) $l \approx 0$ and $m \approx 0$ therefore $d\Omega = dldm$.

Thus, Equation 6.1 can be written as

$$V_\nu(u,v) = \int\int A(l,m)I_\nu(l,m)e^{-2\pi\mathrm{i}(ul+vm)}dldm \tag{6.4}$$

which is equivalent to a Fourier transform, therefore, we can express the source brightness distribution as a function of the visibility measurements by inverting Equation 6.4.

$$A(l,m)I_\nu(l,m) = \int\int V_\nu(u,v)e^{2\pi\mathrm{i}(ul+vm)}dudv \tag{6.5}$$

Since the antenna spacings are sparse and irregular, the (u,v) plane coverage is sparse and irregular as well. For computational economy AIPS uses fast Fourier transforms (FFT) to calculate $A(l,m)I_\nu(l,m)$. The FFT requires the data to lie on a regular grid and that the number of sample points be a power of 2. Thus AIPS grids the visibility measurements onto the (u,v) plane and fills every pixel of the (u,v) plane with values. If the cell is empty then the value is zero. If the cell contains more than one measurement then AIPS uses a weighted average of the measurements as the cell value. To do that AIPS folds each visibility onto a regular grid with a gridding convolution function centred on the coordinates of the measurements, in other words, AIPS multiplies the data by a gridding convolution function and translate the convolution function to the centre of every (u,v) cell, integrates the product of the convolution function with the discrete function describing the surrounding visibilities measurements and writes the result into the corresponding (u,v) cell. In still other words, AIPS convolves the convolution function with the discrete function describing the surrounding visibility measurements and multiply it by a comb function. To avoid aliasing one wants to select a convolution function so that its Fourier transform remains unity within the image (i.e. 256 x 256 pixel) and has small or absent side lobes beyond the edges of the image. Sidelobes could allow a confusing source that lies outside the image to produce an aliased response within the image. To see whether a source in the image is an aliased response from a source outside the image one can change the cellsize as it would cause the aliased source to move within the image (Cornwell 1995).

The image obtained is called the dirty image (I_d), since it corresponds to the sky brightness (also called the real image), I, convolved with the synthesised beam (also called the dirty beam[3]), B and it is $I_\mathrm{d} = B * I$. The image can be deconvolved since B and I_d are known i.e. AIPS solves the equation for I. B is calculated by the imaging task IMAGR by replacing the measured amplitudes with a value equal to one and phases zero degrees and Fourier transforming it to form the point spread function (PSF)[4] in the image domain. The simplest way to deconvolve the image and PSF would be to take the Fourier transform of the above equation, and to divide the Fourier transform of I_d by the Fourier transform of B and then

[3]The dirty beam is the diffraction pattern of the array, which is given by the Fourier transform of the (u,v) plane coverage.

[4]The PSF is what I would see for a 1 Jansky (Jy) point source at the field centre

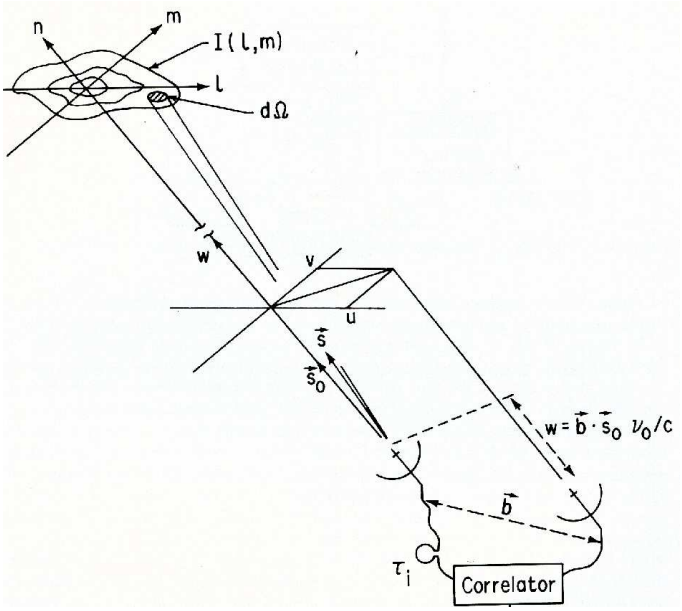

Figure 6.4: Scheme describing the (u,v) coordinate system and how the source coordinate are related to the (u,v) coordinate. At the top left the source of flux density $I_\nu(l,m)$ is visble and at the bottom right there is the two-telescope array observing it. Thompson 1999

Fourier transform the result back to the image domain. However this procedure fails because the Fourier transform of B has zeroes where there are no measurements, therefore the division is undefined in some areas. Instead this deconvolution can be performed using common algorithms such as CLEAN (Högbom 1974) or MEM (Maximum Entropy Method) (Burg 1967). I used the CLEAN algorithm, which iteratively takes the peak in the image, translates and scales the PSF to the position of the peak and subtracts a fraction of it from the whole image to partially remove the peak and its sidelobes. A δ-component with the same flux density is added in the clean map at the same position. I stopped the cleaning process when the largest negative value in the image was larger than the remaining positive peak and restored the image by adding back in a Gaussian profile at the position of the components that were subtracted away.

To reduce further the calibration errors in phase and amplitude, I iteratively improved my model of the sky brightness distribution using a self calibration cycle consisting of determining the antenna gains, imaging and deconvolving (CLEAN)(Cornwell and Fomalont 1999). This self-calibration cycle, when iterated, uses the visibility measurements and solves simultaneously for antenna-based gains and for the source structure.

Figure 6.5 shows the before-and-after images after two cycles of phase self calibration and one of amplitude self calibration. The artifacts in the image were reduced by the improvement in the amplitude calibration. Typically I used 12 iterations of self calibration to obtain a dynamic range between 200 : 1 to almost 400 : 1 depending on the setup, for the 1.6 Jansky (Jy) source OQ 208. The imaging process is required to calculate the leakage. The solutions (SN table) produced by the task IMAGR are required for solving simultaneously for intrinsic polarization and polarization leakage. Clearly the better the image the more precise the determination of the leakage.

6.4.4 Polarization Leakage Determination

At this point the total intensity calibration was complete and the polarization calibration began. The first step was to correct the delay offset between the two opposite hands of polarization due to differences in

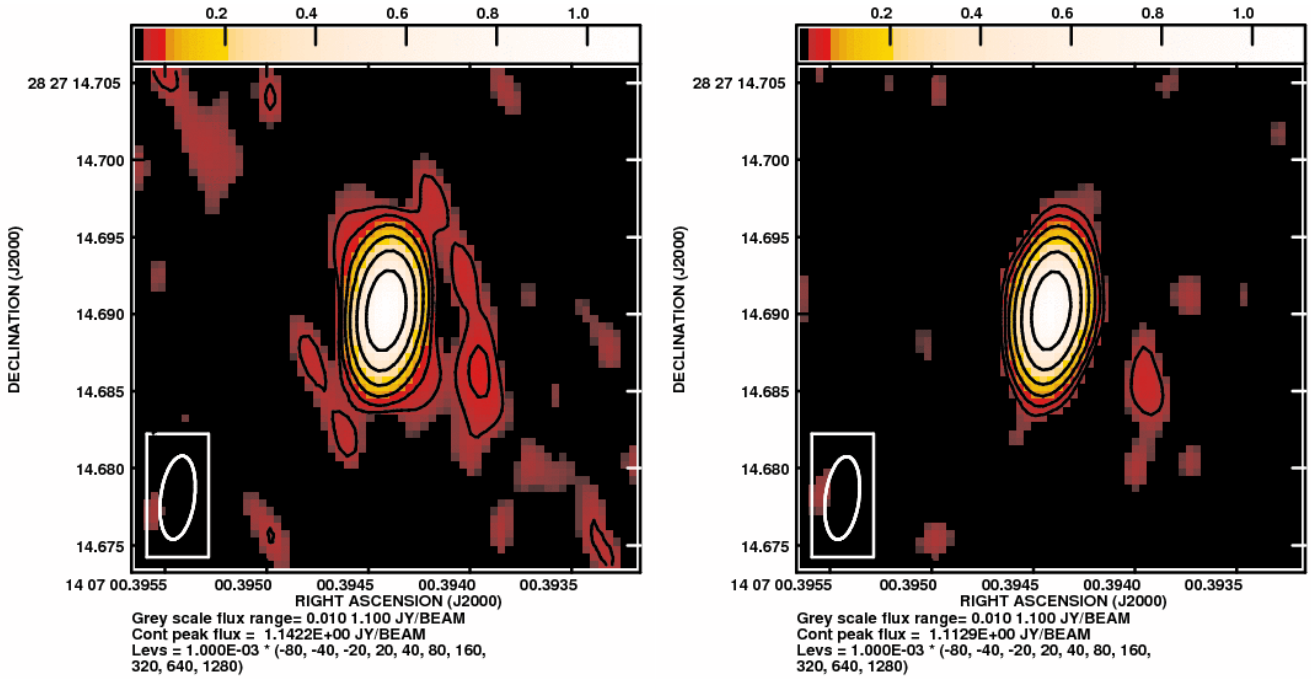

Figure 6.5: Image of OQ 208 at 2225 MHz with the VLBA and geodetic array with phase self calibration (left) and after amplitude self calibration (right).

the electronic path length. This could in principle be done by measuring the delay offset at one reference antenna between its LCP and RCP channels by performing a LCP-RCP autocorrelation for the following reason. The fringe fit that was performed on the parallel hands tied the RCP channels of all the antennas to the RCP channel of the selected reference antenna. Likewise the fringe fit tied the LCP channels of all the antennas to the LCP channel of the selected reference antenna. What remains is to tie the RCP to the LCP at the reference antenna. In practice the AIPS procedure VLBACPOL, which is a script that calls a series of tasks in sequence, performs this operation using the cross-hand cross-correlation. Instead of using the whole data within the frequency setup as is required in the step above, to tie the RCP to the LCP one needs only one baseline in one scan. This scan was selected for having enough SNR in the cross-hand cross-correlation to yield good delay solution during the fringe fit. This choice of using two antennas instead of one is done since the Mark IV correlator cannot perform autocorrelation between LCP and RCP channels and in any case the noise diode signal would dominate the RCP-LCP autocorrelation phases. This cross-hand cross-correlation was performed between only two VLBA antennas and two delay solutions were determined from the scan selected. The first delay solution was based on RCP-LCP cross-correlation and the second one was based on LCP-RCP cross-correlation. The two solutions should be equal except for a sign inversion and thermal noise. To improve SNR these two solutions were averaged, allowing for their sign inversion when the polarizations are swapped (Kemball 1999). This procedure tied the RCP and LCP channels at all antennas, including the geodetic antennas although they have no LCP channels.

The derivation of leakage proceeded as follows. If the source is polarized, the LCP-RCP (and RCP-LCP) cross correlations are non-zero. The RCP-LCP and LCP-RCP cross correlations contain also a contribution due to leakage between the polarization channels. The two contributions can be separated since the LCP-RCP phase due to source polarization rotates with the parallactic angle whereas the LCP-RCP phase due to leakage remains constant throughout an observation and over much longer periods (Cotton 1999). The result of this derivation is illustrated in Figure 6.6, which shows the LCP-RCP

cross correlation real and imaginary components for OQ 208 throughout the observation. The data were corrected for the parallactic angle, which means that the visibility phases were rotated according to the parallactic angle, causing the LCP-RCP phase due to source polarization to remain constant and the LCP-RCP phase due to the leakage to rotate. The rotating leakage vector is centred at zero in the real/imaginary plane as shown at the top of Figure 6.6. This is because OQ 208 is unpolarized. Had it been polarized, the rotating leakage vector would have not been centered at zero in the real/imaginary plane. The derivation of the leakage was performed using the AIPS task LPCAL (Leppanen et al 1995). The leakage disappears as the D-terms were derived and correction for them were applied as shown in the bottom of Figure 6.6.

The amplitudes of the leakage terms in this first setup were found to vary from -40 dB (1 % of power leakage of one polarization into the other) at Wettzell to -15 dB (17 % of power leakage) at Westford as is shown if Figure 6.7

Since the leakage value for Westford was so large, as an independent check on AIPS I checked with the HOPS package whether I could detect the signal produced by the leakage in the cross-correlation of the left circular feed at one VLBA antenna and the right circular feed at the Westford antenna and indeed had a detection.

The large leakage values derived above need not yet be of concern, since this analysis represents only one channel that lies at the extreme edge of the band where the worst leakage is expected. The concern for the geodesist lies in the variation with frequency of both the phase and amplitude of the leakage. Once the frequency dependence of the leakage was known, I could estimate and correct its effects on the group delay measurements.

Determination of the frequency dependence required repeating the analysis above for 45 frequencies, which called for automating the process.

6.5 Parsel Tongue Script

AIPS is an interactive program and all the tasks are performed on the fly, but there are two ways to run AIPS in batch mode. The first way is to write an AIPS procedure, the second way is to write a Python-based script. I chose the second way because it gave the option of complete access to the raw (u,v) data, had that been required, which is not possible within AIPS. ParselTongue, the Python-based interface to AIPS, was written and named by a convinced Herry Potter fan working for the Joint Institute for Very Long Baseline Interferometry in Europe (JIVE). The code and a small cookbook can be found at the web site http://www.jive.nl/dokuwiki/doku.php/parseltongue:parseltongue.

The script, which is reproduced in Appendix B, contained all the instructions for AIPS to calibrate the data with a quality sufficient to make an image with dynamic range of 300. I then used the calibrated data to derive the leakage by running the procedure VLBACPOL and the task LPCAL manually (as described in the previous section).

6.6 Data Reduction in X-band

The data reduction for the X-band, was conducted in the same way as for the pilot S-band setup using the Python script described in Appendix B. The only differences were in the number of BBCs present and in the source model that was used, since the source structure changed with frequency. For the S-band, only one setup was reduced, whilst for the X-band all 15 setups in the first 12 hours were reduced. Priority was given to the X-band setups since the precision of the group delay measurements comes primarily from the X-band.

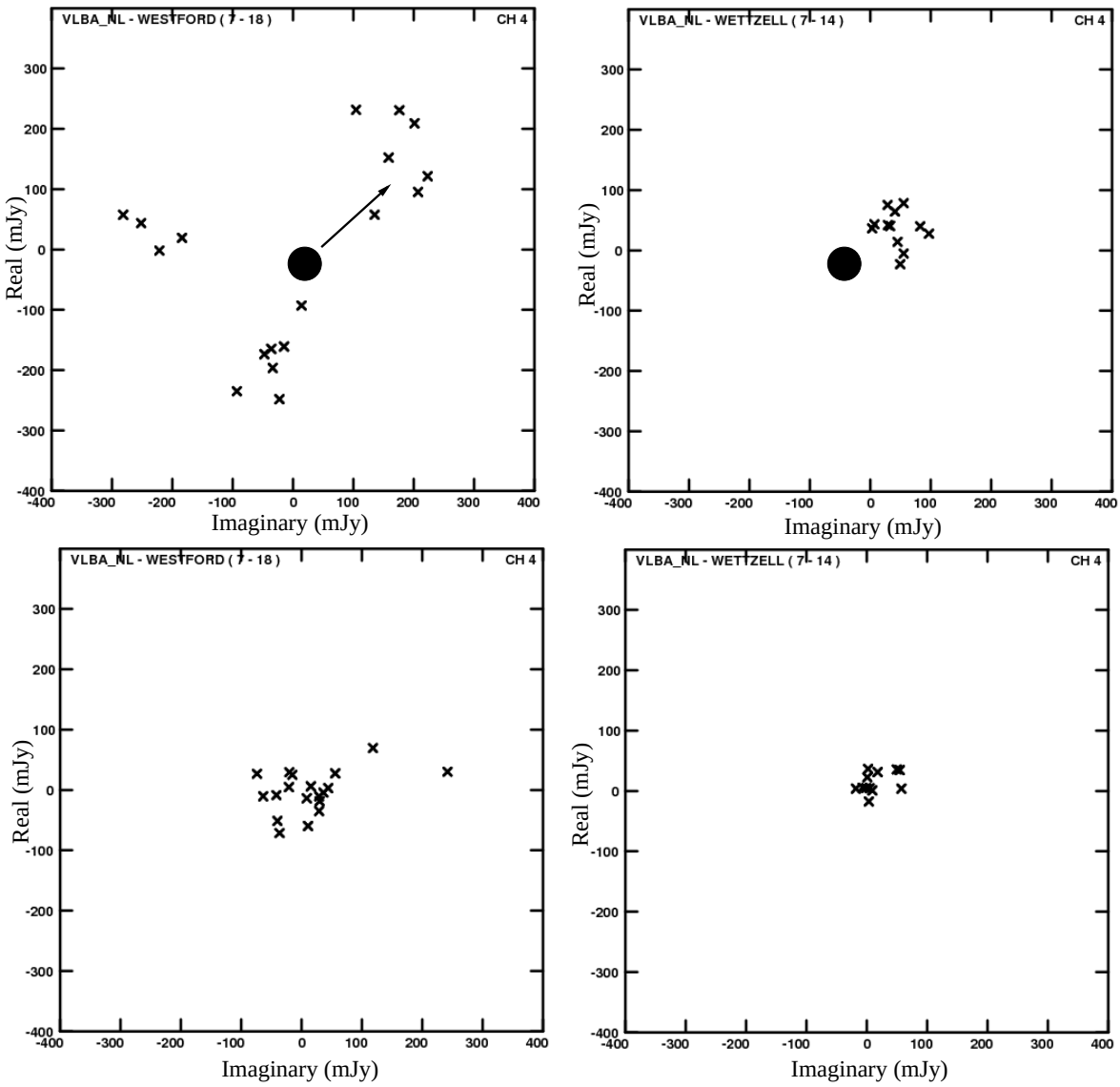

Figure 6.6: LCP-RCP visibility on the unpolarized source OQ 208 plotted in the imaginary vs real plane for the baseline North Liberty (VLBA) - Westford (IVS) (left column) and the baseline North Liberty - Wettzell (IVS)(right column) before the corrections for the instrumental polarization were applied (top row) and after the corrections were applied (bottom row). The big dot at the centre of the plots in the top row is the origin of the axes and the crosses are the measured visibilities, which rotate around the origin during the observation due to the relative rotation between the feed and the sky causing the leakage vector to appear to rotate. For clarity one of the vectors has been drawn in full for the baseline North Liberty - Westford. After applying the D-term correction the leakage vector has almost zero amplitude (bottom row).

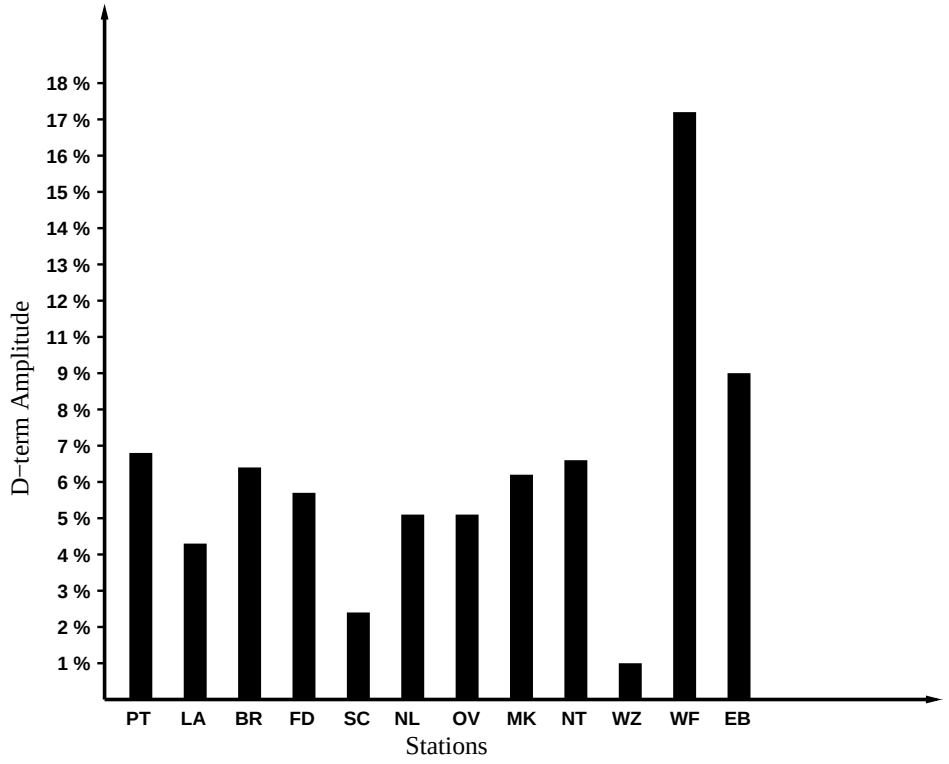

Figure 6.7: Amplitude of the polarization leakage for the IVS and VLBA stations for the frequency setup at 2225 MHz.

6.7 Error Budget

After having calculated the D-terms for all the antennas and all frequencies in X-band, I estimated the error on the D-term measurements. To do that I selected one of the frequency setups, specifically the setup sx_11 (X-band frequencies: 8564.99 MHz, 8820.99 MHz and 8836.99 MHz) because the data reduction showed that sx_11 produced good SNR on the cross hand fringes. Within this setup I had one D-term per station per frequency as calculated by the AIPS task LPCAL. Using another AIPS task, called DTSIM, I simulated the setup sx_11. DTSIM requires a parameter file (reproduced in Appendix B) which contains:

- Antenna paramters like mounting type and position,
- Frequency parameters like observed frequencies, bandwidth, number of BBC channels and polarization,
- Source parameters like coordinates and source model,
- Error parameters like thermal noise, antenna gain and D-terms,
- Observation parameters like when the source was observed, for how long and integration time.

In this case, the source was one source with the same characteristics as the source OQ 208, the antennas coordinates were selected to match the coordinate of the stations that really took part in the observation, the thermal noise and gain were taken from the system temperatures and system equivalent flux density monitored and tabulated by the stations for the real observation and the D-terms were taken to be those calculated from LPCAL for the setup sx_11. In summary, all the DTSIM parameters were selected to reproduce the real sx_11 observation. DTSIM generated from this parameter file a new set of cross-correlation coefficients as if produced by the correlator. Then I processed this new set of cross-correlation

coefficients artificially generated in the same way as I did for the real data, using the same Python script. The D-term derived in such way were compared to the D-terms used as input in the simulation, i.e. the ones calculated on the real data. This approach was used since the experiment is unique and cannot be easily reobserved to check repeatability and the calculation of formal error propagation from the observed data to the derived D-terms is not possible due to the complexity of the algorithms required for the data reduction of radio interferometry data. One could think that there are enough scans to make multiple independent determinations of the D-terms and compare their scatter to estimate the uncertainty. This is not possible because the SNR is not sufficient within a subset of data to allow D-term determination. Instead one must integrate over several scans to reduce fluctuations due to thermal noise and the experiment duration was chosen to allow to determine one D-term value per frequency. Thus the D-term solution is not an over-determined problem.

Before running the simulation, I checked that the source model description given to DTSIM was in good agreement with the real data. For this check, I ran DTSIM to create a dataset from the source model with no noise added and plotted the phases along with the real data (using the AIPS task VPLOT). If the model is a good representation of the true source structure, then the phases generated within the model should agree with the phases of the data. If there are problems with DTSIM's calculation of the data from the model, then it should show up as disagreement between the model and the data. Figure 6.8 shows the result of this test and one can see that the DTSIM-generated data agree with the source model. This test gave confidence that the program used for simulating the data was giving the expected results.

The comparison revealed the extent of systematic and random errors in the D-term derivation method, as follows in the next subsections. The test was performed only once because it required five months of work due to the poor documentation for this specific AIPS task and some errors in the code that I found and rectified. Had it not be for that one would have wanted to repeat the test a number of times.

A possible weakness of this method is that it does not explore the sensitivity of the result to the choice of data calibration and imaging techniques. Another possible method would have been to analyze the real data many times with various different analysis pipelines and comparing the agreement between the results (Monte-Carlo-style). A third possibility would be to re-observe and re-analyse RD0705 and compare the agreement between the results, however this is prohibitively expensive. A technique that is almost as good, without re-observing, is bootstrap resampling (Kemball and Martinsek 2005) in which many test datasets are generated from the observed dataset by selecting samples at random. The bootstrap method gives the statistical uncertainty on properties calculated from a set of measurements that are made from a parent population. Since one does not know the true property values of the parent population (e.g. median, interquartile range), one cannot estimate the errors by simply comparing by how much the calculated property values differ from their true values. Instead, the concept behind bootstrap resampling for estimating random measurement errors is to treat the set of measurements themselves as a parent population, of which we take sets of measurements (resampling). For each new set of (resampled) measurements, one calculates the property values (eg median, interquartile range) in the same way that one did for the real measurements of the real parent population. The key is that the same statistical fluctuations are at work in the real measurement process and in the resampling process since the sample sizes and parent distribution shapes are the same. The property values calculated for each resampled set of measurements will differ a little from each other due to the statistical sampling fluctuations. From the spread of values obtained, one sees directly how large are the statistical fluctuations and can quote an uncertainty due to this effect. Generally one would generate, say, 10000 such test datasets and analyse them and construct a distribution of errors. Bootstraping and its implementation in AIPS though would have implied to write a quite large amount of software (estimated at one year of effort) and so was not used.

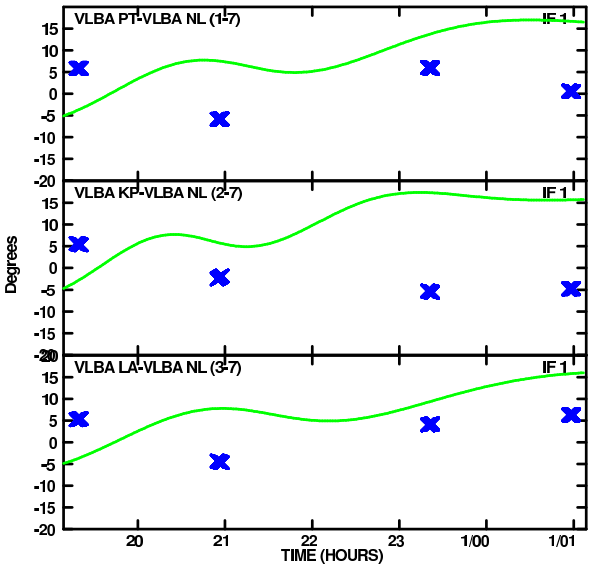

Figure 6.8: Visibility phase versus time for real and simulated data for a sample of baselines. Green lines: the model coming from the real data. Blue crosses: the phases of the simulated data. The phases show only small deviations from zero due to a secondary weak component close to the main source component at the phase centre (image centre). The simulated data follow the line relatively well.

6.7.1 Systematic Errors

One cannot normally determine systematic errors by repeated measurement since systematic error affects all measurements in the same way and normally one does not know the true value to compare to look for systematic bias between the measurements and the true value. The determination of the leakage will be influenced by any effects that corrupts the cross-hand cross-correlations coefficients therefore possible sources of systematic errors to be considered are:

- propagation effects. The tropospheric propagation delay is not polarization dependent since it is a neutral medium, it is isotropic and does not display birefringence[5]. Therefore troposphere does not change the cross-hand cross-correlations. The ionospheric propgation delay depends on the orientation of the plane of polarization with respect to the direction of the magnetic field. This causes Faraday rotation which could influence the measurement of the D-tems if it changes significantly during the observation. The amount of Faraday rotation at X-band is in the range between 0.08° and 0.8° for night time with total electron content of 5×10^{16} m^2 and day time with total electron content of 5×10^{17} m^2 (Thompson et al 2001a). These values are negligibly small.

- analog systems and cable lengths. Changes with time in the relative lengths of the electronic paths in the two polarization channels will affect the cross-hand cross-correlations. Such changes occur mostly due to temperature changes of the electronics and cables. This has been measured by injecting a test signal at the receiver such as that it passes through the same electronic path as the astronomical signal and the test signal is extracted in the data acquisition system. The test signal phase is compared to a phase reference to detect changes in the electrical path length with time. The test signal is injected in both polarization channels and extracted separately. This allows comparison of the path length through the two polarization channel. The typical effect is shown in

[5] A birefringent medium is changing the index of refraction of the light in dependence of the orientation of the plane of polarization. A birefringent medium is for example the ionosphere

Figure 6.9. The Figure shows that the path lengths do not differ by more than 2° over six hours. These values are also negligibly small.

- correlator. The correlator is a digital system whose behaviour is well known and by its design has phase measurement errors below 2° (Rogers 1991. These errors are also negligibly small.
- algorithms used in the data reduction. This is the most likely place for systematic errors to arise because the algorithms are non linear (i.e. deconvolution in imaging), in some places iterative (i.e. self-calibration steps), therefore the systematic errors can accumulate, in some places operates with low SNR (i.e. cross-hand fringes) and in some places involve a linear approximation to a non-linear process (i.e. simultaneous solution of source structure, source polarization and the D-terms). This is a sufficiently complex sequence of algorithmic steps, many of which lack a formal error analysis and so it is not possible to calculate analytically the formal error propagation. Thus one must use numerical experiments with datasets that should produce known results.

In the following discussion, I consider the errors introduced by the algorithms. Systematic errors were searched for by differencing the D-terms derived from the simulated data (section 6.7) and those used to generate the simulated data and seeing whether the differences have a zero mean and random scatter. Plots of the differences are shown in Figures 6.10 for the imaginary components and in Figure 6.11 for the real components. In this case, the situation is unusually easy because the true values of the D-terms (that is the one put in to generate the simulated data set) are known. Thus, it is straightforward to detect systematic error in the data reduction algorithms by looking at bias between the measured and true values.

The null hypothesis was that there were no systematic errors, i.e. that the difference between true and measured D-term was zero on average. I would have rejected the null hypothesis and concluded instead that there was a systematic difference only if I saw a statistically significant departure of the measured median away from zero. The probability of a given departure of the measured median away from zero is given by the standard error of the mean (SEM) in the case that errors are not correlated. Since there is no apriori knowledge of the degree of correlation of the errors, one would ideally measure the correlation with repeated simulated datasets, with small variations in the parameter sets during the data reduction and with different noise and calculate the covariance matrix. The process of simulation and analysis of the first simulated data set took five months. At least another four datasets and preferably many more, would be required to have statistical significance in the covariance matrix which amounts to a prohibitive length of time. Instead of assuming Gaussian errors I used the real error distribution as revealed by the simulation performed and using non-parametric statistics as follows. The median difference is 0.0015 (dimensionless quantity) for the real part and 0.0012 (dimensionless quantity) for the imaginary part. The uncertainty on the median was estimated by bootstrap resampling (Johnson 2001) with 100 trials and yielded a 95 % confidence interval that spanned from -0.00125 to 0.002800 (dimensionless quantities) for the real part and from -0.0014 to 0.0030 for the imaginary part, thus the median did not differ from zero by more than the 95 % confidence interval and so I cannot reject the null hypothesis with confidence, thus there is no evidence for detectable systematic errors. This gave confidence that the data reduction pipeline did not introduce a systematic bias in the case tested and there was no expectation that the pipeline would have introduced systematic errors in the other setups too.

6.7.2 Random Errors

The 95 % confidence interval on the D-term measurement was estimated from the spread in the differences between the D-terms derived from the simulated data and those used to generate the simulated data, differencing both the real components and the imaginary components (Figures 6.10 and 6.11). The 95 % confidence interval on the real part of the D-term is 0.016 (dimensionless) and the 95 % confidence interval on the imaginary part of the D-term is 0.011 (dimensionless). I averaged these estimates and found the

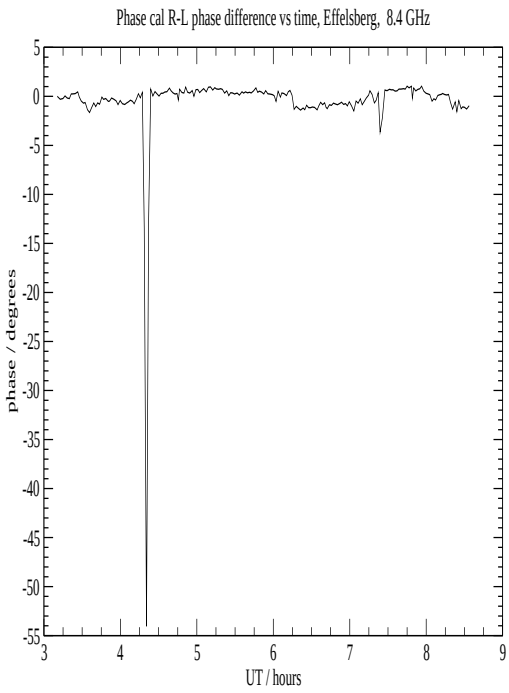

Figure 6.9: Effects of the cable length variation due to temperature changes. This effect influences the D-term determination.

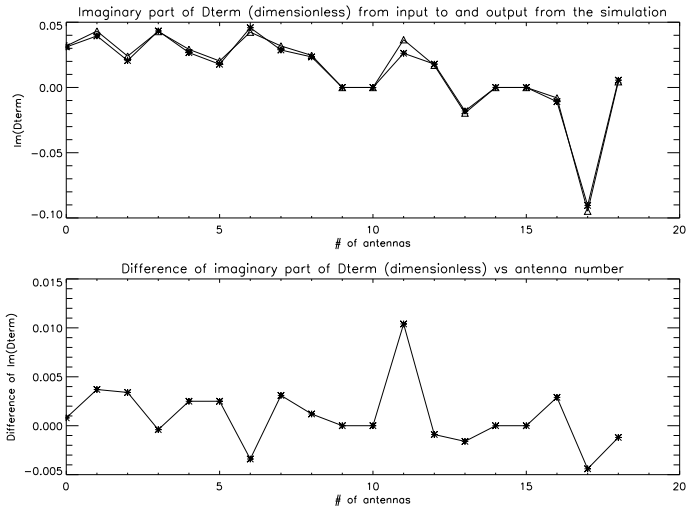

Figure 6.10: Top: Imaginary part of the LCP leakage (dimensionless) into the RCP feed at 8564.99 MHz versus the antenna number as used to generate the simulated data and as derived from the real data. Bottom: difference of the two lines in the top plot, with vertical scale magnified by a factor 3 compared to the top plot.

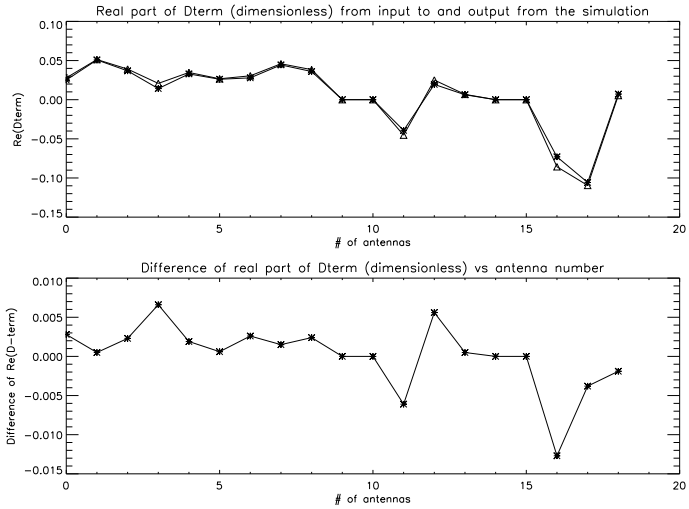

Figure 6.11: Top: Real part of the LCP leakage into the RCP (dimensionless) feed at 8564.99 MHz versus the antenna number as used to generate the simulated data and as derived from the real data. Bottom: difference of the two lines in the top plot, with vertical scale magnified by a factor 10 compared to the top plot.

final 95 % confidence interval uncertainty was 0.013. This value is used later when quoting the D-terms with their uncertainties.

From the error analysis one should capture errors due to algorithms, as explained in the itemized list in Section 6.6.1 and due to thermal noise.

6.8 Converting Error Estimates from Real and Imaginary to Amplitude and Phase

The errors on the amplitudes and the phases of the D-terms were derived from the random errors on the real and imaginary components and they are not Gaussian, but rather are Rice distributed (Thompson et al 2001b). The Rice distribution is the same as the Gaussian distribution for high SNR (SNR > 5), but is noticeably different at low SNR (see Figure 6.12). The typical D-term measurements for the antennas that took part in RD0705 have low enough SNR to be in that range where the Rice distribution is needed.

The Rice distribution is described by the following equations (Thompson et al 2001b):

$$p(Z) = \frac{Z}{\sigma^2}\exp(-\frac{Z^2+|D|^2}{2\sigma^2})I_0(\frac{Z|D|}{\sigma^2}) \tag{6.6}$$

$$p(\phi) = \frac{1}{2\pi}\exp(-\frac{|D|^2}{2\sigma^2})\{1+\frac{\sqrt{\pi}}{2}\frac{|D|\cos\phi}{\sigma}\exp(\frac{|D|^2\cos^2\phi}{2\sigma^2})[1+\mathrm{erf}(\frac{|D|\cos\phi}{\sqrt{2}\sigma})]\} \tag{6.7}$$

where $p(Z)$ and $p(\phi)$ are respectively the probability distribution for the amplitude and the phase, I_0 is the modified Bessel function of zero order, erf is the error function, D is the D-term vector, σ is the 95 % confidence interval on the real or imaginary components of the D-terms and Z is the sum of the visibility plus noise.

To estimate the amplitude errors I took each D-term amplitude measurement as $|V|$ and the random noise estimate (0.013) as σ in Equations 6.6 and 6.7. A C-program was written to integrate numerically the area under the wings of the of the Rice distribution to find the 98 % confidence interval. The program is reproduced in Appendix B and the resulting distributions are shown for three illustrative cases in Figure 6.12 and Figure 6.13. One can see that, for high-amplitude D-term (0.1637) the distributions look Gaussian, but for low amplitudes (0.0009) the amplitude distribution becomes noticeably skewed. The

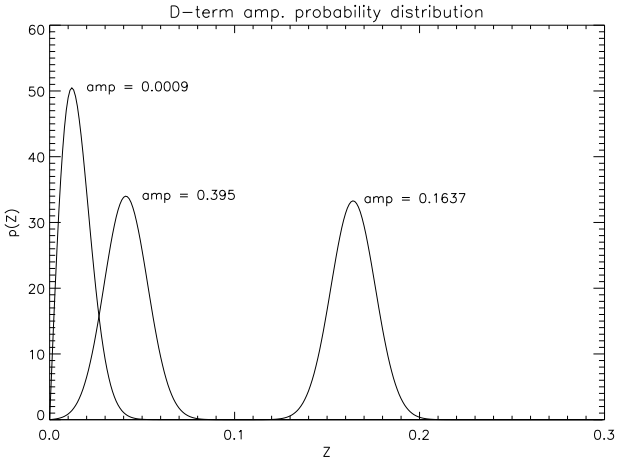

Figure 6.12: D-term amplitude probability distribution for the maximum D-term amplitude (0.1637), the median (0.0395) and the minimum (0.0009) D-term amplitude found in RD0705, for a 95 % confidence interval on the real and imaginary components of 0.013. The lower the D-term amplitude the more skewd is the distribution.

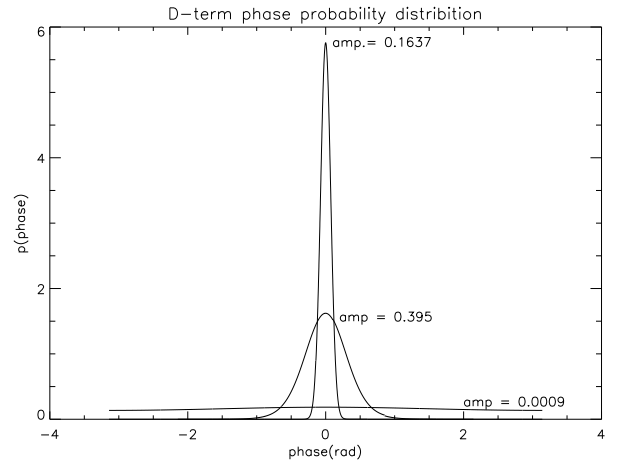

Figure 6.13: D-term phase probability distribution for the maximum D-term amplitude (0.1637), the median (0.0395) and the minimum (0.0009) D-term amplitude found in RD0705, for a 95 % confidence interval on the real and imaginary components of 0.013.

98 % confidence interval derived by this process is used as the error on quoted values of D-terms in this work.

The errors on the D-term phases are related to the D-term amplitudes. If one considers the D-term vector with an additive noise vector added, one would see that if the amplitude of the D-term vector is large the noise vector does not cause much change of the phase away from the phase of the D-term. If the amplitude of the D-term vector is small, then addition of the noise vector yields a resultant that can vary a lot in phase.

6.9 D-Term Values

All the D-terms (about 1400 values of phase and amplitude) derived for all antennas, all the frequencies and polarizations are given in the Tables in Appendix C. They were found to vary in amplitude from 0.0009 to 0.163. Every station has its own table and the values of the D-terms are reported with errors calculated from the Rice distribution, described in the paragraph 6.6. In the Tables for the VLBA antennas there are leakages from both the RCP channel into the LCP channel and from the LCP channel into the RCP channel, whilst for the Mark IV antennas there are the leakages from only the LCP channel into the RCP channel, because the Mark IV stations did not have dual polarization receivers.

An excerpt from the Tables in Appendix C is given in Table 6.1 . The first column is the frequency at which the D-term was determined, the second is the dimensionless amplitude of the D-term for the RCP leakage with its errors, the third is the phase in degree of the D-term for the RCP leakage with errors. The fourth and fifth columns are amplitudes and phases for the LCP leakage and are present only for the VLBA antennas since they have dual polarization receivers whilst the IVS stations do not (only RCP).

The D-term amplitudes and phases are also represented graphically in the Figures in the Appendix D.

In the case of Effelsberg, the D-terms of the receiver were known from laboratory measurements. Figure 6.14 shows the leakage measurements made in the laboratory and the leakage measurements made during this experiment. The measurement (Lochner, 1999) was made by injecting a polarized test signal into the receiver and measuring the response of the orthogonally polarized receiver output, which would have been zero for an ideal receiver.

The measurements are similar in their limited area of overlap giving additional confidence im my D-term measurement technique, although the D-terms measured for Effelsberg in this thesis are all systematically lower that those measured in the laboratory. This is most probably caused by the fact that for the laboratory measurement the receiver was in the laboratory, whilst during observations the receiver is sitting off-axis in the secondary focus. Off-axis illumination of a parabolic antenna creates asymmetric electric field distribution on the surface of the parabola which creates additional polarization leakage (Johnson and Jasik 1984), that is not included in the laboratory measurements.

Freq (MHz)	Amp. RCP	Phase RCP	Amp. LCP	Phase LCP
8228.99	$0.022^{+0.018}_{-0.030}$	$51^\circ \pm 73^\circ$	$0.023^{+0.019}_{-0.030}$	$118^\circ \pm 71^\circ$
8244.99	$0.026^{+0.020}_{-0.030}$	$52^\circ \pm 67^\circ$	$0.025^{+0.020}_{-0.030}$	$111^\circ \pm 68^\circ$
8276.99	$0.033^{+0.023}_{-0.029}$	$51^\circ \pm 58^\circ$	$0.022^{+0.018}_{-0.030}$	$120^\circ \pm 73^\circ$

Table 6.1: Amplitudes and Phases of D-term for antenna Pie Town versus frequency

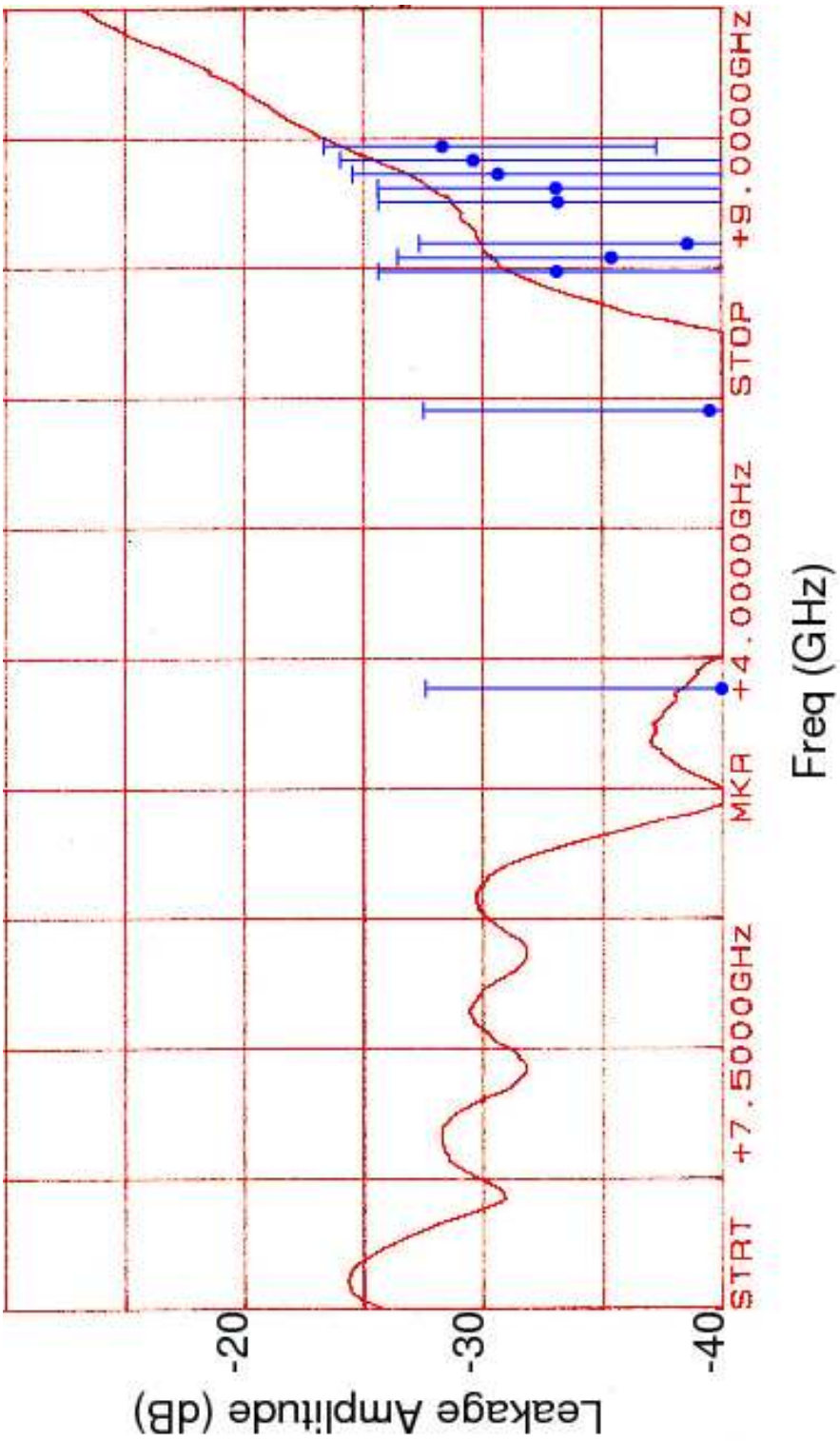

Figure 6.14: Red: Laboratory measurement of leakage power for the Effelsberg X-band receiver expressed in decibel ($20 \times log_{10}$(amplitude)) from 7500 MHz to 9000 MHz versus frequency. The curve was prepared by Lochner without error bars. Blue: Measurement of leakage made using the VLBI experiment RD0705. The error bars show the 98 % confidence interval. The two curves agree within their errors. Below -40 dB, the leakage amplitude is less than 0.01 which is negligible.

Chapter 7

Correction of the Delay for Polarization Leakage

7.1 Correction of the Leakage

Correction for the error created by the leakage in the delay was implemented within the HOPS *fourfit* program. The correction was based on Equation 3.9 and was convenient to implement after *fourfit* decoded the correlator output, but before the data were fringe fitted. More precisely, the correction was applied after the Fourier transform from single-band delay to power spectrum. The correction was a 2x2 rotation matrix that multiplied the real and imaginary visibility components for every accumulation period to rotate the phases through an angle that depends on the measured leakages and parallactic angles. First I copied the *fourfit* programs to a private version for developing the code and created an ASCII file containing the measured D-terms for all the stations (reported as station correction Tables in Appendix C) then I added to *fourfit* three functions.

- *pang.c* calculates the parallactic angle. This function is called from the main (*fourfit.c*). The code of *pang.c* is reported in Appendix E.
- *dterm_load.c* reads the D-term from file (*dterm_X-band.dat*), calculates the correction angle using Equation 3.9 for all possible combinations of antennas using the parallactic angle from *pang.c*. This function is called from *fourfit.c*. The code of *dterm_load.c* is reported in Appendix E.
- *dterm_apply.c* reads the correction angle from *dterm_load.c* for the baseline being fringe fitted and if it finds one it returns it to *norm.c*. If it does not find one, then it linearly interpolates between the nearest D-term values in frequency and returns the result to *norm.c*. The code of *dterm_apply.c* is reported in Appendix E.

The actual rotation of the visibility phases is performed in *norm.c* by adding the following code fragment to implement multiplication by a rotation matrix.

```
/*  Add a rotation to the phases to correct the d-term leakages */

/* call to dterm_apply */
      dterm_corr_ang = dterm_apply(pass, fr);
/*    dterm_corr_ang = 0.; */
/*dterm_corr_ang =  phase angle through which we will rotate the visib. vector for D-term corr*/
/*dterm_corr_ang = 0 when no D-terms are applied */
```

```
xcor_re_temp = xcor[l].re;  /* temporary storage for applying rotation matrix*/
if (sb == 1)
    dterm_corr_ang *= -1;  /* adjusting the sign in case of LSB*/
xcor[l].re = xcor_re_temp * cos(dterm_corr_ang) - xcor[l].im * sin (dterm_corr_ang);
xcor[l].im = xcor_re_temp * sin(dterm_corr_ang) + xcor[l].im * cos (dterm_corr_ang);
                          /*rotate the xcor through angle dterm_cor_ang*/
```

where *xcor[l].re* and *xcor[l].im* are the real and imaginary components of the cross correlation, i.e. they contain the contaminated visibility, *xcor_re_temp* is temporary storage for *xcor[l].re* during the phase rotation. Had *xcor_re_temp* not been used, then *xcor[l].im* would have used *xcor[l].re* after it was rotated rather than before rotation and therefore would have been wrong. Since the change in the MBD due to the correction of the D-term could have been as small as the sub-picosecond level, I increased the resolution of the MBD and visibility phases printed in the *fourfit* plot by a factor 10. This change was made in the *fourfit* function *make_postplot.c*.

7.2 Program Validation

To verify the correctness of the program modifications, I took a geodetic experiment correlated at Bonn (R1399) and considered the baseline between Westford and Wettzell. I ran *fourfit* with and without D-term correction applied, keeping the increased MBD output precision in both cases. The outputs from both runs of *fourfit* are shown in Figure 7.1

The difference in MBD was 0.6 ps for this baseline. To check whether this result was reasonable I extracted from *fourfit* the values of the D-term correction angles for the frequencies in R1399, and plotted them against frequency and performed a linear regression with least squares minimization and the result is shown in Figure 7.2. The linear regression was used since the delay is constant across the bandwidth at this range of frequencies (X-band) since the medium is non dispersive. Since the delay is the first derivative of phase with respect to frequency, then constant delay is equivalent to a straight line. The slope of this line should equal the change in MBD due to the D-term correction. The linear regression gave a delay correction of (0.6 ± 0.4) ps, which agrees with the *fourfit* result.

I also tested more thoroughly whether the rotation angle was calculated and applied to the visibilities correctly, as follows. I considered as above R1399, fringe fitted all observations by the baseline Westford-Wettzell of the source 3C 418, both with and without D-term correction applied and extracted the visibility phases in a file. The differences between the visibility phases with the D-term correction applied and the ones without the D-term correction gave the applied rotation angle. I then checked the correctness of these rotation angles using *sched*, which is a well tested and reliable program, to calculate parallactic angles. I differenced the parallactic angles for Westford and Wettzell, and used the same D-term values as were used for the D-term correction in fourfit, and calculated the correction angles using Equation 3.9. I plotted these correction angles on the top of the correction angles as calculated from the modified *fourfit* and show the results in Figure 7.3. The correction angles agree, thus validating the *fourfit* modifications for D-term corrections.

7.3 Validation of Group Delay Improvement Using RD0705

To demonstrate whether the corrections improved the group delay measurements, I ran the modified *fourfit* with and without D-term correction applied for the whole RD0705, and stored the resulting MBD measurements in a file. The algorithms for D-term measurement and D-term correction are completely different since the derivation of the D-terms is performed on the cross-hand data, and the check is performed on the parallel-hand data, so they are different correlator outputs depending on different properties of

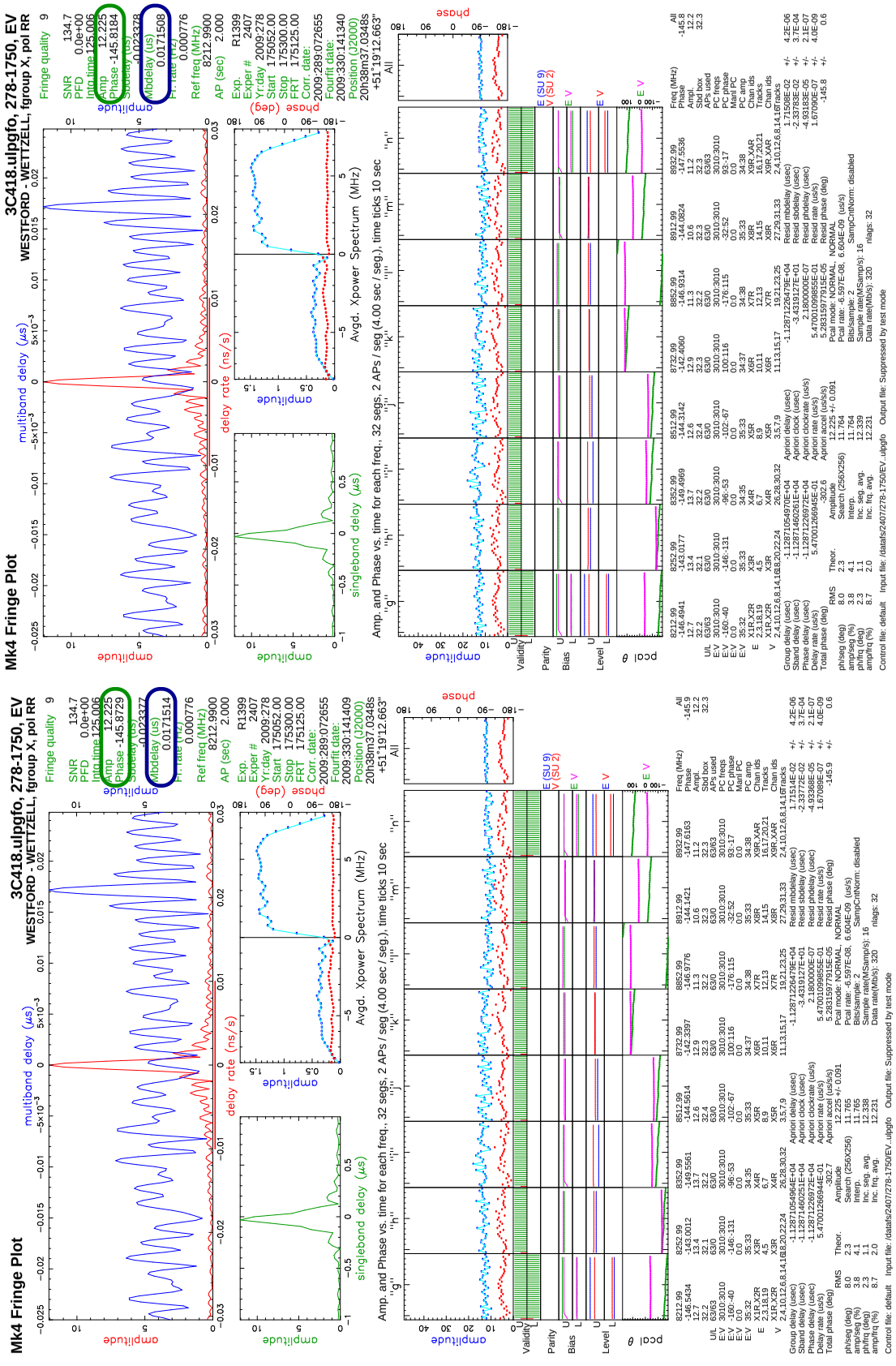

Figure 7.1: *Fourfit* plots for the baseline Westford-Wettzell for one scan in one geodetic experiment (R1399) on a strong source (3C 418) in X-band. Top: without the D-term correction. Bottom: with the D-term correction applied. The MBD is the value circled in dark blue in both plots. MBD = 0.0171508νs without D-term corrections and MBD = 0.0171514νs with D-term corrections. The difference in the MBD is 0.6 ps.

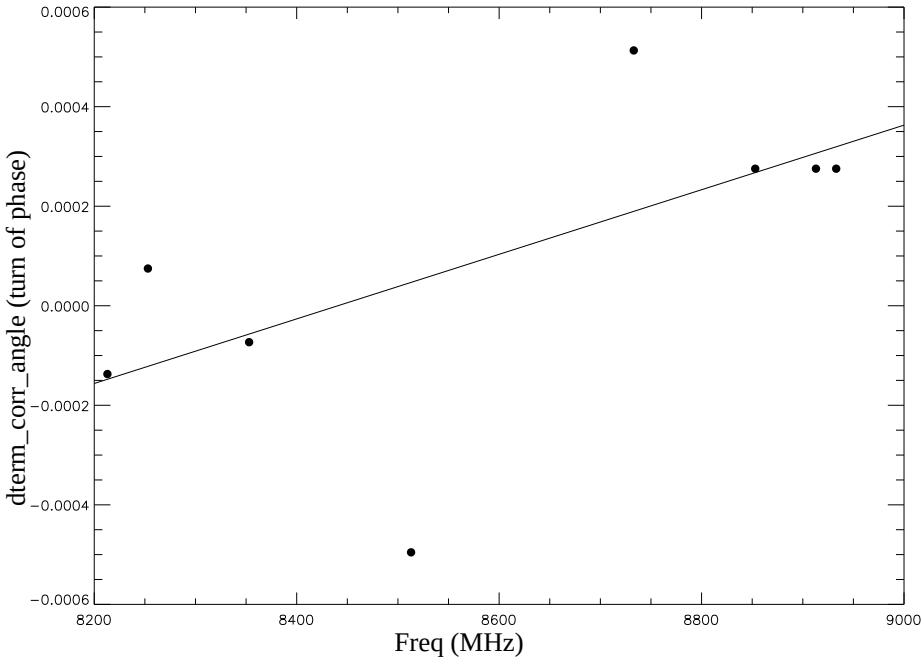

Figure 7.2: D-term correction angle versus frequency for the baseline Westford-Wettzell in the experiment R1399 on the source 3C 418 at 17:50 UT. The line is a least squares fit through the points whose gradient gives a delay correction of (0.6 ± 0.4) ps, in agreement with the value calculated by *fourfit*.

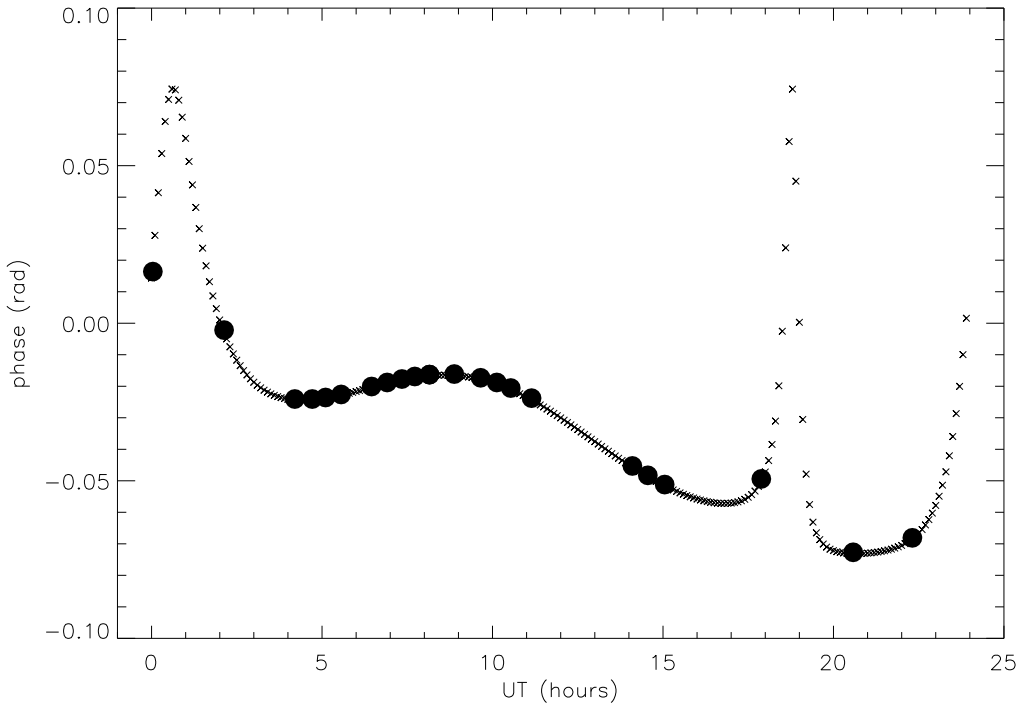

Figure 7.3: Black dots: D-term correction angle as applied by *fourfit* to the visibility phases in R1399 for the baseline Westford-Wettzell on the source 3C 418. Crosses: D-term correction angle obtained using Equation 3.9 with the parallactic angles calculated by *sched*.

the source. This already delivers a fair degree of independence between the D-term measurement and the check. One way to have the two coupled is to assume that there is a bug in CALC 8 or in the correlator harware or in correlator software that produces coupled errors in the cross-hands and the parallel hands, then the errors in the cross hands in one experiment could be anticorrelated with the errors in the parallel hands in another experiment, causing errors in the D-term measurement on RD0705 to be cancelled by errors in the parallel hands in the R1 and so go undetected. Therefore it is extremely unlikely that an error in one will be compensated by an opposite error in the other and the validation of the group delay using RD0705 data is justified.

First, I differenced the MBD with and without D-term correction applied, for each baseline and scan. The difference is the size of the correction that was applied to the data. Figure 7.4 shows the histogram of the MDB differences and Figure 7.5 shows the same difference in cumulative form. The cumulative form is presented to enable reading off the median and percentile values, which is not possible from the histogram. The median correction was 0.18 ps and the 90th percentile was 1.6 ps i.e., the corrections are mostly (90% of the time) less than 1.6 ps.

Second, I looked for a reduction in the MBD residual due to correction of the polarization leakage. Unfortunately one cannot simply compare directly the MBD before and after the D-term correction since the MBD is affected by residual correlator errors that are much larger than the effect sought. Instead, one must resort to form closure triangles of three antennas and to sum the MBDs around the triangle since this cancels all station-based errors and the result should be accurately zero except from the non-closing errors, of which the polarization leakage is expected to be the biggest. To calculate the closure MBD I wrote a C program, *cmbd.c* which identified all triangles of antennas for each scan, summed the MBD values around each triangle, and wrote the resulting closure MBD values to an output file. This program is reported in Appendix E.

Since the frequency channel spacing was not optimal to calculate the MBD, I saw very high sub-ambiguities in the resulting closure quantities. This effect was present because the observation was optimized for measuring the D-terms over a wide frequency range and was not optimized for determining the MBD. Figure 7.6 shows the MBD for a scan in RD0705. These sub-ambiguities showed up in the closure MBD and I accounted for them by wrapping them modulo 0.0625 μs, which is the ambiguity spacing for the 16 MHz channel bandwidth used. At that point, most of the good data lay close to 0 ps within 50 ps. I then created a histogram of the closure MBD values for both cases (with and without D-term corrections), in differential and cumulative forms and these are shown in Figure 7.7 and Figure 7.8.

I estimated the width of the two distributions to see whether the closure error, was noticeably reduced by the D-term correction. The width was taken as the difference between the 25th and 75th percentile and is (27.5 ± 0.3) ps in both cases, where the uncertainty is the 95% confidence interval[1] estimated by boostrap resampling (Johnson 2001). Thus the D-term correction made no detectable reduction of the closure errors. However, this experiment (RD0705) was not scheduled for the purpose to deliver precision delay measurements, therefore the channel spacing was not optimal to deliver high resolution MBD. Thus there was not enough sensitivity to detect a median change in the MBD of 0.18 ps as calculated above when the closure MBD values are distributed around 0 ps with an inter-quartile range of 27.5 ps, as it will be expalined in detail in section 7.4. RD0705 produced only 26400 useful closure MBD measurements, from 12 antennas per scan, 480 scans, and with the number of independent closure measurements among n stations being $\frac{1}{2}n(n-1)-(n-1)$ (Cornwell and Fomalont 1999). This was not enough to detect a 0.18 ps change in MBD.

The width of the closure error distribution was found to be 27.5 ps (inter-quartile range), therefore the leakage is not the dominant error among the factors contributing to the total closure error, thus I considered the other two most likely non-closing errors, i.e the source structure and the bandpass filter

[1] I.e. there is a 5 % probability that the true width differs by more than the ± 0.3 ps uncertainy limit from the estimated width of 27.5 ps due to a chance statistical fluctuation

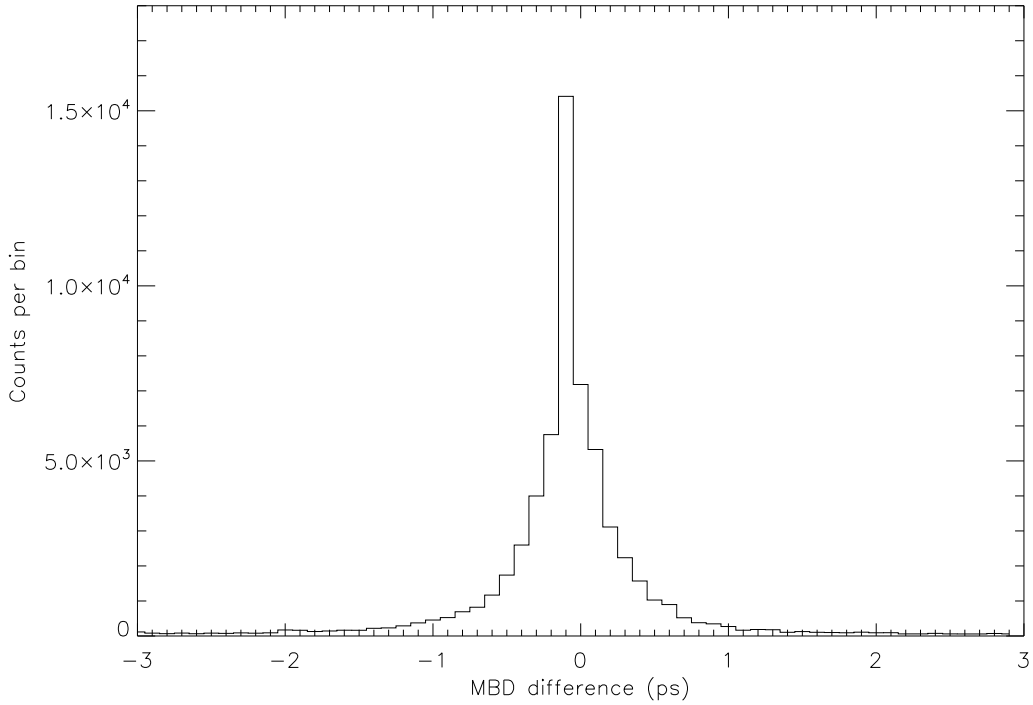

Figure 7.4: Histogram of the MBD change on OQ 208 in RD0705 caused by correcting the leakage. Bin size 0.1 ps

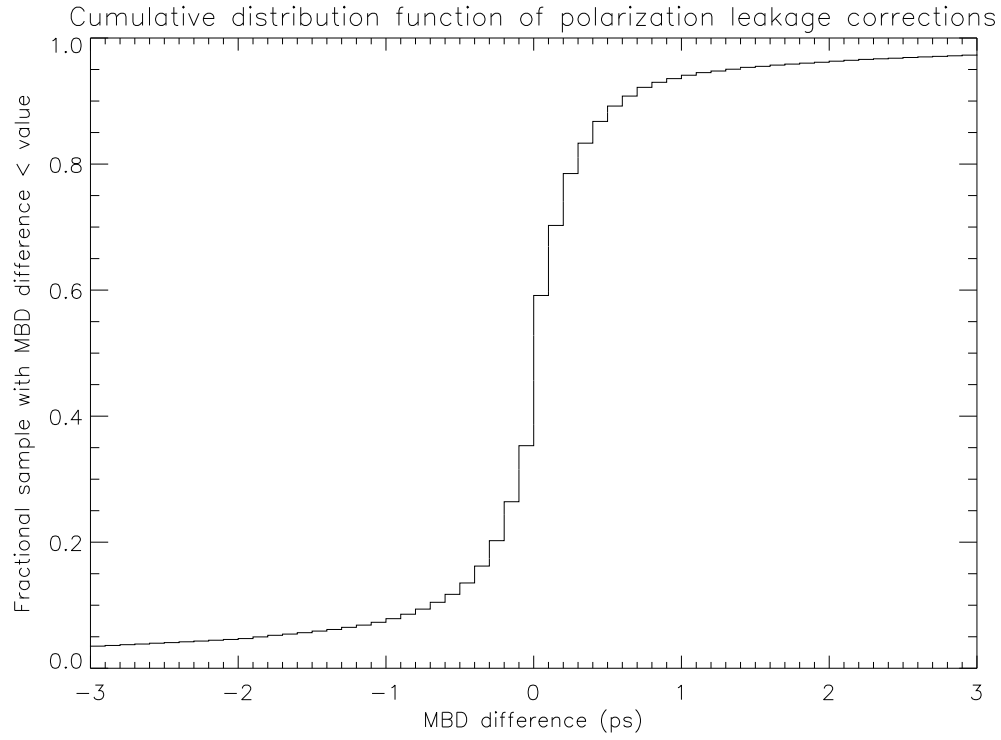

Figure 7.5: Cumulative histogram of the MBD change on OQ 208 in RD0705 caused by correcting the leakage.

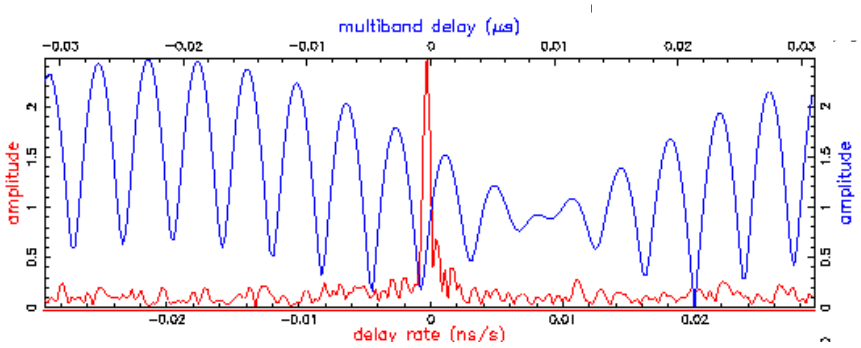

Figure 7.6: MBD function for one scan for RD0708 for the source OQ 208 at X-band. The MBD function has high sidelobes due to limited frequency sampling.

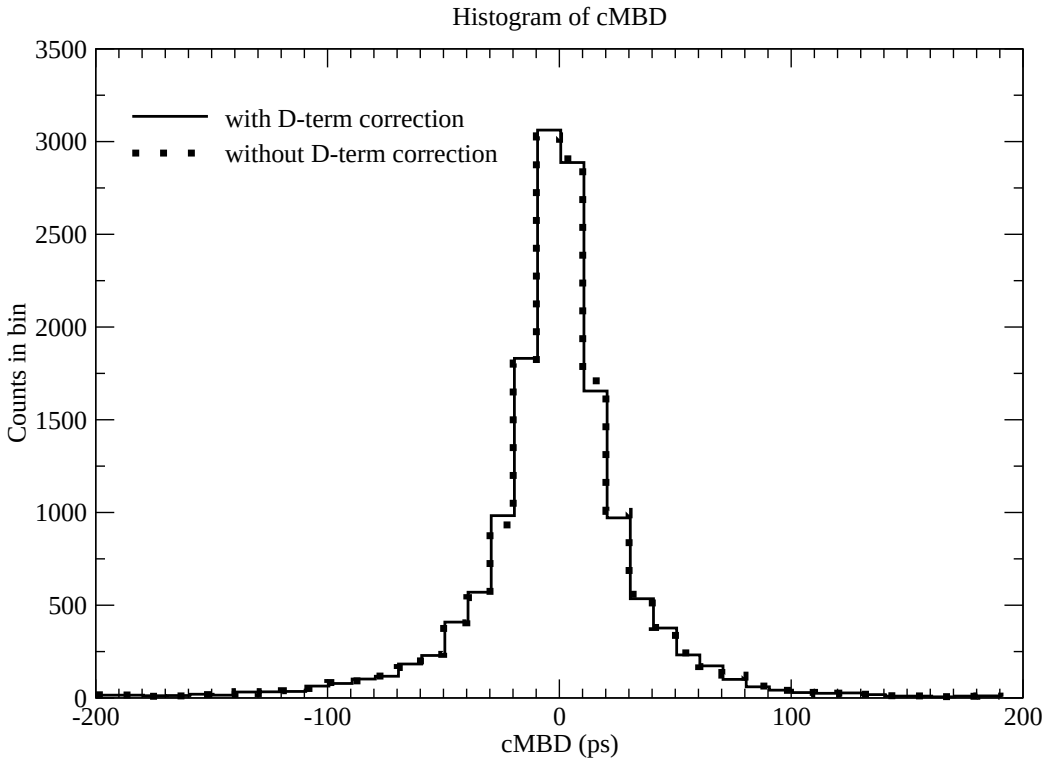

Figure 7.7: Histogram of the closure MBD on OQ 208 in RD0705 with and without D-terms correction applied.

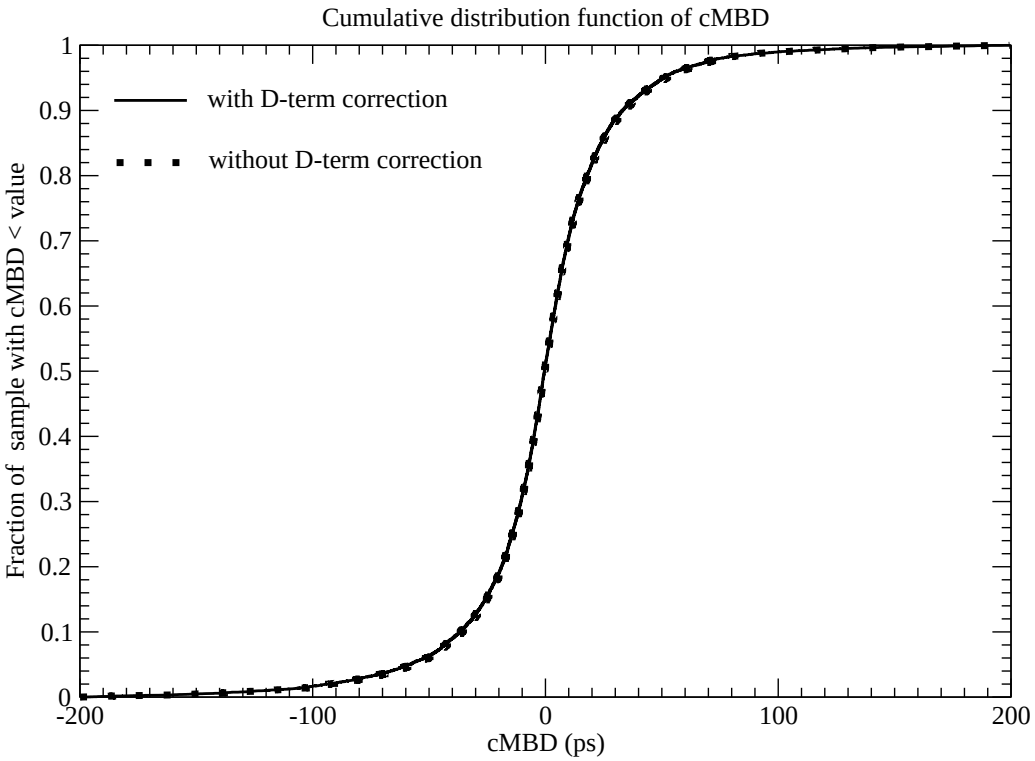

Figure 7.8: Histogram of the closure MBD on OQ 208 in RD0705 with and without D-terms correction applied.

shape.

7.3.1 Source Structure

The target source was OQ 208, which is not point-like, but has a small second component, as is visible in Figure 6.5 in the bottom right part of the plot. Following the recipies of Charlot (1990), I could calculate the effect of the source structure on the closure delay. The main component is located at the phase centre in the map, therefore after the correlator delay model was applied, the main component has zero delay. The secondary component, on the contrary, has an angular offset from the main component of about 8 mas, therefore the residual delay after the correlator model was applied is non-zero. Figure 7.9 shows the geometry of the observation. The source is at infinity, therefore the radio waves arriving at the telescopes A and B are parallel wavefronts. The angle between the radio waves incoming from the main component (solid lines) and from the secondary component (dotted lines) is equal to the separation of the two components, i.e. 8 mas. The delay from the secondary component is

$$\tau = \frac{b \tan \alpha}{c} \tag{7.1}$$

where b is the distance between the two stations, and α is the angle between the baseline and the line from station B to the point D. By geometry, $\alpha = 8$ mas or 3.88×10^{-8} radians. Considering the longest baseline with mutual visibility of about 6000 km and considering the worst case when the projection of the vector separation between the two components is parallel to the baseline, Equation 7.1 lead to a delay of 776 ps. The response of the interferometer to this geometry is the flux-density-weighted average of the two wavefronts. The flux density of the main component is 1.6 Jy and the flux density of the secondary component is 0.16 Jy, as derived in the data analysis. Given a weight $w_1 = 1.6$ for the main component

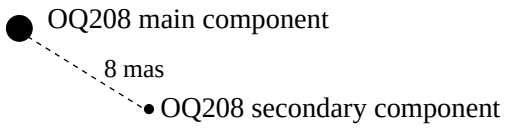

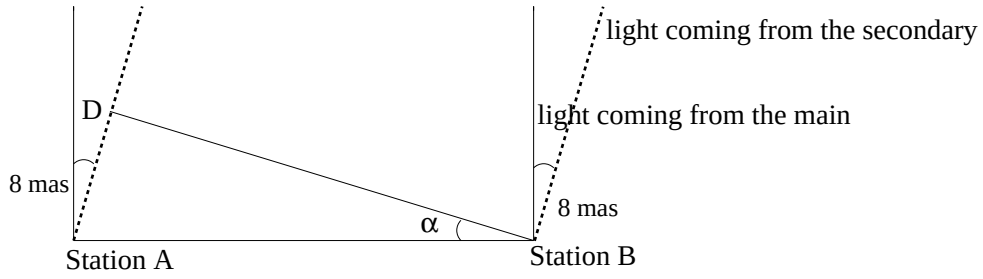

Figure 7.9: Cartoon describing the geometry of an observation where the source is not point-like, but has a secondary component with non-zero delay.

and a weight $w_2 = 0.16$ for the secondary component, then the weighted average is

$$\sum_{n=1}^{2} \frac{w_n \tau_n}{\sum_{n=1}^{2} w_n} \tag{7.2}$$

where the sum goes with the number of components, which in this case is two. The amount by which the delay is different from zero on this 6000 km baseline is then 70 ps.

The best case happens when the projection of the vector separation between the two components is perpendicular to the baseline, in which case the delay error is 0 ps independent from the baseline length. In a median case, the baseline length is 4000 km and the projection of the vector separation between the two components is 45° relative to the baseline. Using Equations 7.1 and 7.2 in this case leads to a delay of 33 ps.

With a simulation using the AIPS task DTSIM, I generated a dataset using the same characteristic present in the real observation (same antennas, same source), though without any noise added, to see the effects of the source structure on the closure quantities. I took a representative longer baseline across the Atlantic from the VLBA station North Liberty, to Noto and chose a second VLBA station (Los Alamos) to form a triangle. I calculated the closure phases on this triangle every second for the whole duration of the experiment on the source OQ 208 and the largest value was found to be 100° corresponding to a delay of 33 ps when observing at X-band, which is acceptably close to the 27.5 ps inter-quartile range of the closure MBD distribution that was found during data reduction. Thus source structure can cause closure errors in the MBD of similar magnitude of those seen in the analysis of this experiment.

7.3.2 Bandpass Filter Shape Missmatch

The bandpass filter in the ideal case has a flat passband for both phase and amplitude but is never achievable in real cases. Thompson and D'Addario (1984) showed that a linear amplitude slope across the passband gives almost zero phase error and that a sinusoidal ripple in the amplitude across the passband can cause at most 0.02° error. The most probable source of errors comes from phase ripple across the filter filter passbands. This particular case is not treated by Thompson and D'Addario (1984), therefore I did it for this specific observation. I generated within a C-program, three sinusoids with amplitudes of 3.5°, 10° and 15° to simulate the phase ripples across the passband actually found to be present by inspecting the data. This simulated the bandpass at each antenna in a triangle. I calculated the closure phase around the triangle calculating the phase differences between antennas for each frequency within the bandpass and vector-averaging the phase differences over the whole frequency range within the passband. I then generated 100 such cases with randomly selected ripple periods and ripple phases, though constrained to lie within the range of values actually seen in the data. I recorded the maximum value of non-closing phase, which was 1.43° (closure delay of 5.5 ps when observing at X-band) and the median value of non-closing phases, which was 0.96° (closure delay of 3.7 ps at X-band).

From this I can conclude that the source structure accounts for most of the closure MBD spread, that the bandpass effect on closure is 13 % of the total spread, and that the polarization leakage effect is below 2 % of the total spread.

7.4 χ^2 Test

To test whether the closure MBD distributions before and after D-term correction (Figures 7.4 and 7.5) differ I applied a χ^2 test which demonstrated that there is no statistically significant difference between the two distributions. I then tried to see whether this result would have changed, had I considered only four stations with the largest D-terms (Matera, Noto, Westford and Onsala) and arrived at the same conclusion that there is no statistically significant difference.

The power of the χ^2 test to distinguish the two distributions was estimated from a numerical simulation. For the simulation I took the measured closure MBD distribution and made a scaled copy of it that had progressively broader width on each trial. Then I used the χ^2 test to compare the measured and scaled distributions. The χ^2 test yielded a significant difference (95% significance) when the width of the distribution changed by 15%. This means that the total closure errors would have to be reduced by 15% to be noticeable. The polarization leakage is only one of many non-closing error (see Sections 3.3, 7.3.1 and 7.3.2) and since the error sources do not add linearly, the effect of the polarization leakage on the MBD needs to be more than 15% of the total closure errors to be detectable. The open question is then how large must be this number. To answer the question one must understand the way the errors combine, which requires knowledge of the error distribution. It is reasonable to assume that the distribution of the closure MBD correction has the same shape as, and is $\sqrt{3}$ times wider than the distribution of the MBD correction. This is the case because the closure MBD correction is the sum of three MBD corrections on the three baseline constituting a triangle. It is also reasonable to assume that the distribution of the other non-closing errors is that of the distribution of the closure MBD after the leakage corrections have been applied (Figure 7.7). These assumptions formed the basis for calculating the propagation of errors. To combine the errors without assuming that the data are Gaussian distributed, one would need to convolve the distribution of the MBD correction with the distribution of the closure MBD. This is though unnecessarily complicated, since it is a good approximation to assume that the two distributions are Gaussian and use the simplest parametric statistic. This statement was proven by comparing the width estimate of the closure MBD histogram from parametric and non-parametric estimators. The width, using a non-parametric estimator (the inter-quartile range; Weisstein (1999)), was 27.5 ps. The width, using a parametric estimator (the inter-quartile range of a Gaussian that was fit to the closure MBD distribution), was 24.2 ps (corresponding to a dispersion of 17.5 ps). The two inter-quartile ranges differ

by 10%, which represents the error that one would make by assuming that the distribution is Gaussian. Since this difference is acceptably small, I used Gaussian statistics for answering the question of how large must be the effect of the polarization leakage on closure MBD to be detectable when corrected. I considered two independent Gaussian error sources, one representing the effect of the polarization leakage on closure MBD and the other representing all the other non-closing errors that affect closure MBD. These sum together to give the measured dispersion of 17.5 ps. Correcting the polarization leakage would have to reduce this dispersion by 15% to 14.9 ps for the change to be detectable by the χ^2 test. This means the polarization leakage would have to have a dispersion of 9.2 ps considering that Gaussian errors add quadratically.

Chapter 8

Consideration on Polarization Leakage for VLBI2010 Receivers

Having developed an analytical understanding of how D-term corrupts the delay, I applied it to develop a guideline for polarization purity in the new VLBI2010 receivers presently being designed. This developement was done using a numerical simulation although one could have performed this investigation purely theoretically.

VLBI2010 (Niell et al 2007) identifies a number of ways to improve the precision of geodetic observables. Within VLBI2010 there is a recommendation on new receivers, which are intended to span 16 GHz bandwidth. Typical design for feeds in VLBI2010 were discussed at the meeting *Future Radio Frequencies and Feeds*[1] held in Wettzell in 2009. Discussed were the *11 feed* designed by Onsala (Olsson et al 2006), the multiband corrugated horn presented by Göldi and the quad-ridge horn (ETS-Lindgren 3164-05 model). These feeds have cross polarization levels that vary between -10 dB to -35 dB, which is equivalent to D-term amplitudes between 0.3 and 0.02.

Given these feed properties one can estimate whether the leakage is likely to cause problems for the geodetic observables. If the feed is chosen to be linearly polarized I cannot make any statement about tolerable leakage levels. That is because the effect of D-terms on the visibilities is totally different from that of circularly polarized feeds and is outside the scope of this study. If the feed is chosen to be circularly polarized, I can give an upper limit to allowable leakage by considering the case of 11 GHz of spanned bandwidth and the worst D-term amplitude of 0.3. For the D-term phase gradient with frequency I evaluated many possible gradients to find the worst possible case that yields the largest delay error. The calculation was done numerically by vector addition at each frequency of the visibility vector and leakage contamination with the D-term phase rotated through an angle that is frequency dependent. The delay was derived following Corey and Titus (2006) approach but trying various parallactic angle differences. Figure 8.1 shows how the delay error depends upon the D-term phase gradient and parallactic angle.

I found that the worst case delay error range between 2.5 ps and 3.4 ps depending on the parallactic angle difference. Since 3.4 ps corresponds to 1.1 mm, this is quite close to the VLBI2010 goal of 1 mm total error and therefore the leakage should be kept smaller than this worst case.

Therefore, although the leakage is high in some feed designs, the fact that the bandwidth spanned is huge reduces the contribution to a value that is below the detectability of the leakage in the present geodetic measurable. Future improvements through the VLBI2010 project may reduce the uncertainties to the point that the polarization leakage effect becomes a relevant source of error in the delay determination.

To ensure that the polarization leakage is low enough for 1 mm precision for VLBI2010, one should design the new feeds so that their polarization leakage characteristic is sufficiently low as it is estimated below for circularly polarized feeds.

[1] http://www.wettzell.ifag.de/veranstaltungen/vlbi/frff2009/frff2009.html

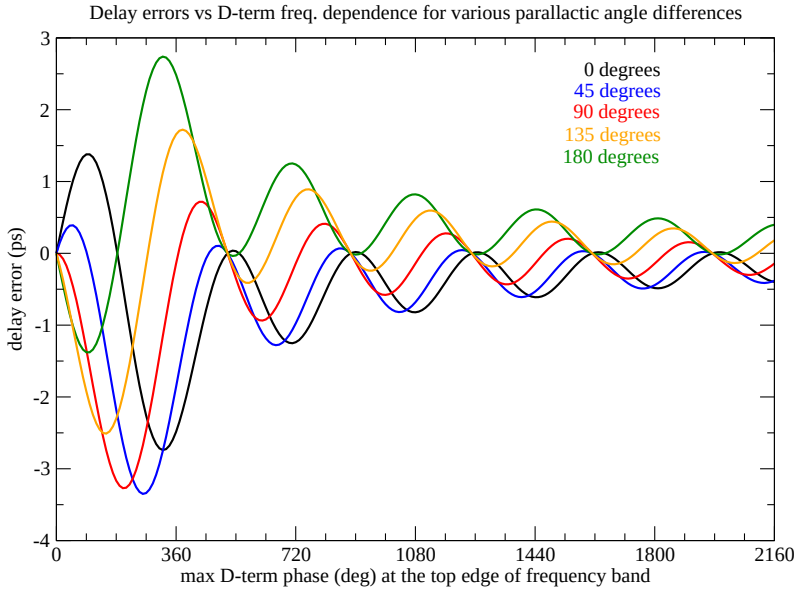

Figure 8.1: Effect on the delay due to polarization leakage produced by a linear gradient of D-term phase difference between two stations with D-term amplitude of 0.3 and 11 GHz of spanned bandwidth for various parallactic angles.

I began by considering that there are some ten independent sources of errors such as troposphere, thermal expansion of telescopes, instrumental effects and each of them should contribute at most $\frac{1 \text{ mm}}{\sqrt{10}} = 0.3$ mm. In the explicit case of the polarization leakage, there are two effects that contribute to the delay error: the phase gradient across the spanned bandwidth and the D-term amplitude. Taking the worst case of a phase gradient of 260° across the spanned bandwidth of 11 GHz and assuming that both antennas have the same polarization leakage amplitude, then the D-term amplitude that yields 0.3 mm delay perturbation is 0.17 corresponding to -15 dB. If the feed is built better than this, the delay error will be less than 0.3 mm in all cases.

Chapter 9

Conclusion

9.1 Summary of Results

In this PhD thesis I determined the effects of polarization leakage on the delay observables in geodetic VLBI using one dedicated observation with a 19-station global VLBI array consisting of the 10 VLBA and 9 geodetic VLBI stations. I found that the leakage of signal from one polarization channel to the opposite polarization channel (the D-term) had a dimensionless amplitude that varied from 0.0009 to 0.1637 and phases that mostly varied very little with frequency over the range 8212.99 MHz to 8932.99 MHz. The errors on these quantities were calculated using the Rice statistic and vary for every D-term measurements. The phase change of the leakage with frequency causes an error in the geodetic delay determination which, from the measured leakage dependence on frequency was found to be 0.18 ps and the 90th percentile was 1.6 ps, i.e. the delay error due to leakage is less than 1.6 ps in 90 % of the cases.

To look for a reduction in the MBD residuals due to correction of the polarization leakage, one must resort to form closure triangles of three antennas and to sum the MBDs around the triangle since this cancels all station-based errors and the result should be zero except for the non-closing errors. The width of the closure error distribution was found to be 17.5 ps, therefore the leakage is not the dominant error among the factors contributing to the total closure error. Future works should, thus, concentrate on identifying and reducing the dominant error sources. Typical sources of non-closing errors are:

- source structure, and
- different filter shapes at different stations

Having developed this analytical understanding I applied it to develop a guideline for polarization purity in the new VLBI2010 receivers presently being designed. Within VLBI2010 there is a preliminary specification for the new receivers to span 16 GHz bandwidth. Given the measured properties of the feeds being considered for VLBI2010, one can estimate whether the leakage is likely to cause problems for the geodetic observables. Although the leakage is high in some feed designs, the fact that the bandwidth spanned is huge reduces the contribution to a value that is below the detectability of the leakage in the present geodetic measurable. Future improvements through the VLBI2010 project may reduce the uncertainties to the point that the polarization leakage effect becomes a relevant source of error in the delay determination. To ensure that the polarization leakage is low enough for 1 mm precision (i.e. 0.3 mm error contribution from polarization leakage) for VLBI2010, one should design the new feeds so that their polarization leakage characteristic is below -15 dB.

9.2 Comparison with Previous Results

The results of this project are in agreement with the results obtained by Corey and Titus (2006) from their measured D-term dependency on frequency. Corey and Titus (2006) found that polarization leakage introduces an error on the MBD at X-band of 1.0 ps (0.3 mm) at the VLBA antennas and up to 9 ps (2.7 mm) at the geodetic stations for 360 MHz bandwidth. I found that polarization leakage introduced an error of 0.6 ps in the MBD on the baseline Westford-Wettzell (geodetic stations) for a bandwidth of 720 MHz, or 6 ps had the bandwidth been 360 MHz. If the mean value of the error caused by the D-terms is as big as that calculated by Corey and Titus (2006) for the baseline Westford – Kitt Peak of (7 ps), then the improvement would be statistically detectable with 1300 independent closure MBD measurements. This is clearly not the typical case, or I would have seen it in this study with the 26400 closure triangles considered.

Since this value is smaller than the 14 ps derived in the theoretical work of Rogers (1991), then Rogers might have been pessimistic in both his assumptions of a phase gradient over 360 MHz and of a nominal D-term amplitude of about 0.17 for all the antennas, which I measured to be the case only for the worst antenna.

Chapter 10

Summary

Geodetic VLBI delivers baseline length and Earth orientation parameter measurements, which offer the most viable and precise way to study Earth crustal and core dynamics and to support space navigation. The geodetic observable obtainable from VLBI measurements is the propagation time difference of electromagnetic radiation from the quasars to the antennas measured as the phase slope versus frequency (group delay). Within the past 35 years the precision of the geodetic measurements has improved by a factor of 100, from metre precision (Hinteregger et al 1972) down to a few millimetre precision (Niell et al 2007) opening possibilities for the geophysicists to study the Earth's interior dynamics and climatology (Chao 2004). Still, the requirement to increase the precision drives geodesists to eliminate, where possible, factors that hinder their goal of reaching the sub-millimetre level (Niell et al 2007). Among these factors, the primary limitations come from the atmospheric and ionospheric refraction, source structure and instrumental effects such as polarization leakage (D-term). The polarization leakage has so far been considered to be one of the biggest error sources not yet corrected in the geodetic analysis.

The polarization leakage corrupts the phase in a way that varies with frequency, and since the group delay is the first derivative of the phase delay with respect to frequency, the polarization leakage corrupts also the group delay. That polarization leakage affects the VLBI measurements has been known for more than a decade but both the geodetic and astronomical communities have conducted only a few studies to either model theoretically or measure the contamination of the observables by polarization leakage. The need for new measurements arose because in the previous studies only approximate values were established: the observed sources were assumed to be unpolarized, the bandwidth spanned for the geodetic antennas by Corey and Titus (2006) was only 360 MHz of the 720 MHz available at X-band, and some stations upgraded the receivers since those measurement were made.

In this study I made a 24 hour observation with some IVS and the 10 VLBA stations and analyzed the data assuming that the observed sources could be polarized. For this reason, I first made images of the sources to determine simultaneously the source structure, the intrinsic polarization and the polarization leakage. I spanned the so-called geodetic wide-band that is from 8212 MHz to 8932 MHz at X-band and from 2225 MHz to 2365 MHz at S-band. I also measured the polarization leakage more densely in frequency, every 16 MHz, for better interpolation of the leakage vectors across the whole bands and in case the geodetic frequency sequence is changed in the future. Nearly 60 frequencies divided in 15 frequency-setups were observed. To obtain the best results possible, I pushed the Mark IV stations beyond their standard usage. The preparation of the observations required a deep understanding of the VLBI data acquisition racks and their capabilities and was defined the most complex VLBI observation made sofar.

Polarization leakage was detected by the following procedure. In the absence of leakage the signals received in the LCP channel and RCP channel are uncorrelated Gaussian noise processes and cross correlation between them will yield no coherence. If leakage is present then some of the signal in one

polarization channel will add to the signal in the other polarization channel. By cross-correlating the contaminated LCP channel at one antenna and the contaminated RCP channel at the other antenna one will find coherence caused by the LCP in the LCP channel when correlating against the LCP that leaked into the RCP channel at the other antenna. To disentangle the intrinsic polarization of a source and the polarization leakage terms, one needs a wide parallactic angle coverage because the electric vector intrinsic to the source will not rotate as the dipoles rotate whilst the vectors describing the leakage terms will rotate with the dipoles. Geodetic stations mostly have only RCP, but measurements of the leakage for these stations are still possible if the antenna at the other end of the baseline has dual-polarization receivers. Therefore, I used the 10 VLBA antennas since they are among the few antennas that have dual polarization capability at S-band and X-band and their hardware is carefully designed for VLBI observations. In addition, 10 geodetic antennas were used as a test sample to measure the polarization leakage. All the different frequency setups designed in this study were correlated at the Bonn correlator and the correlation was done between all possible combinations of polarization (i.e. RCP against RCP, LCP against LCP, RCP against LCP and LCP against RCP).

The correlated data were subsequently imported into the Astronomical Image Processing System (AIPS) and processed up to and including the determination of the polarization leakage. The choice of AIPS was made because it implements the algorithms required, namely amplitude and phase calibration, fringe fitting, imaging, deconvolution, self-calibration and leakage determination solving simultaneously for source polarization.

Errors were estimated on the leakages within AIPS by simulating a dataset with the same leakage characteristics as the original one. The simulated dataset was then analyzed in the same way as for the real data. The leakages obtained from the simulated dataset were compared with the leakages derived by the real data to estimate errors from the repeatability. This approach was used since the experiment is unique and cannot be reobserved without considerable efforts to check the repeatability.

Correction of geodetic data for the error created by the leakage in the delay was implemented within the HOPS *fourfit* program. The correction was based on Equation 3.9 and it was convenient to implement it after *fourfit* decoded the correlator output, but before the data were fringe fitted. The correction was a 2x2 rotation matrix that multiplied the real and imaginary visibility components to rotate the phases through an angle that depends on the measured leakages and parallactic angles. First I created an ASCII file containing the measured D-terms for all stations (reported as station correction tables in Appendix C). Then I added to *fourfit* three functions:

- *pang.c* calculates the parallactic angle. This function is called from the main (*fourfit.c*). The code of *pang.c* is reported in Appendix E.

- *dterm_load.c* reads the D-terms from file (*dterm_X-band.dat*), calculates the correction angles using Equation 3.9 for all possible combinations of antennas using the parallactic angle from *pang.c*. This function is called from *fourfit.c*. The code of *dterm_load.c* is reported in Appendix E.

- *dterm_apply.c* reads the correction angle from *dterm_load.c* for the baseline being fringe fitted and if it finds one it returns it to *norm.c*. If it does not find one, then it linearly interpolates between the nearest D-term values in frequency and returns the result to *norm.c*. The code of *dterm_apply.c* is reported in Appendix E.

The actual rotation of the visibility phases is performed in the existing, but slightly modified, *fourfit* function *norm.c*.

To verify the correctness of the program modifications, I took a geodetic experiment correlated at Bonn (R1399) and considered the baseline between two stations, Westford and Wettzell. I ran *fourfit* with and without D-term corrections applied. The difference in MBD was 0.6 ps for a scan within these two stations. To check this result I extracted from *fourfit* the values of the D-term correction angles for the frequencies in the R1, and plotted them against frequency and performed a linear regression with

least squares minimization using software that is independent of *fourfit*. The regression gave a delay correction of (0.6 ± 0.4) ps, which agrees exactly with the *fourfit* result.

To demonstrate whether the corrections improved the group delay measurements, I ran the modified *fourfit* with and without D-term correction applied for the whole RD0705. First, I differenced the MBD with and without D-term correction applied, for each baseline and scan. The difference is the size of the correction that was applied to the data. The median correction was 0.18 ps and the 90th percentile was 1.6 ps i.e., the corrections are mostly (90% of the time) less than 1.6 ps. Second, I looked for a reduction in the MBD residual due to correction of the polarization leakage. Unfortunately one cannot simply compare directly the MBD before and after the D-term correction since the MBD is affected by residual correlator errors that are much larger than the effect sought. Instead, one must resort to form closure triangles of three antennas and to sum the MBDs around the triangle since this cancels all station-based errors and the result should be accurately zero except from the non-closing errors, of which the polarization leakage is expected to be the biggest. However the leakage correction measured in this investigation, was found to make no detectable reductions in the closure errors.

The results of this project are in agreement with the results obtained by Corey and Titus (2006) from their measured D-term dependency on frequency.

A χ^2 test comparing the closure errors before and after polarization correction is unable to detect the improvement due to leakage effects smaller than 9.2 ps and so was not sensitive enough to detect the improvement made by polarization leakage corrections. Since the median value of the leakage correction was found to be 0.18 ps and the width of the closure error distribution was found to be 17.5 ps, the leakage is not the dominant error among the factors contributing to the total closure error. Future works should concentrate in identifying and reducing the other non-closing error sources, which are:

- source structure, and
- filter shapes

Having developed this analytical understanding I applied it to develop a guideline for polarization purity in the new VLBI2010 receivers presently being designed. Within VLBI2010 there is a preliminary specification for the new receivers to span 16 GHz bandwidth. Given the measured properties of the feeds being considered for VLBI2010, one can estimate whether the leakage is likely to cause problems for the geodetic observables. Although the leakage is high in some feed designs, the fact that the bandwidth spanned is huge reduces the contribution to a value that is below the detectability of the leakage in the present geodetic observable. Future improvements through the VLBI2010 project may reduce the uncertainties to the point that the polarization leakage effect becomes a relevant source of error in the delay determination. To ensure that the polarization leakage is low enough for 1 mm precision (i.e. 0.3 mm error contribution from polarization leakage) for VLBI2010, one should design the new feeds so that their polarization leakage characteristic is below -15 dB (or amplitude of 0.17), which correspond to the amplitude seen for the worst case during this work. Considering that the feeds considered for VLBI2010 have cross polarization levels that vary between -10 dB to -35 dB (or amplitudes from 0.3 to 0.02) the goal of reaching -15 dB is feasible.

Appendix A

Scheduling, Observation and Correlation

A.1 *Fourfit* Plots

Examples of the fringe-fitted data are shown in *fourfit* plots in Figures A.1, A.2 and A.3. Figure A.1 is the cross-correlation between Westford (Wf) and North Liberty (Nl) on one scan, 220 s, RCP against RCP for the target source OQ 208. The left figure represents the S-band and the right figure is the X-band. In both cases there is good correlated signal.

As a last example, Figure A.3 shows the presence of RFI due to a known satellite transmission. The fringe fit plot shown is, in this case, an autocorrelation of Nl, because the effect is much more easily recognized in the autocorrelation spectra than in the cross-correlation spectra. The broadband RFI is present in the USB of the spectrum: its amplitude is so high compared to the amplitude of the radio astronomical signal, that it dominated the signal. In such cases the data must be discarded.

A.2 Explanation of a *Fourfit* Plot

The fourfit plot is explained in detail by Bertarini et al (2009) and is summarized here. Please refer to the top panel of Figure A.1. In the top plot within that panel, the red line shows the amplitude of the cross-correlation coefficient versus the delay rate (DR) expressed in ns/s, i.e. how fast the fringes move away from the delay tracking centre due to correlator model error. After fringe fitting, the peak is centred at zero. The blue line in the top plot is the amplitude of the cross-correlation coefficients versus the multiband delay (MBD) expressed in microseconds (note it is present only for the X-band, where more than one BBC channel is present). The MBD is the geodetic observable and is given by the slope of the visibility phase versus frequency over the whole spanned bandwidth. In the cases where only one BBC channel is used (like the S-band), the MBD is equal to the singleband delay (SBD) and is not drawn. The plot on the left on the second row is the amplitude of the cross correlation coefficient versus lag, also called SBD, expressed in microseconds, averaged over all the BBCs within the band. The offset of the peak from zero indicates residual correlator model errors. The plot on the right on the second row represents the Fourier transform of the SBD averaged over all BBCs within the band (plot on the left of that row). The plot is itself divided into two subplots representing the lower sideband (LSB) and upper sideband (USB). The blue line is the amplitude of the frequency spectrum in units of correlation coefficient times the number of lags time 10000 and the red line is the phase of the frequency spectrum expressed in degrees.

To fringe fit the data with HOPS means to find the maximum amplitude of the correlator coefficient

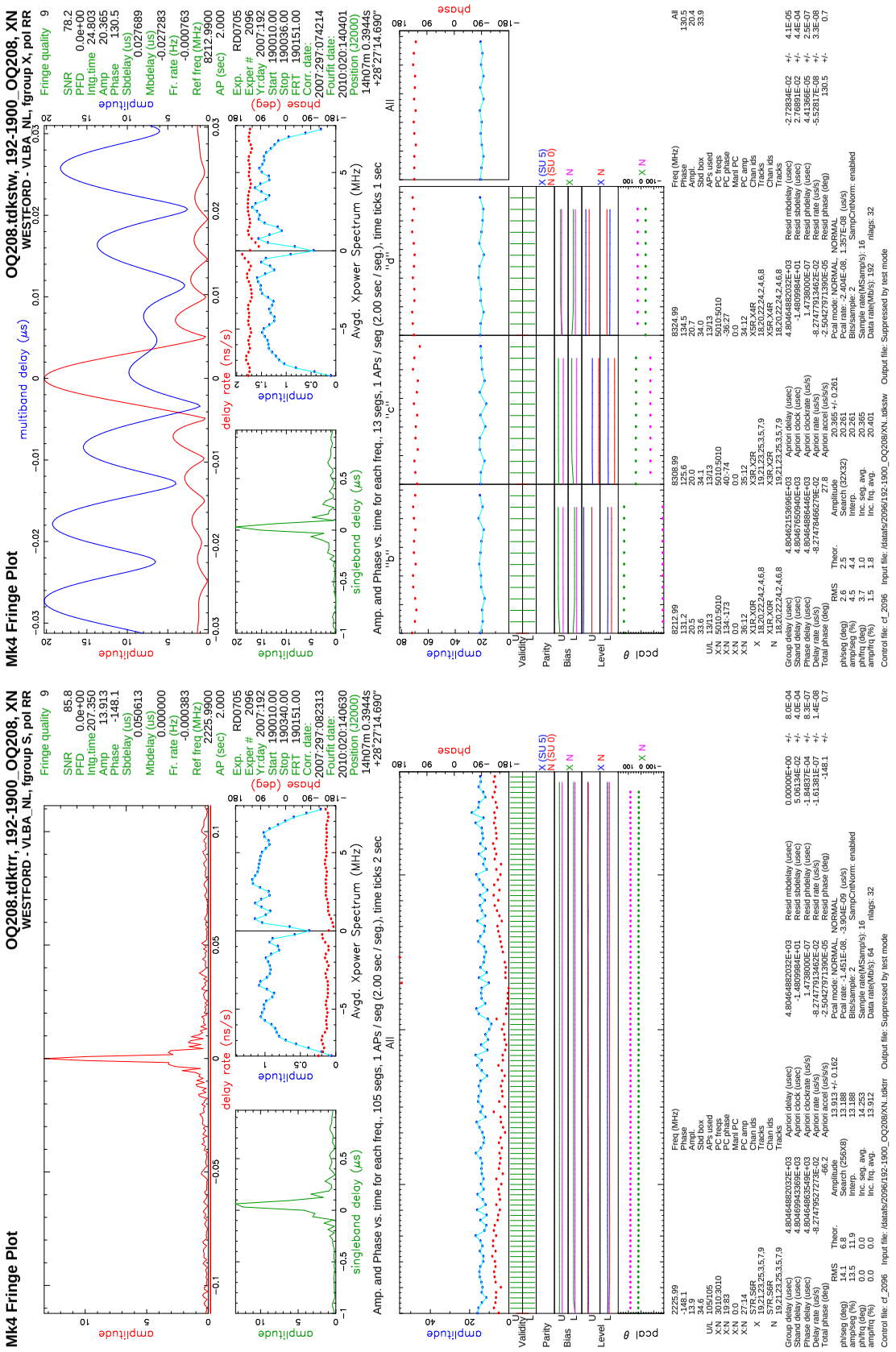

Figure A.1: HOPS fringe plots for one scan on OQ 208. The polarization is RCP and the antennas are Westford (Wf) and North Liberty (Nl). The bottom plot is the S-band and the top plot is the X-band. Both bands have strong fringes with high SNRs.

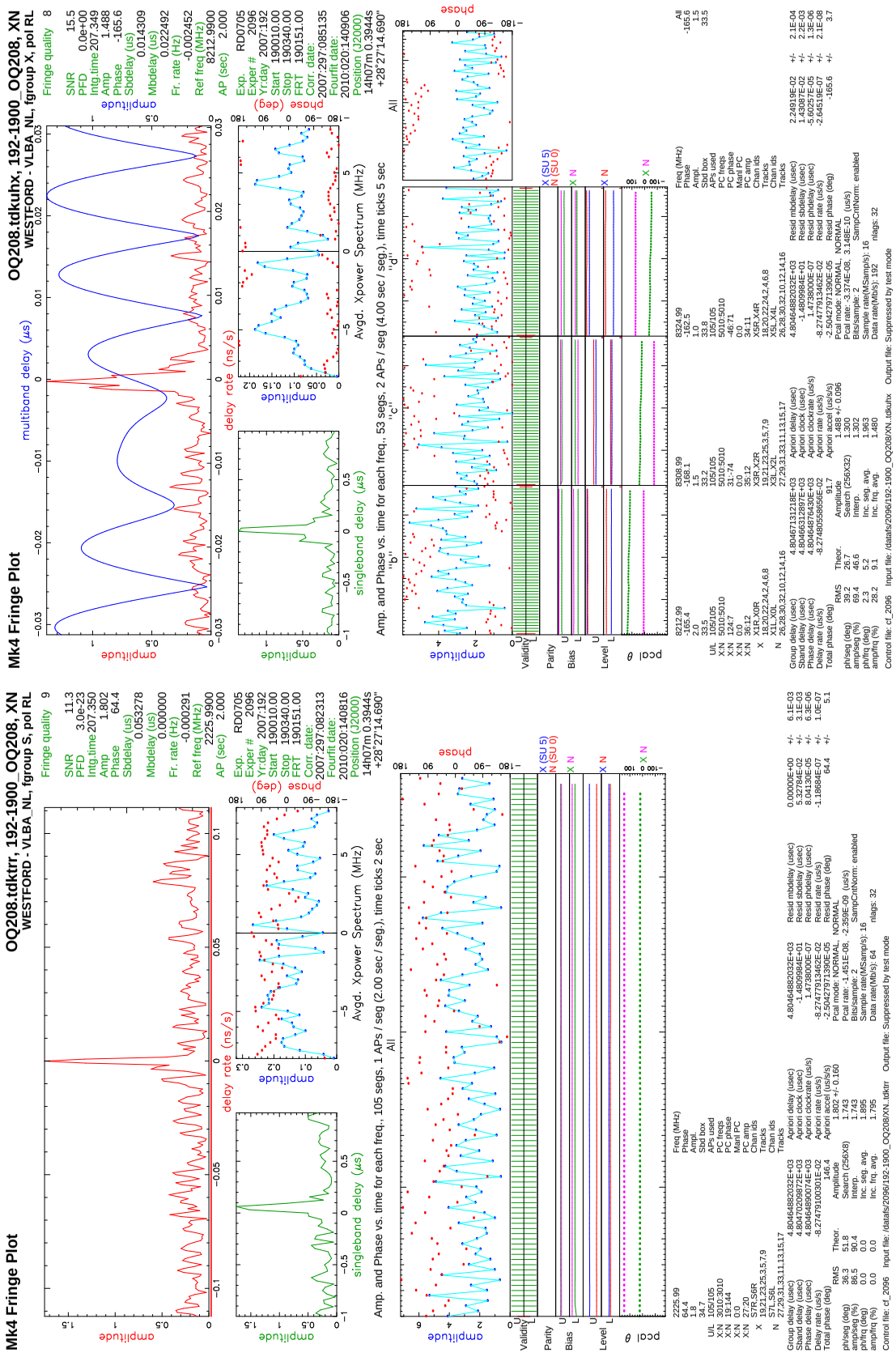

Figure A.2: HOPS fringe plots for the same scan on OQ 208 as in Figure A.1, but the correlation is between RCP at Westford and LCP at Noth Liberty. The presence of fringes is a symptom of polarization leakage, because OQ 208 is not polarized. The bottom plot is the S-band and the top plot is the X-band.

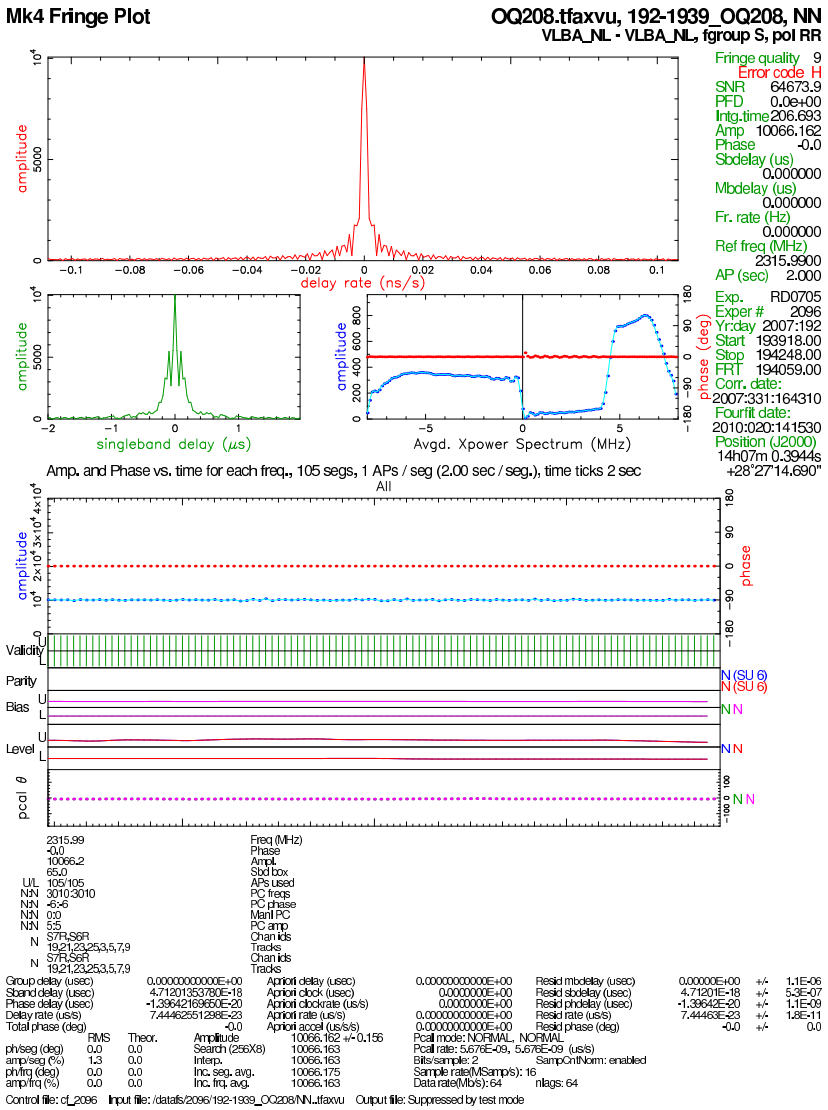

Figure A.3: HOPS fringe plot showing the autocorrelation for North Liberty, S-band. The amplitude of the power spectrum in the USB is completely dominated by the RFI. This scan is not usable for further analysis.

simultaneously versus SBD, MBD and DR. The plots described above, are slices through this 3D space. The residual errors are written at the bottom of the fourfit plots, but are removed from the data themselves before plotting i.e. the plotted data are the residual after the data are corrected using the delay and phase solution found by *fourfit* during fringe fitting. The other plots in the third row will not be described as they are out of the scope of this dissertation and are there for helping the correlator analysts to perform data quality analysis and carry out recorrelations where necessary.

Appendix B

Data Reduction To Measure Polarization Leakage - Programs

B.1 Python Script for Reduction of X-Band Data

This Python script was used to automate most of the data reduction, it reads a priori calibration from a file of system temperature measurements, called the ANTAB file, performs fringe fitting, imaging, deconvolution and self calibration. The python script had to be given the input and output filenames and frequencies for every setup.

```
# Python script taylored for rd0705 data reduction.
# Based on the EVN python scripts from Cormac Reynolds.
# Changed by A. Bertarini and A. Roy

# Standard preliminaries

# the 'import' serves two different purposes: it identifies an external
# file to be loaded, and it becomes a variable in the script,
# which references the module object after the file is loaded

# 'from' imports the module file as usual, but adds an extra step
# that copies one or more names out of the file.

from AIPS import AIPS, AIPSDisk
from AIPSTask import AIPSTask, AIPSList
from AIPSData import AIPSUVData, AIPSImage, AIPSCat
from AIPSTV import AIPSTV

# Alessandra's user ID
AIPS.userno = xxxx

# Ale decided to use AIPS stable version form dec 2007:
AIPSTask.version = 'OLD'

# This module provides instances to dispatch function calls locally
```

```
# without doing any Remote Programm Call.
import LocalProxy

#A ServerProxy instance has a method corresponding to each remote
# procedure call accepted by the XML-RPC server
from xmlrpclib import ServerProxy

import copy, optparse, os, sys
import re, string, pprint, math
import time

FuncLog = sys.stdout
my_tv = AIPSTV()
pid_list = []


# Main program is at the end. Python complains otherwise.
# Just discovered that also that the program wants first the AIPS task, then the
# functions that call the AIPS task and at the end the main....

# ***** Start with the definition of the AIPS tasks with their parameters*****

#task IMAGR:

def runimagr(uvdata, source, clbox1, clbox2, nboxes, imsize,
             cellsize, docalib, eif, niter, stokes, outdata,
             dotv, flagver, nchan = 64, doband = -1):

    """ must set indata, cellsize and source"""
    #assert (indata != None, cellsize != None and source != None), '''cellsize
    #        not set in runimagr'''

    if dotv > 0:
        my_tv.clear()

    imagr = AIPSTask('imagr')

    imagr.isbatch = 0
    imagr.indata = uvdata
    imagr.outname = outdata
    imagr.outdisk = 1
    imagr.outseq = 0
    imagr.sources[1] = source
    imagr.freqid = 1
#    imagr.selband = -1
#    imagr.selfreq = -1
#    imagr.subarray = 0
    imagr.docalib = docalib
    imagr.dopol = -1
```

```
    imagr.bif = 1
    imagr.eif = eif
    imagr.bchan = 3
    imagr.echan = 61
    imagr.clbox [1:]= [clbox1] + [clbox2]
    imagr.bpver = 1
    imagr.doband = doband
    imagr.nboxes = nboxes
    imagr.nchav = nchan
    imagr.chinc = nchan
    imagr.flagver = flagver
    imagr.stokes = stokes
    imagr.uvwtfn = 'UO'
    imagr.cellsize[1:] = [cellsize, cellsize]
    imagr.imsize[1:] = [imsize, imsize]
    imagr.robust = 0
    imagr.xtype = 5
    imagr.ytype = 5
    imagr.niter = niter
# If FLUX < 0 then Clean stops after the first negative Clean component
    imagr.flux = -1
    imagr.allokay = -1
    imagr.gain = 0.05
    imagr.minpatch = imsize // 2
    imagr.imagrprm[8:10] = [-0.1e-4, 1]
    imagr.dotv = dotv
    imagr.inp()
    imagr.go()

# task CALIB:

def runcalib(uvdata, solint, calsour, solmode, antuse, uvrange,
             docalib, refant, flagver, imgdata, doband=-1, bpver=1):

    calib = AIPSTask('calib')
    calib.indata = uvdata
    if is_aipsdata(imgdata):
        calib.in2data = imgdata
    calib.calsour[1] = calsour
    calib.smodel[1] = 0
    calib.freqid = 1
    calib.docalib = docalib
    calib.gainuse = 0
    calib.flagver = flagver
    calib.doband = doband
    calib.bpver = bpver
    calib.bchan = 3
    calib.echan = 61
```

```
#   use all the component that IMAGR found
    calib.ncomp[1] =0
    calib.solmode = solmode
    if (solmode == 'P'):
        calib.aparm[1] = 3
        calib.cparm[2] = 1
    else:
        calib.aparm[1] = 4
        calib.cparm[2] = 0
    calib.aparm[6] = 1

#   default to minimum allowed snr = 5
    calib.aparm[7] = 0
    calib.aparm[9] = 1
    calib.solint = solint
    calib.refant = refant
    calib.soltype = 'L1R'
    calib.cmethod = 'DFT'
    calib.minamper = 10
    calib.minphser = 20
    calib.cparm[1] = 30
# calib.cparm[2] defined in the IF above
    calib.cparm[3] = 10
    calib.cparm[4] = 20
    calib.antuse = antuse
    calib.uvrange = uvrange
    calib.snver = 0
    calib.inp()
    calib()

 # function to run clcal. Don't allow default snver.
def runclcal(uvdata, refant, calsour, source, snver):

    clcal = AIPSTask('clcal')
    clcal.indata = uvdata
    clcal.subarray = 1
    clcal.calsour = AIPSList([calsour])
    clcal.sources = AIPSList([source])
    clcal.opcode = 'CALI'
    clcal.interpol = 'SELF'
    clcal.samptype = ''
    clcal.doblank = 0
    clcal.dobtween = 0
    clcal.refant = refant

# snver is equal to one in the call to runclcal from apriori_cal
# but snver = to the last one in the  call to runclcal from
# selfcal_map
    clcal.snver = snver
```

```
    clcal.gainver = 0
    clcal.gainuse = 0
    clcal.inp()
    clcal()

def runantab(uvdata, antab_file):
    antab = AIPSTask('antab')
    antab.indata = uvdata
    antab.infile = antab_file
    antab.offset = 1
    antab.tyver = 0
    antab.gcver = 0
    antab.inp()
    antab()

def runapcal(uvdata, eif):
    apcal = AIPSTask('apcal')
    apcal.indata = uvdata
    apcal.antennas[1:] = [0]
    apcal.stokes = ''
    apcal.bif = 1
    apcal.eif =eif
    apcal.sources = AIPSList([''])
    apcal.timerang[1:] = [0]
    apcal.tyver = 0
    apcal.gcver = 0
    apcal.snver = 0
    apcal.opcode = ''
    apcal.inp()
    apcal()

def runclcor(uvdata, eif):
    clcor = AIPSTask('clcor')
    clcor.indata = uvdata
    clcor.sources = AIPSList([''])
    clcor.stokes = ''
    clcor.selband = -1
    clcor.selfreq = -1
    clcor.freqid = -1
    clcor.bif = 1
    clcor.eif = eif
    clcor.timerang[1:] = [0]
    clcor.gainver = 0
    clcor.gainus = 0
    clcor.opcode = 'PANG'
    clcor.clcorprm[1] = 1
    clcor.inp()
    clcor()
```

```
def runfring(uvdata, flagver, refant, docalib):
    fring = AIPSTask('fring')
    fring.indata = uvdata
    fring.gainus = 0
    fring.flagver =flagver
    fring.dparm[1] = 1
    fring.dparm[2] = 2000
    fring.dparm[3] = 300
    fring.dparm[4] = 2
#### dparm(7) =1 hen the phase, rate and delays will not be
#    re-referenced to a common antenna.  This option is only
#    desirable for VLBI polarization data.
    fring.dparm(7) =  1
    fring.aparm[1] = 2
    fring.aparm[6] = 3
    fring.aparm[7] = 10
    fring.docalib = docalib
    fring.timerang[1:] = [0]
    fring.bchan = 3
    fring.echan = 61
    fring.refant =refant
    fring.snver = 0
    fring.weightit = 0
    fring.solint = 1
    fring.inp()
    fring()

def runbpass(uvdata, flagver, docalib, eif, refant):
    bpass = AIPSTask('bpass')
    bpass.gainus = 0
    bpass.indata = uvdata
    bpass.ichansel [1] = AIPSList([5,59,1,0])
    bpass.bpassprm [1] = 0
    bpass.docalib = docalib
    bpass.eif = eif
    bpass.bif = 1
    bpass.solint = 5
    bpass.flagver = flagver
    bpass.refant = refant
    bpass.inp()
    bpass()

def runimean(imgdata, blc=0, trc=0):
    '''Must set indata'''

    #assert (indata != None)
    imean = AIPSTask('imean')
    imean.indata = imgdata
    imean.blc[1:] = blc
```

```
    imean.trc[1:] = trc
    imean()
    datamax = imgdata.header.datamax
    return (datamax, imean.pixstd)


# Stop with AIPS tasks.

##### Start with the fuction definition:
#     ---------------------------------


##### FUNCTION APRIORI_CAL ######
def apriori_cal(uvdata, antab_file, refant, eif, flagver, docalib):

#   calls to AIPS tasks required in apriori_cal:
    runantab(uvdata, antab_file)
    runapcal(uvdata,eif)

# first run of clcal, i.e. snver = 0 -> 1

    runclcal(uvdata, refant, calsour = '', source= '', snver = 0)
    runclcor(uvdata, eif)
    runfring(uvdata, flagver, refant, docalib)

#   second run of clcal after fring. Therefore
#   higher version of SN table to be passed into runclcal

    sntable1 = uvdata.table_highver('AIPS SN')

    runclcal(uvdata, refant, calsour= '', source= '', snver = sntable1)
#    runbpass(uvdata, flagver, docalib, eif, refant)


##### FUNCTION SELFCAL_MAP ######
def selfcal_map(uvdata, source, calsour, nsc, solint, refant, cellsize, imsize, eif, niter,
                flagver,prefix, imgseq, docalib, outdata, dotv):

#   defined after a run on OQ208 X-band directly in AIPS.
    nboxes = 2
    clbox1 = AIPSList([116.67, 112.67, 139.00, 149.00])
    clbox2 = AIPSList([158.67, 88.67, 180.33, 114.67])

#   iterate on selfcal and mapping steps.

#   create an empty image:

    imgdata = AIPSImage(uvdata.name, 'ICL001', uvdata.disk, imgseq)
```

```
#   call to subroutine create_image which calls runimagr and get_dyn_range.
#   Get_dyn_range calls runimean.
    create_image(uvdata, outdata, source, imgdata, niter, clbox1, clbox2,
                 nboxes, dotv, cellsize, imsize)

#   self calibration loop
    for i in range(nsc):

#      starting with phase self calibration. I.e. solmode = 'P'
       if (i <= 7):

#           solint = 0.2 for Kp phase instability
            solint = 0.2
            solmode = 'P'
            uvrange = AIPSList([0,0])
            antuse = AIPSList([0,0])

#       from nsc = 10 first round of amplitude & phase calibration. I.e. solmode ='A&P'
       if (i >= 8):
            solmode = 'A&P'
            solint = 4

#           A list of the antennas to be used in the calculation of
#           the mean gain modulus. Antenna used are the one with good
#           apriori calibration. Los Alamos (ante 3) is excluded due to
#           bad weather on site). The trusted antennas are VLBA, Eb and Wz.
            antuse = AIPSList([1, 2, 4, 5, 6, 7, 8, 9, 14, 19])

#           restriction of UVRANGE to less than 200000 klambda due to source (OQ208)
#           structure visible at longer baseline.
            uvrange = AIPSList([0,200000])

#       debugging prints statements:
#        print >>FuncLog, "selfcal iteration ", i+1, \
#                ' using solmode= ', solmode, ' and source model ', \
#                aipsuvname(imgdata)
#        print >>FuncLog, "solint=", solint

#       call to runcalib after the first (empty) map has been created
       runcalib(uvdata, solint, calsour, solmode, antuse, uvrange,
                docalib, refant, flagver, imgdata, doband=-1, bpver=1)

#       higher version of SN table to be passed into runclcal
       sntable = uvdata.table_highver('AIPS SN')

#       call to runclcal
       runclcal(uvdata, refant, calsour, source, snver=sntable)

#       next round of imaging
```

```
       imgseq += 1
       imgdata = AIPSImage(uvdata.name, 'ICL001', uvdata.disk, imgseq)
       print >>FuncLog, 'Creating image:', aipsuvname(imgdata)

#       call to create image again:
       create_image(uvdata, outdata, source, imgdata, niter, clbox1, clbox2,
                    nboxes, dotv, cellsize, imsize)


##### FUNCTION CREATE_IMAGE #####
def create_image(uvdata, outdata, source, imgdata, niter, clbox1, clbox2,
                 nboxes, dotv, cellsize, imsize):

#   created an empty beam:
    stokes = 'I'
    beamklass = stokes + 'BM001'
    beamdata = AIPSImage(imgdata.name, beamklass, imgdata.disk, imgdata.seq)

#   call to zap_old_data. It destroys the onl clean images and beams.
    zap_old_data(imgdata)
    zap_old_data(beamdata)

# debugger print statement:
#    print >>FuncLog, 'number pixels=', imsize
#    print >>FuncLog, 'pixel size=', cellsize*1.e3, 'mas'

#   call to runimagr (AIPS task imagr)
    runimagr(uvdata, source, clbox1, clbox2, nboxes, imsize,
             cellsize, docalib, eif, niter, stokes, outdata, dotv,
             flagver, nchan = 64, doband = -1)

#   call to subroutine get_dyn_range => runimean
    peakflux, rmsflux = get_dyn_range(imgdata)

    print >>FuncLog, 'peak flux=', peakflux
    print >>FuncLog, 'rms flux=', rmsflux
    print >>FuncLog, 'dynamic range=', peakflux/rmsflux

#   the value of peakflux and rms are returned to the main program
    return peakflux, rmsflux

##### FUNCTION ZAP_OLD_DATA #####  (delete AIPS data from catalogue)
def zap_old_data(aipsdata):
    if aipsdata.exists():
        print >>FuncLog, 'zapping old data: ' + aipsuvname(aipsdata)
        aipsdata.zap(force=True)
    else:
        print >>FuncLog, 'no old data to zap: ' + aipsuvname(aipsdata)
```

```
##### FUNCTION AIPSUVNAME #####
# shortcut to return the aips catalogue name of an AIPSUVData object
def aipsuvname(aipsdata):
    return aipsdata.name + '.' + aipsdata.klass + '.' + str(aipsdata.seq)

##### FUNCTION GET_DYN_RANGE #####
def get_dyn_range(imgdata):
    x = imgdata.header.naxis[0]
    y = imgdata.header.naxis[1]
    (peakflux, pixstd) = runimean(imgdata, [0, 0], [x // 4, y // 4])
    rmsflux =  pixstd
    if (rmsflux < 1.e-5):
        rmsflux = 1.e-5
    if (rmsflux > peakflux):
        rmsflux = peakflux/4.
    return peakflux, rmsflux

##### FUNCTION IS_AIPSDATA #####
# Check whether the passed object has the valid attributes for an AIPS data object
def is_aipsdata(aipsdata):
    got_attr = False
    if (hasattr(aipsdata, 'name') and hasattr(aipsdata, 'disk') and
            hasattr(aipsdata, 'seq') and hasattr(aipsdata, 'klass') ):
        got_attr = True
    return got_attr



#**************************** MAIN PROGRAM!*******************#

# prefix = 'S_1'
prefix = 'X_11'

suffix = 'UVSRT'
indisk = 1
inseq = 2
imgseq = 1

antab_file = '/aux/vlb052b/aips/sx_11/X_Band/rd0705.TSYS'

#******General use parameters*******#
solint = 1
refant = 7
source = 'OQ208'
calsour = 'OQ208'
docalib = 1
dotv = -1

#*** Flagging Table*****#
```

```
flagver = 3

#*** Mapping parameters****:#

#cellsize for S-band:
#cellsize = 0.0005

#cellsize for X-band:
cellsize = 0.00015

# image size:
imsize = 256

# S-band end IF:
# eif = 1

# X-band end IF:
eif = 3

# nr. of max iteration in cleaning
niter = 1000

#maps outname:
# outdata = 'OQ208_S1_I'
outdata = 'X_11'
#***************************#

# confirmed: first is read indisk then inseq!
uvdata = AIPSUVData(prefix, suffix, indisk , inseq)

# Debugging checks:
#uvdata.exists()
#print uvdata.exists()

# number of cycle - 1 since Python starts from zero to count!!!
nsc = 11

# call to apriori_cal, which perform the AIPS tasks:
# antab, apcal, clcal, clcor, fring, clcal
#  bpass

apriori_cal(uvdata, antab_file, refant, eif, flagver, docalib)

# call to selfcal_map, which perform the AIPS tasks:
# imagr, imean, calib, clcal

selfcal_map(uvdata, source, calsour, nsc, solint, refant, cellsize, imsize, eif, niter,
            flagver, prefix, imgseq, docalib, outdata, dotv)
```

B.2 DTSIM input file

The file below is the input file used for performing the data simulation in AIPS using DTSIM.

```
!!!! Setup X11 !!!!!!!!!!!!!!!

 AN_TABLE VER = 1 /
   STATION = 'VLBA_PT'
   MNT = 'AZEL'
   NO = 1
   CARTPOS= -1640953.7120,5014816.0240,3575411.8800 /

   STATION = 'VLBA_KP'
   MNT = 'AZEL'
   NO = 2
   CARTPOS= -1995678.6260,5037317.7130,3357328.1290 /

   STATION = 'VLBA_LA'
   MNT = 'AZEL'
   NO = 3
   CARTPOS= -1449752.3590,4975298.5880,3709123.9280 /

   STATION = 'VLBA_BR'
   MNT = 'AZEL'
   NO = 4
   CARTPOS= -2112064.9760,3705356.5160,4726813.7980 /

   STATION = 'VLBA_FD'
   MNT = 'AZEL'
   NO = 5
   CARTPOS= -1324009.1270,5332181.9660,3231962.4740/

   STATION = 'VLBA_SC'
   MNT = 'AZEL'
   NO = 6
   CARTPOS= 2607848.5210,5488069.6850,1932739.5400/

   STATION = 'VLBA_NL'
   MNT = 'AZEL'
   NO = 7
   CARTPOS= -130872.2540,4762317.1160,4226851.0400/

   STATION = 'VLBA_OV'
   MNT = 'AZEL'
   NO = 8
   CARTPOS= -2409150.1120,4478573.2290,3838617.3990/

   STATION = 'VLBA_MK'
   MNT = 'AZEL'
```

```
 NO = 9
 CARTPOS= -5464074.9600,2495249.1160,2148296.8440/

STATION = 'VLBA_HN'
MNT = 'AZEL'
NO = 10
CARTPOS= 1446375.1160,4447939.6560,4322306.1240/

STATION = 'MEDICINA'
MNT = 'AZEL'
NO = 11
CARTPOS= 4461369.9880,-919596.8300,4449559.1730/

 STATION = 'NOTO'
 MNT = 'AZEL'
 NO = 12
 CARTPOS= 4934563.1290,-1321201.2670,3806484.4710/

 STATION = 'ONSALA60'
 MNT = 'AZEL'
 NO = 13
 CARTPOS= 3370606.0450,-711917.4940,5349830.7260/

 STATION = 'WETTZELL'
 MNT = 'AZEL'
 NO = 14
 CARTPOS= 4075539.8990,-931735.2700,4801629.3520/

STATION = 'KOKEE'
MNT = 'AZEL'
NO = 15
CARTPOS= -5543837.6170,2054567.8480,2387851.9390/

STATION = 'FORTLEZA'
MNT = 'AZEL'
NO = 16
CARTPOS= 4985370.0490,3955020.3280,-428472.2810/

 STATION = 'MATERA'
 MNT = 'AZEL'
 NO = 17
 CARTPOS= 4641938.7830,-1393003.0260,4133325.5230/

 STATION = 'WESTFORD'
 MNT = 'AZEL'
 NO = 18
 CARTPOS= 1492206.6000,4458130.5070,4296015.5320/

 STATION = 'EB_VLBA'
```

```
   MNT = 'AZEL'
   NO = 19
   CARTPOS= 4033947.5000,-486990.5200,4900430.8210/

   END /

!!!!!!!!!!!!!!!!!!!

 FQ_TABLE /

   FQID = 1
   FREQ = 8564.99,8820.99,8836.99
   TOTBW = 16,16,16
   CHANBW = 0.25,0.25,0.25
   SIDE = 1,1,1 /

   END /

!!!!!!!!!!!!!!!!!!!!!

 SU_TABLE /

   SU_ID = 1
   NAME = 'OQ208'
   RAEPO = 14:07:00.394414
   DECEPO = 28:27:14.69023
   EPOCH = 2000 /

   END /

!!!!!!!!!!!!!!!!!!!!!

 CAT_HDR /

   REF_FREQ = 8564.99
   NO_IF = 3
   NO_CHAN = 64
   STOKES = 'RR', 'LL', 'RL', 'LR'
   REF_DATE = '11/07/07'

   /

!!!!!!!!!!!!!!!!!!!!!!!

 CAL_ERR LINPOL /

   STATION = 'VLBA_PT'
   FQID = 1
   FEED_1R = 1, 0.0422, 48.75
```

```
FEED_1L = 1, 0.0354, 114.40
FEED_2R = 1,0.0507,47.37
FEED_2L = 1, 0.0472,105.91
FEED_3R = 1, 0.0445,44.17
FEED_3L = 1, 0.0427,95.11
GAIN_1R = 1, 8.70
GAIN_1L = 1, 8.93
GAIN_2R = 1, 8.70
GAIN_2L = 1,8.93
GAIN_3R = 1, 8.70
GAIN_3L = 1,8.93
TSYS_1R  = 1, 0, 2, 34.0, 0
TSYS_1L = 1,0, 2, 34.0, 0
TSYS_2R  = 1, 0, 2, 34.0, 0
TSYS_2L = 1,0, 2, 34.0, 0
TSYS_3R  = 1, 0, 2, 34.0, 0
TSYS_3L = 1,0, 2, 34.0, 0/

STATION = 'VLBA_KP'
FQID = 1
FEED_1R = 1,0.0671,40.06
FEED_1L = 1,0.0600, 121.66
FEED_2R = 1,0.0661,51.52
FEED_2L = 1,0.0546,116.49
FEED_3R = 1,0.0683,55.23
FEED_3L = 1,0.0593,115.75
GAIN_1R = 1, 10.53
GAIN_1L = 1, 9.17
GAIN_2R = 1, 10.53
GAIN_2L = 1, 9.17
GAIN_3R = 1, 10.53
GAIN_3L = 1, 9.17
TSYS_1R  = 1, 0, 2, 42.0, 0
TSYS_1L = 1,0, 2, 42.0, 0
TSYS_2R  = 1, 0, 2, 42.0, 0
TSYS_2L = 1,0, 2, 42.0, 0
TSYS_3R  = 1, 0, 2, 42.0, 0
TSYS_3L = 1,0, 2, 42.0, 0 /

STATION = 'VLBA_LA'
FQID = 1
FEED_1R = 1,0.0459,31.57
FEED_1L = 1,0.0452,133.83
FEED_2R = 1,0.0481,34.46
FEED_2L = 1,0.0565,112.71
FEED_3R = 1,0.0491,35.62
FEED_3L = 1,0.0478,106.90
GAIN_1R = 1, 9.71
GAIN_1L = 1, 9.26
```

```
 GAIN_2R = 1, 9.71
 GAIN_2L = 1, 9.26
 GAIN_3R = 1, 9.71
 GAIN_3L = 1, 9.26
 TSYS_1R  = 1, 0, 2, 43.0, 0
 TSYS_1L = 1,0, 2, 43.0, 0
 TSYS_2R  = 1, 0, 2, 43.0, 0
 TSYS_2L = 1,0, 2, 43.0, 0
 TSYS_3R  = 1, 0, 2, 43.0, 0
 TSYS_3L = 1,0, 2, 43.0, 0 /

 STATION = 'VLBA_BR'
 FQID = 1
 FEED_1R = 1,0.0477,64.15
 FEED_1L = 1,0.0788, 115.12
 FEED_2R = 1,0.0435,61.68
 FEED_2L = 1,0.0728,105.77
 FEED_3R = 1,0.0472,64.17
 FEED_3L = 1,0.0715,95.70
 GAIN_1R = 1, 8.93
 GAIN_1L = 1, 9.26
 GAIN_2R = 1, 8.93
 GAIN_2L = 1, 9.26
 GAIN_3R = 1, 8.93
 GAIN_3L = 1, 9.26
 TSYS_1R  = 1, 0, 2, 38.0, 0
 TSYS_1L = 1,0, 2, 38.0, 0
 TSYS_2R  = 1, 0, 2, 38.0, 0
 TSYS_2L = 1,0, 2, 38.0, 0
 TSYS_3R  = 1, 0, 2, 38.0, 0
 TSYS_3L = 1,0, 2, 38.0, 0 /

 STATION = 'VLBA_FD'
 FQID = 1
 FEED_1R = 1,0.0455,40.00
 FEED_1L = 1,0.0471,113.33
 FEED_2R = 1,0.0494,34.77
 FEED_2L = 1,0.0459,115.04
 FEED_3R = 1,0.0459,44.18
 FEED_3L = 1,0.0454,109.70
 GAIN_1R = 1, 9.62
 GAIN_1L = 1, 10.0
 GAIN_2R = 1, 9.62
 GAIN_2L = 1, 10.0
 GAIN_3R = 1, 9.62
 GAIN_3L = 1, 10.0
TSYS_1R  = 1, 0, 2, 46.0, 0
TSYS_1L = 1,0, 2, 46.0, 0
TSYS_2R  = 1, 0, 2, 46.0, 0
```

```
TSYS_2L = 1,0, 2, 46.0, 0
TSYS_3R  = 1, 0, 2, 46.0, 0
TSYS_3L = 1,0, 2, 46.0, 0 /

 STATION = 'VLBA_SC'
 FQID = 1
 FEED_1R = 1,0.0335,37.30
 FEED_1L = 1,0.0329,127.36
 FEED_2R = 1,0.0226,33.42
 FEED_2L = 1,0.0257,90.94
 FEED_3R = 1,0.0326,32.50
 FEED_3L = 1,0.0150,103.53
 GAIN_1R = 1, 9.35
 GAIN_1L = 1, 9.01
 GAIN_2R = 1, 9.35
 GAIN_2L = 1, 9.01
 GAIN_3R = 1, 9.35
 GAIN_3L = 1, 9.01
 TSYS_1R  = 1, 0, 2, 55.0, 0
 TSYS_1L = 1,0, 2, 55.0, 0
 TSYS_2R  = 1, 0, 2, 55.0, 0
 TSYS_2L = 1,0, 2, 55.0, 0
 TSYS_3R  = 1, 0, 2, 55.0, 0
 TSYS_3L = 1,0, 2, 55.0, 0 /

 STATION = 'VLBA_NL'
 FQID = 1
 FEED_1R = 1,0.0522,54.29
 FEED_1L = 1,0.0604,125.80
 FEED_2R = 1,0.0475,54.86
 FEED_2L = 1,0.0573,113.64
 FEED_3R = 1,0.0499,60.56
 FEED_3L = 1,0.0569,111.82
 GAIN_1R = 1, 9.09
 GAIN_1L = 1, 8.93
 GAIN_2R = 1, 9.09
 GAIN_2L = 1, 8.93
 GAIN_3R = 1, 9.09
 GAIN_3L = 1, 8.93
TSYS_1R  = 1, 0, 2, 38.0, 0
TSYS_1L = 1,0, 2, 38.0, 0
TSYS_2R  = 1, 0, 2, 38.0, 0
TSYS_2L = 1,0, 2, 38.0, 0
TSYS_3R  = 1, 0, 2, 38.0, 0
TSYS_3L = 1,0, 2, 38.0, 0/

 STATION = 'VLBA_OV'
 FQID = 1
 FEED_1R = 1,0.0558,34.75
```

```
   FEED_1L = 1,0.0513,122.32
   FEED_2R = 1,0.0652,42.51
   FEED_2L = 1,0.0685,115.64
   FEED_3R = 1,0.0662,44.04
   FEED_3L = 1,0.0570,109.49
   GAIN_1R = 1, 9.62
   GAIN_1L = 1, 9.43
   GAIN_2R = 1, 9.62
   GAIN_2L = 1, 9.43
   GAIN_3R = 1, 9.62
   GAIN_3L = 1, 9.43
   TSYS_1R  = 1, 0, 2, 48.0, 0
   TSYS_1L = 1,0, 2, 48.0, 0
   TSYS_2R  = 1, 0, 2, 48.0, 0
   TSYS_2L = 1,0, 2, 48.0, 0
   TSYS_3R  = 1, 0, 2, 48.0, 0
   TSYS_3L = 1,0, 2, 48.0, 0 /

   STATION = 'VLBA_MK'
   FQID = 1
   FEED_1R = 1,0.0456,32.70
   FEED_1L = 1,0.0456,124.29
   FEED_2R = 1,0.0456,50.68
   FEED_2L = 1,0.0434,117.42
   FEED_3R = 1,0.0473,45.98
   FEED_3L = 1,0.0490,109.88
   GAIN_1R = 1, 9.26
   GAIN_1L = 1, 9.71
   GAIN_2R = 1, 9.26
   GAIN_2L = 1, 9.71
   GAIN_3R = 1, 9.26
   GAIN_3L = 1, 9.71
   TSYS_1R  = 1, 0, 2, 46.0, 0
   TSYS_1L = 1,0, 2, 46.0, 0
   TSYS_2R  = 1, 0, 2, 46.0, 0
   TSYS_2L = 1,0, 2, 46.0, 0
   TSYS_3R  = 1, 0, 2, 46.0, 0
   TSYS_3L = 1,0, 2, 46.0, 0 /

!   STATION = 'VLBA_HN'
!   FQID = 1
!   FEED_1R = 1,0.0000 , 0.00
!   FEED_1L = 1,0.0000,0.00
!   FEED_2R = 1,0.0000 , 0.00
!  FEED_2L = 1,0.0000,0.00
!  FEED_3R = 1,0.0000 , 0.00
!  FEED_3L = 1,0.0000,0.00
!  GAIN_1R = 1, 1
!  GAIN_1L = 1, 1
```

```
!  GAIN_2R = 1, 1
!  GAIN_2L = 1, 1
!  GAIN_3R = 1, 1
!  GAIN_3L = 1, 1
!  TSYS_1R  = 1, 0, 2, 1.0, 0
!  TSYS_1L = 1,0, 2, 1.0, 0
!  TSYS_2R  = 1, 0, 2, 1.0, 0
!  TSYS_2L = 1,0, 2, 1.0, 0
!  TSYS_3R  = 1, 0, 2, 1.0, 0
!  TSYS_3L = 1,0, 2, 1.0, 0 /

!  STATION = 'MEDICINA'
!  FQID = 1
!  FEED_1R = 1,0.0000,0.00
!  FEED_2R = 1,0.0000,0.00
!  FEED_3R = 1,0.0000,0.00
!  GAIN_1R = 1, 1
!  GAIN_2R = 1, 1
!  GAIN_3R = 1, 1
!  TSYS_1R  = 1, 0, 2, 1.0, 0
!  TSYS_2R  = 1, 0, 2, 1.0, 0
!  TSYS_3R  = 1, 0, 2, 1.0, 0/

   STATION = 'NOTO'
   FQID = 1
   FEED_1R = 1,0.0583,141.08
   FEED_2R = 1,0.0000,0.00
   FEED_3R = 1,0.0000,0.00
   GAIN_1R = 1, 6.49
   GAIN_2R = 1, 6.49
   GAIN_3R = 1, 6.49
   TSYS_1R  = 1, 0, 2, 102.0, 0
   TSYS_2R  = 1, 0, 2, 102.0, 0
   TSYS_3R  = 1, 0, 2, 102.0, 0 /

   STATION = 'ONSALA60'
   FQID = 1
   FEED_1R = 1,0.0303,34.22
   FEED_2R = 1,0.0000,0.00
   FEED_3R = 1,0.0336,63.25
   GAIN_1R = 1, 18.18
   GAIN_2R = 1, 18.18
   GAIN_3R = 1, 18.18
   TSYS_1R  = 1, 0, 2, 56.0, 0
   TSYS_2R  = 1, 0, 2, 56.0, 0
   TSYS_3R  = 1, 0, 2, 56.0, 0 /

   STATION = 'WETTZELL'
   FQID = 1
```

```
   FEED_1R = 1,0.0208,-70.91
   FEED_2R = 1,0.0306,-47.61
   FEED_3R = 1,0.0256,-31.15
   GAIN_1R = 1, 16.67
   GAIN_2R = 1, 16.67
   GAIN_3R = 1, 16.67
   TSYS_1R  = 1, 0, 2, 27.0, 0
   TSYS_2R  = 1, 0, 2, 27.0, 0
   TSYS_3R  = 1, 0, 2, 27.0, 0 /

!  STATION = 'KOKEE'
!  FQID = 1
!  FEED_1R = 1,0.0000,0.00
!  FEED_2R = 1,0.0000,0.00
!  FEED_3R = 1,0.0000,0.00
!  GAIN_1R = 1, 1
!  GAIN_2R = 1, 1
!  GAIN_3R = 1, 1
!  TSYS_1R  = 1, 0, 2, 1.0, 0
!  TSYS_2R  = 1, 0, 2, 1.0, 0
!  TSYS_3R  = 1, 0, 2, 1.0, 0 /

!  STATION = 'FORTLEZA'
!  FQID = 1
!  FEED_1R = 1,0.0000,0.00
!  FEED_2R = 1,0.0000,0.00
!  FEED_3R = 1,0.0000,0.00
!  GAIN_1R = 1, 1
!  GAIN_2R = 1, 1
!  GAIN_3R = 1, 1
!  TSYS_1R  = 1, 0, 2, 1.0, 0
!  TSYS_2R  = 1, 0, 2, 1.0, 0
!  TSYS_3R  = 1, 0, 2, 1.0, 0 /

   STATION = 'MATERA'
   FQID = 1
   FEED_1R = 1,0.0861,-174.66
   FEED_2R = 1,0.0207,111.14
   FEED_3R = 1,0.0206,133.26
   GAIN_1R = 1, 25.0
   GAIN_2R = 1, 25.0
   GAIN_3R = 1, 25.0
   TSYS_1R  = 1, 0, 2, 41.0, 0
   TSYS_2R  = 1, 0, 2, 41.0, 0
   TSYS_3R  = 1, 0, 2, 41.0, 0 /

   STATION = 'WESTFORD'
   FQID = 1
   FEED_1R = 1,0.1448,-139.12
```

```
   FEED_2R = 1,0.1510,93.38
   FEED_3R = 1,0.1329,86.66
   GAIN_1R = 1, 25.0
   GAIN_2R = 1, 25.0
   GAIN_3R = 1, 25.0
   TSYS_1R  = 1, 0, 2, 46.0, 0
   TSYS_2R  = 1, 0, 2, 46.0, 0
   TSYS_3R  = 1, 0, 2, 46.0, 0 /

   STATION = 'EB_VLBA'
   FQID = 1
   FEED_1R = 1,0.0069,39.88
   FEED_2R = 1,0.0330,63.58
   FEED_3R = 1,0.0383,53.94
   GAIN_1R = 1, 0.73
   GAIN_2R = 1, 0.73
   GAIN_3R = 1, 0.73
   TSYS_1R  = 1, 0, 2, 23.0, 0
   TSYS_2R  = 1, 0, 2, 23.0, 0
   TSYS_3R  = 1, 0, 2, 23.0, 0 /

  END /

!!!!!!!!!!!!!!!!!!!!!!!!!!!!

 SU_MODEL /

   SOURCE = 'OQ208'
!! old model maybe too large in size!!!!
!   TYPE=  2, 0, 0, 2.8, 0.0012, 0.0009, 1.6,0,0,0 /
!!!
!! new model at 24.06.2009
     TYPE=  2, 0, 0, 2.8, 0.00096,0.00072, 1.6,0,0,0 /

   SOURCE = 'OQ208'
   TYPE = 1, -0.005499, -0.003993, 0.16,0,0,0 /

 END /

!!!!!!!!!!!!!!!!!!

 SCHEDULE /

   DAY = 11 MONTH = 07 YEAR = 2007
   START = 19:43:31
   STOP =  19:47:09
   SOURCE = 'OQ208'
   FQID = 1
   TINT = 2 /
```

```
  DAY = 11 MONTH = 07 YEAR = 2007
  START = 21:20:35
  STOP =  21:24:13
  SOURCE = 'OQ208'
  FQID = 1
  TINT = 2 /

  DAY = 11 MONTH = 07 YEAR = 2007
  START = 23:45:29
  STOP =  23:49:07
  SOURCE = 'OQ208'
  FQID = 1
  TINT = 2 /

  DAY = 12 MONTH = 07 YEAR = 2007
  START = 01:22:33
  STOP =  01:26:11
  SOURCE = 'OQ208'
  FQID = 1
  TINT = 2 /

  DAY = 12 MONTH = 07 YEAR = 2007
  START = 02:42:13
  STOP =  02:45:51
  SOURCE = 'OQ208'
  FQID = 1
  TINT = 2

  DAY = 12 MONTH = 07 YEAR = 2007
  START = 04:01:53
  STOP =  04:05:31
  SOURCE = 'OQ208'
  FQID = 1
  TINT = 2

  END /
```

B.3 C-program to Calculate the Rice Distribution

```
/*
 * A. Bertarini
 *
 * rice.c : to find the error on dterm phases and amplitude
 * following the rice distribution (pag 192 - Thomson-Moran-Swenson)
 *
 *
 * to compile with math lib: gcc -lm -lc rice.c
```

```
 */

#include <stdio.h>
#include <math.h>
#include <string.h>
#include <stdlib.h>
#define DEBUG 1         /* 1 = print debug messages.  0 = silent */
#define step 0.0001      /*step to calculate the rice distribution */
#define sigma 0.012     /* sigma from RE/Im */
/* #define amp 0.1637       max dterm amplitude -- 0.0009 min dterm ampl -- 0.0395 median */
/*#define amp 0.1637 */
#define INFIL "tderm.idl"
#define OUTFIL "amp_phase_error_bars.txt"
#define MAXLEN 1000

double bessi0 (double x);
double erff0 (double x);

main(int argc) {

  FILE *fp1, *fp2;        /* file pointers for I/O files */
  int i,k;
  double j;
  double sq, bessi_arg, exponential, area;
  double Z, phase;
  double P_Z, P_phase;
  double I_zero;      /* modified bessel function */
  double erf_zero, erf_arg, first_part, second_part, third_part;
  char line[MAXLEN];
  double freq, amp, pha;
  int pol, ante_no;
  double phase_error, amp_error;
  double phase_1, phase_99, Z_1, Z_99;

  sq = pow (sigma,2);
  area = 0;


/* read input file*/

  fp1 = fopen(INFIL, "r");
  if (fp1 == NULL) {
    printf("Trouble opening %s\n", INFIL);
    exit(1);
  }

/* Open output file containing phase errors */

    fp2 = fopen(OUTFIL, "w");
```

```
    if (fp2 == NULL) {
      printf("Trouble opening %s\n", OUTFIL);
      exit(1);
    }
/* read and process every line from input file */

    k = 0;
    fgets(line, MAXLEN, fp1);

    while (!feof(fp1)) {
      sscanf(line, "%lf %d %d %*lf %*lf %lf %lf", &freq, &ante_no, &pol, &amp, &pha);

/* printf ("%s\n", line); read correctly */

/* printf("%lf %d %d %lf %lf\n", freq, ante_no, pol, amp, pha); read correctly */

      if(amp != 0.0000) {
/*printf ("%lf\n",amp); */

/* for loop for calculating the d-term amp. probablility distribution */

       for (Z = 0.; Z < 0.3; Z+= step) {
          bessi_arg = (Z * fabs(amp) / sq);
          I_zero = bessi0(bessi_arg);
          exponential = exp(-1. * (Z*Z + amp * amp)/ (2. * sq));
          P_Z = (Z / sq) * exponential  * I_zero;
/*          printf("%lf %le\n", Z, P_Z); */
        }

/* for loop to calculate the d-term phase probablility distribution*/

       for (phase = -1. * M_PI; phase < M_PI; phase += step) {
         erf_arg = (fabs(amp) * cos(phase)) / ((sqrt(2.)) * sigma);
         erf_zero = erff0 (erf_arg);
         first_part =  1. / ( 2. * M_PI) * exp (-1. * (amp * amp) / (2. * (sigma * sigma))) ;
         second_part = 1. + sqrt(M_PI / 2.) * (fabs(amp) * cos (phase)) / sigma ;
         third_part = exp((amp  * amp * pow(cos(phase),2.)) / (2. * sigma * sigma));
         P_phase = first_part * second_part * third_part * (1. + erf_zero);
       }


/*  calculation of the 2 % of the total area under the two asimmetric tails */
/* first percentile */
      area = 0;
       for (Z = 0.; area <= 0.01; Z += step) {
           bessi_arg = (Z * fabs(amp) / sq);
           I_zero = bessi0(bessi_arg);
           exponential = exp(-1. * (Z*Z + amp * amp)/ (2. * sq));
           P_Z = (Z / sq) * exponential  * I_zero;
```

```
           area += P_Z * step;
        }
       Z_1 = Z;
 /*     printf("first amp percentile  = %lf\n",Z); */

/* 99th percentile */
       area = 0;
         for (Z = 0.3; area <= 0.01; Z -= step) {
            bessi_arg = (Z * fabs(amp) / sq);
            I_zero = bessi0(bessi_arg);
            exponential = exp(-1. * (Z*Z + amp * amp)/ (2. * sq));
            P_Z = (Z / sq) * exponential  * I_zero;
            area += P_Z * step;
         }
         Z_99 = Z;
/*  printf("99th amp percentile  = %lf\n",Z); */

         area = 0.;
         for (phase = -1. * M_PI; area <= 0.01; phase += step) {
            erf_arg = (fabs(amp) * cos(phase)) / ((sqrt(2.)) * sigma);
            erf_zero = erff0 (erf_arg);
            first_part =  1. / ( 2. * M_PI) * exp (-1. * (amp * amp) / (2. * (sigma * sigma))) ;
            second_part = 1. + sqrt(M_PI / 2.) * (fabs(amp) * cos (phase)) / sigma ;
            third_part = exp((amp  * amp * pow(cos(phase),2.)) / (2. * sigma * sigma));
            P_phase = first_part * second_part * third_part * (1. + erf_zero);
            area += P_phase * step;
         }
         phase_1 = phase;
/*         printf("1st phase percentile = %lf\n", (180. / M_PI) * 1_phase);  */


         area = 0.;
         for (phase = M_PI; area <= 0.01; phase -= step) {
           erf_arg = (fabs(amp) * cos(phase)) / ((sqrt(2.)) * sigma);
           erf_zero = erff0 (erf_arg);
           first_part =  1. / ( 2. * M_PI) * exp (-1. * (amp * amp) / (2. * (sigma * sigma))) ;
           second_part = 1. + sqrt(M_PI / 2.) * (fabs(amp) * cos (phase)) / sigma ;
           third_part = exp((amp  * amp * pow(cos(phase),2.)) / (2. * sigma * sigma));
           P_phase = first_part * second_part * third_part * (1. + erf_zero);
           area += P_phase * step;
           }
           phase_99 = phase;
/*printf("%lf\n", phase_99); */
          phase_error = (phase_99 - phase_1) / 2.;
/* printf("%lf %lf %lf\n", phase_1, phase_99, phase_error);*/

           amp_error = (Z_99 - Z_1)/2.;

           fprintf(fp2, "%7.2lf %d %d %7.4lf %7.4lf %7.4lf %7.2lf %7.2lf\n",
```

```
                freq, ante_no, pol, amp, Z_1, Z_99, pha, (180. / M_PI) * phase_error);
      } /* close if amp != 0.*/
           k++;
           fgets(line, MAXLEN, fp1);
    } /* while end*/
    fclose(fp1);
    fclose(fp2);
} /*main end */

double bessi0(double x) {
/*Returns the modifiedd Bessel function I0(x) for any real x. */
/* from Numerical Recepies in C */

  double ax, I_zero;
  double y; /* Accumulate polynomials in double precision */

  if ((ax = fabs(x)) < 3.75) {
     y = x / 3.75;
     y= y * y;
     I_zero = 1.0 + y*(3.5156229 + y*(3.0899424 + y*(1.2067492 +
               y*(0.2659732 + y*(0.360768e-1 + y*0.45813e-2)))));
  }
  else {
     y = 3.75 / ax;
     I_zero = (exp(ax) / sqrt(ax)) * (0.39894228 + y*(0.1328592e-1 +
             y*(0.225319e-2 + y*(-0.157565e-2 + y*(0.916281e-2 + y*(-0.2057706e-1 +
             y*(0.2635537e-1 + y*(-0.1647633e-1 + y*0.392377e-2)))))));
  }

return I_zero;
}

double erff0(double x) {

/* Returns the error function erf(x)
   algorithm from http://mathworld.wolfram.com/Erf.html */

   double erf_zero;
   int n;
   double n_fact;

   erf_zero = 0.;
   n_fact = 1;

   if (x <= 6. && x >= -6.) {

     for (n = 0; n < 100; n++) {

        if (n == 0){
```

```
          n_fact = 1;
        }
        else {
          n_fact *= n;
        }

        erf_zero += (pow(-1.,n) * pow(x,2.*n+1.)) / (n_fact * (2. *n + 1.));
     }

     erf_zero *= 2. / sqrt (M_PI);

   }

   else if (x > 6.) {

     erf_zero = 1.;

   }
   else if  (x < -6.) {

     erf_zero = -1.;

   }


/*    printf("%lf %lf\n", x, erf_zero); */

   return erf_zero;

}
```

Appendix C

Polarization Leakage Tables

Table C.1: Amplitudes (dimensionless) and phases (in degrees) of D-term for antenna Pie Town versus frequency

Freq (MHz)	Amp. RCP	Phase RCP	Amp. LCP	Phase LCP
8228.99	$0.022^{+0.018}_{-0.030}$	51 ± 73	$0.023^{+0.019}_{-0.030}$	118 ± 71
8244.99	$0.026^{+0.020}_{-0.030}$	52 ± 67	$0.025^{+0.020}_{-0.030}$	111 ± 68
8276.99	$0.033^{+0.023}_{-0.029}$	51 ± 58	$0.022^{+0.018}_{-0.030}$	120 ± 73
8356.99	$0.036^{+0.024}_{-0.029}$	16 ± 52	$0.029^{+0.022}_{-0.029}$	152 ± 63
8372.99	$0.036^{+0.024}_{-0.029}$	28 ± 52	$0.031^{+0.023}_{-0.029}$	129 ± 60
8404.99	$0.040^{+0.025}_{-0.029}$	49 ± 46	$0.033^{+0.024}_{-0.029}$	111 ± 56
8420.99	$0.037^{+0.025}_{-0.029}$	49 ± 50	$0.033^{+0.023}_{-0.029}$	106 ± 58
8436.99	$0.036^{+0.024}_{-0.029}$	55 ± 52	$0.029^{+0.022}_{-0.030}$	90 ± 63
8500.99	$0.040^{+0.025}_{-0.029}$	44 ± 47	$0.038^{+0.025}_{-0.029}$	107 ± 50
8516.99	$0.039^{+0.025}_{-0.029}$	46 ± 47	$0.038^{+0.024}_{-0.029}$	108 ± 50
8532.99	$0.049^{+0.026}_{-0.029}$	53 ± 37	$0.043^{+0.025}_{-0.029}$	96 ± 42
8564.99	$0.042^{+0.025}_{-0.029}$	49 ± 43	$0.035^{+0.024}_{-0.029}$	114 ± 53
8692.99	$0.050^{+0.026}_{-0.029}$	58 ± 35	$0.046^{+0.025}_{-0.029}$	109 ± 39
8708.99	$0.054^{+0.026}_{-0.029}$	55 ± 32	$0.050^{+0.026}_{-0.029}$	108 ± 35
8724.99	$0.048^{+0.026}_{-0.029}$	44 ± 37	$0.050^{+0.026}_{-0.029}$	111 ± 35
8740.99	$0.051^{+0.026}_{-0.029}$	55 ± 34	$0.048^{+0.026}_{-0.029}$	96 ± 37
8772.99	$0.050^{+0.026}_{-0.029}$	47 ± 36	$0.043^{+0.025}_{-0.029}$	106 ± 42
8788.99	$0.052^{+0.026}_{-0.029}$	45 ± 34	$0.043^{+0.025}_{-0.029}$	101 ± 43
8804.99	$0.046^{+0.025}_{-0.029}$	50 ± 39	$0.042^{+0.025}_{-0.029}$	102 ± 44
8820.99	$0.051^{+0.026}_{-0.029}$	47 ± 35	$0.047^{+0.026}_{-0.029}$	106 ± 38
8836.99	$0.044^{+0.025}_{-0.029}$	44 ± 41	$0.043^{+0.025}_{-0.029}$	95 ± 43

Table C.2: Amplitudes (dimensionless) and phases (in degree) of D-term for antenna Kitt Peak versus frequency

Freq (MHz)	Amp. RCP	Phase RCP	Amp. LCP	Phase LCP
8212.99	$0.046^{+0.026}_{-0.029}$	28 ± 39	$0.041^{+0.025}_{-0.029}$	137 ± 46
8228.99	$0.043^{+0.025}_{-0.029}$	29 ± 42	$0.044^{+0.025}_{-0.029}$	147 ± 42
8244.99	$0.045^{+0.025}_{-0.029}$	32 ± 40	$0.046^{+0.025}_{-0.029}$	141 ± 39
8276.99	$0.046^{+0.025}_{-0.029}$	33 ± 39	$0.045^{+0.025}_{-0.029}$	139 ± 40
8308.99	$0.050^{+0.026}_{-0.029}$	32 ± 35	$0.048^{+0.026}_{-0.029}$	134 ± 37
8324.99	$0.052^{+0.026}_{-0.029}$	32 ± 33	$0.047^{+0.025}_{-0.029}$	131 ± 38
8356.99	$0.051^{+0.026}_{-0.029}$	3 ± 35	$0.048^{+0.026}_{-0.029}$	161 ± 37
8372.99	$0.054^{+0.026}_{-0.029}$	22 ± 32	$0.047^{+0.026}_{-0.029}$	140 ± 38
8404.99	$0.054^{+0.026}_{-0.029}$	39 ± 32	$0.050^{+0.026}_{-0.029}$	123 ± 35
8420.99	$0.050^{+0.026}_{-0.029}$	46 ± 35	$0.051^{+0.026}_{-0.029}$	119 ± 35
8436.99	$0.051^{+0.026}_{-0.029}$	53 ± 34	$0.048^{+0.026}_{-0.029}$	115 ± 37
8500.99	$0.058^{+0.026}_{-0.029}$	47 ± 30	$0.050^{+0.026}_{-0.029}$	123 ± 35
8516.99	$0.062^{+0.026}_{-0.029}$	41 ± 28	$0.054^{+0.026}_{-0.029}$	130 ± 32
8532.99	$0.066^{+0.026}_{-0.029}$	57 ± 26	$0.056^{+0.026}_{-0.029}$	112 ± 31
8564.99	$0.067^{+0.026}_{-0.029}$	40 ± 25	$0.060^{+0.026}_{-0.029}$	122 ± 29
8692.99	$0.065^{+0.026}_{-0.029}$	42 ± 26	$0.046^{+0.025}_{-0.029}$	102 ± 40
8708.99	$0.065^{+0.026}_{-0.029}$	44 ± 26	$0.048^{+0.026}_{-0.029}$	112 ± 38
8724.99	$0.059^{+0.026}_{-0.029}$	38 ± 29	$0.047^{+0.026}_{-0.029}$	119 ± 38
8740.99	$0.062^{+0.026}_{-0.029}$	53 ± 27	$0.051^{+0.026}_{-0.029}$	113 ± 34
8772.99	$0.068^{+0.026}_{-0.029}$	48 ± 25	$0.061^{+0.026}_{-0.029}$	112 ± 28
8788.99	$0.069^{+0.026}_{-0.029}$	51 ± 24	$0.054^{+0.026}_{-0.029}$	105 ± 32
8804.99	$0.066^{+0.026}_{-0.029}$	52 ± 26	$0.051^{+0.026}_{-0.029}$	109 ± 34
8820.99	$0.066^{+0.026}_{-0.029}$	52 ± 26	$0.055^{+0.026}_{-0.029}$	116 ± 32
8836.99	$0.068^{+0.027}_{-0.029}$	55 ± 25	$0.059^{+0.026}_{-0.029}$	116 ± 29

Table C.3: Amplitudes (dimensionless) and phases (in degrees) of D-term for antenna Los Alamos versus frequency

Freq (MHz)	Amp. RCP	Phase RCP	Amp. LCP	Phase LCP
8212.99	$0.039^{+0.025}_{-0.029}$	11 ± 48	$0.030^{+0.023}_{-0.029}$	134 ± 61
8228.99	$0.031^{+0.023}_{-0.030}$	15 ± 59	$0.028^{+0.021}_{-0.030}$	145 ± 65
8244.99	$0.035^{+0.024}_{-0.029}$	20 ± 54	$0.030^{+0.022}_{-0.029}$	144 ± 61
8276.99	$0.035^{+0.024}_{-0.029}$	18 ± 53	$0.034^{+0.024}_{-0.029}$	143 ± 56
8308.99	$0.045^{+0.025}_{-0.029}$	17 ± 41	$0.038^{+0.025}_{-0.029}$	137 ± 49
8324.99	$0.043^{+0.025}_{-0.029}$	13 ± 43	$0.037^{+0.025}_{-0.029}$	133 ± 50
8356.99	$0.038^{+0.025}_{-0.029}$	-17 ± 50	$0.037^{+0.024}_{-0.029}$	166 ± 51
8372.99	$0.042^{+0.025}_{-0.029}$	13 ± 44	$0.040^{+0.025}_{-0.029}$	137 ± 46
8404.99	$0.042^{+0.025}_{-0.029}$	22 ± 44	$0.037^{+0.024}_{-0.029}$	121 ± 51
8420.99	$0.043^{+0.025}_{-0.029}$	30 ± 43	$0.034^{+0.024}_{-0.029}$	118 ± 55
8436.99	$0.035^{+0.024}_{-0.029}$	35 ± 54	$0.035^{+0.024}_{-0.029}$	120 ± 53
8500.99	$0.047^{+0.026}_{-0.029}$	16 ± 38	$0.036^{+0.024}_{-0.029}$	103 ± 53
8516.99	$0.041^{+0.025}_{-0.029}$	29 ± 46	$0.033^{+0.024}_{-0.029}$	127 ± 57
8532.99	$0.056^{+0.026}_{-0.029}$	43 ± 31	$0.046^{+0.026}_{-0.029}$	104 ± 39
8564.99	$0.046^{+0.026}_{-0.029}$	32 ± 39	$0.045^{+0.025}_{-0.029}$	134 ± 40
8692.99	$0.047^{+0.025}_{-0.029}$	23 ± 38	$0.060^{+0.026}_{-0.029}$	108 ± 29
8708.99	$0.050^{+0.026}_{-0.029}$	24 ± 36	$0.058^{+0.026}_{-0.029}$	106 ± 30
8724.99	$0.043^{+0.025}_{-0.029}$	28 ± 42	$0.052^{+0.026}_{-0.029}$	112 ± 33
8740.99	$0.049^{+0.026}_{-0.029}$	44 ± 36	$0.049^{+0.026}_{-0.029}$	103 ± 36
8772.99	$0.059^{+0.026}_{-0.029}$	29 ± 29	$0.044^{+0.025}_{-0.029}$	118 ± 41
8788.99	$0.055^{+0.026}_{-0.029}$	32 ± 32	$0.050^{+0.026}_{-0.029}$	111 ± 36
8804.99	$0.048^{+0.026}_{-0.029}$	28 ± 37	$0.050^{+0.026}_{-0.029}$	106 ± 35
8820.99	$0.048^{+0.026}_{-0.029}$	34 ± 37	$0.057^{+0.026}_{-0.029}$	113 ± 31
8836.99	$0.049^{+0.026}_{-0.029}$	36 ± 36	$0.048^{+0.026}_{-0.029}$	107 ± 37

Table C.4: Amplitudes (dimensionless) and phases (in degrees) of D-term for antenna Brewster versus frequency

Freq (MHz)	Amp. RCP	Phase RCP	Amp. LCP	Phase LCP
8212.99	$0.023^{+0.018}_{-0.030}$	56 ± 72	$0.058^{+0.026}_{-0.029}$	131 ± 30
8228.99	$0.028^{+0.021}_{-0.030}$	67 ± 65	$0.057^{+0.026}_{-0.029}$	129 ± 30
8244.99	$0.034^{+0.024}_{-0.029}$	68 ± 56	$0.052^{+0.026}_{-0.029}$	124 ± 34
8276.99	$0.036^{+0.024}_{-0.029}$	50 ± 53	$0.050^{+0.026}_{-0.029}$	130 ± 35
8324.99	$0.032^{+0.023}_{-0.029}$	49 ± 59	$0.052^{+0.026}_{-0.029}$	124 ± 34
8356.99	$0.030^{+0.022}_{-0.029}$	24 ± 61	$0.046^{+0.026}_{-0.029}$	149 ± 39
8372.99	$0.033^{+0.024}_{-0.029}$	45 ± 57	$0.051^{+0.026}_{-0.029}$	128 ± 34
8404.99	$0.032^{+0.023}_{-0.029}$	55 ± 58	$0.041^{+0.025}_{-0.029}$	131 ± 46
8420.99	$0.041^{+0.025}_{-0.029}$	59 ± 45	$0.053^{+0.026}_{-0.029}$	132 ± 33
8436.99	$0.035^{+0.024}_{-0.029}$	67 ± 55	$0.064^{+0.026}_{-0.029}$	122 ± 27
8500.99	$0.041^{+0.025}_{-0.029}$	51 ± 45	$0.070^{+0.026}_{-0.029}$	124 ± 24
8516.99	$0.039^{+0.025}_{-0.029}$	54 ± 48	$0.069^{+0.027}_{-0.029}$	125 ± 24
8532.99	$0.060^{+0.026}_{-0.029}$	68 ± 29	$0.060^{+0.026}_{-0.029}$	100 ± 29
8564.99	$0.048^{+0.026}_{-0.029}$	64 ± 37	$0.079^{+0.027}_{-0.029}$	115 ± 21
8692.99	$0.056^{+0.026}_{-0.029}$	63 ± 31	$0.064^{+0.026}_{-0.029}$	103 ± 26
8708.99	$0.055^{+0.026}_{-0.029}$	63 ± 31	$0.062^{+0.026}_{-0.029}$	108 ± 27
8724.99	$0.054^{+0.026}_{-0.029}$	57 ± 32	$0.064^{+0.026}_{-0.029}$	111 ± 26
8740.99	$0.053^{+0.026}_{-0.029}$	66 ± 33	$0.059^{+0.026}_{-0.029}$	101 ± 29
8772.99	$0.054^{+0.026}_{-0.029}$	61 ± 32	$0.063^{+0.026}_{-0.029}$	112 ± 27
8788.99	$0.056^{+0.026}_{-0.029}$	65 ± 31	$0.068^{+0.027}_{-0.029}$	103 ± 25
8804.99	$0.055^{+0.026}_{-0.029}$	65 ± 32	$0.072^{+0.027}_{-0.029}$	98 ± 23
8820.99	$0.043^{+0.025}_{-0.029}$	62 ± 42	$0.073^{+0.027}_{-0.029}$	106 ± 23
8836.99	$0.047^{+0.026}_{-0.029}$	64 ± 38	$0.071^{+0.026}_{-0.029}$	96 ± 24

Table C.5: Amplitudes (dimensionless) and phases (in degrees) of D-term for antenna Fort Davis versus frequency

Freq (MHz)	Amp. RCP	Phase RCP	Amp. LCP	Phase LCP
8212.99	$0.024^{+0.019}_{-0.030}$	16 ± 70	$0.027^{+0.021}_{-0.030}$	132 ± 65
8228.99	$0.023^{+0.019}_{-0.030}$	23 ± 72	$0.032^{+0.023}_{-0.029}$	140 ± 59
8244.99	$0.023^{+0.018}_{-0.030}$	32 ± 72	$0.038^{+0.025}_{-0.029}$	135 ± 49
8276.99	$0.031^{+0.023}_{-0.029}$	40 ± 60	$0.034^{+0.024}_{-0.029}$	118 ± 55
8308.99	$0.034^{+0.024}_{-0.029}$	30 ± 55	$0.029^{+0.022}_{-0.030}$	118 ± 62
8324.99	$0.037^{+0.024}_{-0.029}$	29 ± 51	$0.027^{+0.021}_{-0.030}$	133 ± 66
8356.99	$0.033^{+0.024}_{-0.029}$	0 ± 57	$0.036^{+0.024}_{-0.029}$	158 ± 53
8372.99	$0.034^{+0.024}_{-0.029}$	21 ± 56	$0.034^{+0.024}_{-0.029}$	140 ± 55
8404.99	$0.037^{+0.024}_{-0.029}$	39 ± 51	$0.034^{+0.024}_{-0.029}$	128 ± 56
8420.99	$0.033^{+0.023}_{-0.029}$	42 ± 58	$0.041^{+0.025}_{-0.029}$	115 ± 46
8436.99	$0.035^{+0.024}_{-0.029}$	58 ± 53	$0.041^{+0.025}_{-0.029}$	111 ± 45
8500.99	$0.047^{+0.026}_{-0.029}$	35 ± 38	$0.037^{+0.024}_{-0.029}$	107 ± 51
8516.99	$0.039^{+0.025}_{-0.029}$	36 ± 48	$0.041^{+0.025}_{-0.029}$	115 ± 45
8532.99	$0.050^{+0.026}_{-0.029}$	50 ± 36	$0.039^{+0.025}_{-0.029}$	110 ± 48
8564.99	$0.045^{+0.025}_{-0.029}$	40 ± 40	$0.047^{+0.026}_{-0.029}$	113 ± 38
8692.99	$0.045^{+0.025}_{-0.029}$	42 ± 40	$0.033^{+0.023}_{-0.029}$	99 ± 57
8708.99	$0.050^{+0.026}_{-0.029}$	43 ± 35	$0.036^{+0.024}_{-0.029}$	105 ± 52
8724.99	$0.042^{+0.025}_{-0.029}$	35 ± 43	$0.034^{+0.024}_{-0.029}$	119 ± 56
8740.99	$0.041^{+0.025}_{-0.029}$	45 ± 45	$0.037^{+0.024}_{-0.029}$	113 ± 50
8772.99	$0.044^{+0.025}_{-0.029}$	37 ± 41	$0.044^{+0.025}_{-0.029}$	115 ± 42
8788.99	$0.045^{+0.025}_{-0.029}$	41 ± 40	$0.043^{+0.025}_{-0.029}$	112 ± 42
8804.99	$0.049^{+0.026}_{-0.029}$	45 ± 36	$0.044^{+0.025}_{-0.029}$	107 ± 42
8820.99	$0.049^{+0.026}_{-0.029}$	35 ± 36	$0.046^{+0.026}_{-0.029}$	115 ± 39
8836.99	$0.046^{+0.026}_{-0.029}$	44 ± 39	$0.045^{+0.025}_{-0.029}$	110 ± 40

Table C.6: Amplitudes (dimensionless) and phases (in degrees) of D-term for antenna Saint Croix versus frequency

Freq (MHz)	Amp. RCP	Phase RCP	Amp. LCP	Phase LCP
8212.99	$0.017^{+0.014}_{-0.030}$	16 ± 83	$0.016^{+0.013}_{-0.031}$	139 ± 87
8228.99	$0.014^{+0.011}_{-0.031}$	23 ± 94	$0.021^{+0.017}_{-0.030}$	135 ± 74
8244.99	$0.023^{+0.019}_{-0.030}$	20 ± 71	$0.018^{+0.015}_{-0.030}$	131 ± 81
8276.99	$0.022^{+0.018}_{-0.030}$	0 ± 73	$0.010^{+0.008}_{-0.031}$	152 ± 121
8308.99	$0.016^{+0.013}_{-0.030}$	-2 ± 86	$0.022^{+0.018}_{-0.030}$	135 ± 73
8324.99	$0.016^{+0.013}_{-0.030}$	-1 ± 86	$0.021^{+0.017}_{-0.030}$	130 ± 74
8356.99	$0.020^{+0.017}_{-0.030}$	-13 ± 76	$0.021^{+0.017}_{-0.030}$	154 ± 74
8372.99	$0.021^{+0.017}_{-0.030}$	-0 ± 74	$0.018^{+0.015}_{-0.030}$	152 ± 81
8404.99	$0.020^{+0.017}_{-0.030}$	41 ± 76	$0.027^{+0.021}_{-0.030}$	134 ± 66
8420.99	$0.017^{+0.014}_{-0.030}$	40 ± 83	$0.030^{+0.023}_{-0.030}$	123 ± 61
8436.99	$0.019^{+0.016}_{-0.030}$	40 ± 78	$0.026^{+0.021}_{-0.030}$	107 ± 67
8500.99	$0.025^{+0.020}_{-0.030}$	43 ± 69	$0.027^{+0.021}_{-0.030}$	125 ± 65
8516.99	$0.027^{+0.021}_{-0.030}$	37 ± 66	$0.027^{+0.021}_{-0.030}$	122 ± 66
8532.99	$0.027^{+0.021}_{-0.030}$	33 ± 66	$0.038^{+0.025}_{-0.029}$	97 ± 49
8564.99	$0.034^{+0.024}_{-0.029}$	37 ± 56	$0.033^{+0.024}_{-0.029}$	127 ± 57
8692.99	$0.032^{+0.023}_{-0.029}$	23 ± 58	$0.034^{+0.024}_{-0.029}$	103 ± 55
8708.99	$0.031^{+0.023}_{-0.030}$	35 ± 61	$0.035^{+0.024}_{-0.029}$	100 ± 54
8724.99	$0.023^{+0.019}_{-0.030}$	25 ± 72	$0.032^{+0.023}_{-0.029}$	113 ± 58
8740.99	$0.027^{+0.021}_{-0.030}$	45 ± 65	$0.039^{+0.025}_{-0.029}$	102 ± 47
8772.99	$0.029^{+0.022}_{-0.030}$	40 ± 63	$0.029^{+0.022}_{-0.030}$	96 ± 63
8788.99	$0.026^{+0.021}_{-0.030}$	44 ± 66	$0.027^{+0.021}_{-0.030}$	98 ± 65
8804.99	$0.034^{+0.024}_{-0.029}$	46 ± 56	$0.020^{+0.017}_{-0.030}$	91 ± 76
8820.99	$0.023^{+0.018}_{-0.030}$	33 ± 72	$0.026^{+0.020}_{-0.030}$	91 ± 68
8836.99	$0.033^{+0.023}_{-0.029}$	32 ± 58	$0.015^{+0.012}_{-0.030}$	104 ± 89

Table C.7: Amplitudes (dimensionless) and phases (in degrees) of D-term for antenna North Liberty versus frequency

Freq (MHz)	Amp. RCP	Phase RCP	Amp. LCP	Phase LCP
8212.99	$0.034^{+0.024}_{-0.029}$	40 ± 56	$0.042^{+0.025}_{-0.029}$	135 ± 44
8228.99	$0.027^{+0.021}_{-0.030}$	56 ± 65	$0.044^{+0.025}_{-0.029}$	131 ± 42
8244.99	$0.042^{+0.025}_{-0.029}$	64 ± 43	$0.045^{+0.025}_{-0.029}$	125 ± 40
8276.99	$0.054^{+0.026}_{-0.029}$	54 ± 32	$0.043^{+0.025}_{-0.029}$	119 ± 42
8308.99	$0.052^{+0.026}_{-0.029}$	31 ± 34	$0.040^{+0.025}_{-0.029}$	129 ± 46
8324.99	$0.046^{+0.025}_{-0.029}$	29 ± 39	$0.042^{+0.025}_{-0.029}$	126 ± 44
8356.99	$0.040^{+0.025}_{-0.029}$	15 ± 47	$0.041^{+0.025}_{-0.029}$	154 ± 45
8372.99	$0.043^{+0.025}_{-0.029}$	38 ± 42	$0.039^{+0.025}_{-0.029}$	135 ± 48
8404.99	$0.050^{+0.026}_{-0.029}$	42 ± 35	$0.042^{+0.025}_{-0.029}$	123 ± 44
8420.99	$0.046^{+0.025}_{-0.029}$	49 ± 39	$0.044^{+0.025}_{-0.029}$	115 ± 41
8436.99	$0.042^{+0.025}_{-0.029}$	56 ± 43	$0.048^{+0.026}_{-0.029}$	109 ± 37
8500.99	$0.051^{+0.026}_{-0.029}$	46 ± 35	$0.054^{+0.026}_{-0.029}$	120 ± 33
8516.99	$0.047^{+0.026}_{-0.029}$	44 ± 38	$0.053^{+0.026}_{-0.029}$	122 ± 33
8532.99	$0.046^{+0.025}_{-0.029}$	53 ± 39	$0.053^{+0.026}_{-0.029}$	111 ± 33
8564.99	$0.052^{+0.026}_{-0.029}$	54 ± 34	$0.060^{+0.026}_{-0.029}$	126 ± 28
8692.99	$0.059^{+0.026}_{-0.029}$	47 ± 29	$0.053^{+0.026}_{-0.029}$	108 ± 33
8708.99	$0.054^{+0.026}_{-0.029}$	46 ± 32	$0.049^{+0.026}_{-0.029}$	109 ± 36
8724.99	$0.047^{+0.026}_{-0.029}$	40 ± 38	$0.047^{+0.025}_{-0.029}$	120 ± 38
8740.99	$0.051^{+0.026}_{-0.029}$	52 ± 35	$0.054^{+0.026}_{-0.029}$	108 ± 32
8772.99	$0.044^{+0.025}_{-0.029}$	52 ± 41	$0.054^{+0.026}_{-0.029}$	116 ± 32
8788.99	$0.046^{+0.025}_{-0.029}$	61 ± 39	$0.054^{+0.026}_{-0.029}$	112 ± 32
8804.99	$0.048^{+0.026}_{-0.029}$	64 ± 37	$0.058^{+0.026}_{-0.029}$	112 ± 30
8820.99	$0.048^{+0.026}_{-0.029}$	55 ± 38	$0.057^{+0.026}_{-0.029}$	114 ± 30
8836.99	$0.050^{+0.026}_{-0.029}$	61 ± 35	$0.057^{+0.026}_{-0.029}$	112 ± 30

Table C.8: Amplitudes (dimensionless) and phases (in degrees) of D-term for antenna Owens Valley versus frequency

Freq (MHz)	Amp. RCP	Phase RCP	Amp. LCP	Phase LCP
8212.99	$0.044^{+0.025}_{-0.029}$	21 ± 41	$0.048^{+0.026}_{-0.029}$	135 ± 37
8228.99	$0.043^{+0.025}_{-0.029}$	17 ± 42	$0.044^{+0.025}_{-0.029}$	136 ± 41
8244.99	$0.046^{+0.025}_{-0.029}$	17 ± 39	$0.044^{+0.025}_{-0.029}$	138 ± 42
8276.99	$0.040^{+0.025}_{-0.029}$	18 ± 47	$0.039^{+0.025}_{-0.029}$	143 ± 48
8308.99	$0.040^{+0.025}_{-0.029}$	30 ± 46	$0.054^{+0.026}_{-0.029}$	141 ± 32
8324.99	$0.045^{+0.025}_{-0.029}$	22 ± 40	$0.051^{+0.026}_{-0.029}$	143 ± 35
8356.99	$0.041^{+0.025}_{-0.029}$	-9 ± 46	$0.047^{+0.026}_{-0.029}$	172 ± 38
8372.99	$0.055^{+0.026}_{-0.029}$	16 ± 32	$0.036^{+0.024}_{-0.029}$	134 ± 52
8404.99	$0.046^{+0.025}_{-0.029}$	32 ± 39	$0.051^{+0.026}_{-0.029}$	131 ± 34
8420.99	$0.050^{+0.026}_{-0.029}$	45 ± 35	$0.052^{+0.026}_{-0.029}$	122 ± 33
8436.99	$0.050^{+0.026}_{-0.029}$	46 ± 36	$0.046^{+0.025}_{-0.029}$	114 ± 39
8500.99	$0.054^{+0.026}_{-0.029}$	29 ± 32	$0.054^{+0.026}_{-0.029}$	125 ± 32
8516.99	$0.052^{+0.026}_{-0.029}$	32 ± 34	$0.058^{+0.026}_{-0.029}$	126 ± 30
8532.99	$0.061^{+0.026}_{-0.029}$	43 ± 28	$0.061^{+0.026}_{-0.029}$	113 ± 28
8564.99	$0.056^{+0.026}_{-0.029}$	35 ± 31	$0.051^{+0.026}_{-0.029}$	122 ± 34
8692.99	$0.057^{+0.026}_{-0.029}$	37 ± 30	$0.072^{+0.026}_{-0.029}$	120 ± 23
8708.99	$0.061^{+0.026}_{-0.029}$	40 ± 28	$0.059^{+0.026}_{-0.029}$	116 ± 29
8724.99	$0.058^{+0.026}_{-0.029}$	33 ± 30	$0.059^{+0.026}_{-0.029}$	120 ± 29
8740.99	$0.063^{+0.026}_{-0.029}$	48 ± 27	$0.061^{+0.026}_{-0.029}$	113 ± 28
8772.99	$0.059^{+0.026}_{-0.029}$	39 ± 29	$0.061^{+0.026}_{-0.029}$	122 ± 28
8788.99	$0.059^{+0.026}_{-0.029}$	45 ± 29	$0.066^{+0.026}_{-0.029}$	114 ± 26
8804.99	$0.063^{+0.026}_{-0.029}$	48 ± 27	$0.062^{+0.026}_{-0.029}$	111 ± 28
8820.99	$0.065^{+0.026}_{-0.029}$	43 ± 26	$0.069^{+0.027}_{-0.029}$	116 ± 25
8836.99	$0.066^{+0.026}_{-0.029}$	44 ± 26	$0.057^{+0.026}_{-0.029}$	109 ± 30

Table C.9: Amplitudes (dimensionless) and phases (in degrees) of D-term for antenna Mauna Kea versus frequency

Freq (MHz)	Amp. RCP	Phase RCP	Amp. LCP	Phase LCP
8212.99	$0.033^{+0.023}_{-0.029}$	27 ± 58	$0.032^{+0.023}_{-0.029}$	136 ± 59
8228.99	$0.031^{+0.023}_{-0.030}$	28 ± 59	$0.031^{+0.023}_{-0.029}$	144 ± 60
8244.99	$0.035^{+0.024}_{-0.029}$	26 ± 55	$0.036^{+0.024}_{-0.029}$	144 ± 53
8276.99	$0.032^{+0.023}_{-0.029}$	25 ± 58	$0.042^{+0.025}_{-0.029}$	140 ± 44
8308.99	$0.038^{+0.025}_{-0.029}$	24 ± 49	$0.043^{+0.025}_{-0.029}$	122 ± 42
8324.99	$0.036^{+0.024}_{-0.029}$	27 ± 52	$0.043^{+0.025}_{-0.029}$	116 ± 42
8356.99	$0.036^{+0.024}_{-0.029}$	-2 ± 52	$0.036^{+0.024}_{-0.029}$	152 ± 52
8372.99	$0.038^{+0.025}_{-0.029}$	21 ± 49	$0.037^{+0.024}_{-0.029}$	146 ± 51
8404.99	$0.043^{+0.025}_{-0.029}$	39 ± 42	$0.038^{+0.025}_{-0.029}$	123 ± 49
8420.99	$0.039^{+0.025}_{-0.029}$	46 ± 48	$0.040^{+0.025}_{-0.029}$	118 ± 46
8436.99	$0.039^{+0.025}_{-0.029}$	51 ± 48	$0.049^{+0.026}_{-0.029}$	110 ± 36
8500.99	$0.047^{+0.025}_{-0.029}$	33 ± 38	$0.041^{+0.025}_{-0.029}$	122 ± 45
8516.99	$0.042^{+0.025}_{-0.029}$	34 ± 43	$0.043^{+0.025}_{-0.029}$	124 ± 43
8532.99	$0.044^{+0.025}_{-0.029}$	39 ± 41	$0.047^{+0.026}_{-0.029}$	100 ± 38
8564.99	$0.046^{+0.025}_{-0.029}$	33 ± 40	$0.046^{+0.025}_{-0.029}$	124 ± 40
8692.99	$0.044^{+0.025}_{-0.029}$	39 ± 41	$0.052^{+0.026}_{-0.029}$	107 ± 33
8708.99	$0.049^{+0.026}_{-0.029}$	38 ± 36	$0.057^{+0.026}_{-0.029}$	111 ± 30
8724.99	$0.041^{+0.025}_{-0.029}$	26 ± 45	$0.057^{+0.026}_{-0.029}$	113 ± 30
8740.99	$0.039^{+0.025}_{-0.029}$	42 ± 48	$0.052^{+0.026}_{-0.029}$	104 ± 34
8772.99	$0.042^{+0.025}_{-0.029}$	41 ± 44	$0.050^{+0.026}_{-0.029}$	108 ± 35
8788.99	$0.041^{+0.025}_{-0.029}$	47 ± 45	$0.041^{+0.025}_{-0.029}$	98 ± 45
8804.99	$0.051^{+0.026}_{-0.029}$	48 ± 35	$0.043^{+0.025}_{-0.029}$	104 ± 42
8820.99	$0.046^{+0.025}_{-0.029}$	51 ± 40	$0.043^{+0.025}_{-0.029}$	117 ± 42
8836.99	$0.047^{+0.026}_{-0.029}$	46 ± 38	$0.049^{+0.026}_{-0.029}$	110 ± 36

Table C.10: Amplitudes (dimensionless) and phases (in degrees) of D-term for antenna Noto versus frequency. Noto has fewer frequencies that the other stations since its receiver can observe only up to about 8600 MHz.

Freq (MHz)	Amp. RCP	Phase RCP
8212.99	$0.026^{+0.021}_{-0.030}$	113 ± 67
8228.99	$0.035^{+0.024}_{-0.029}$	110 ± 53
8244.99	$0.033^{+0.024}_{-0.029}$	109 ± 56
8276.99	$0.030^{+0.023}_{-0.029}$	100 ± 61
8308.99	$0.054^{+0.026}_{-0.029}$	63 ± 32
8324.99	$0.031^{+0.023}_{-0.029}$	115 ± 60
8356.99	$0.026^{+0.021}_{-0.030}$	67 ± 67
8372.99	$0.040^{+0.025}_{-0.029}$	94 ± 46
8404.99	$0.035^{+0.024}_{-0.029}$	78 ± 53
8420.99	$0.032^{+0.023}_{-0.029}$	80 ± 58
8436.99	$0.028^{+0.022}_{-0.030}$	127 ± 64
8500.99	$0.021^{+0.017}_{-0.030}$	132 ± 75
8516.99	$0.026^{+0.021}_{-0.030}$	126 ± 66
8564.99	$0.058^{+0.026}_{-0.029}$	141 ± 30

Table C.11: Amplitudes (dimensionless) and phases (in degrees) of D-term for antenna Onsala versus frequency

Freq (MHz)	Amp. RCP	Phase RCP
8212.99	$0.071^{+0.026}_{-0.029}$	18 ± 24
8228.99	$0.051^{+0.026}_{-0.029}$	-14 ± 34
8244.99	$0.060^{+0.026}_{-0.029}$	-5 ± 28
8276.99	$0.035^{+0.024}_{-0.029}$	-12 ± 54
8308.99	$0.016^{+0.014}_{-0.030}$	35 ± 84
8324.99	$0.039^{+0.025}_{-0.029}$	48 ± 48
8356.99	$0.021^{+0.018}_{-0.030}$	11 ± 74
8372.99	$0.042^{+0.025}_{-0.029}$	35 ± 44
8404.99	$0.061^{+0.026}_{-0.029}$	19 ± 28
8420.99	$0.067^{+0.026}_{-0.029}$	23 ± 25
8436.99	$0.059^{+0.026}_{-0.029}$	7 ± 29
8500.99	$0.030^{+0.023}_{-0.030}$	-22 ± 61
8516.99	$0.021^{+0.017}_{-0.030}$	-3 ± 75
8532.99	$0.006^{+0.004}_{-0.032}$	-11 ± 166
8564.99	$0.030^{+0.023}_{-0.029}$	34 ± 61
8692.99	$0.056^{+0.026}_{-0.029}$	-25 ± 31
8708.99	$0.052^{+0.026}_{-0.029}$	-14 ± 34
8724.99	$0.053^{+0.026}_{-0.029}$	-37 ± 33
8740.99	$0.037^{+0.025}_{-0.029}$	-46 ± 50
8772.99	$0.007^{+0.005}_{-0.032}$	41 ± 156
8788.99	$0.018^{+0.015}_{-0.030}$	55 ± 79
8804.99	$0.011^{+0.009}_{-0.031}$	71 ± 113
8836.99	$0.034^{+0.024}_{-0.029}$	63 ± 56

Table C.12: Amplitudes (dimensionless) and phases (in degrees) of D-term for antenna Wettzell versus frequency

Freq (MHz)	Amp. RCP	Phase RCP
8212.99	$0.011^{+0.008}_{-0.031}$	-180 ± 114
8228.99	$0.004^{+0.002}_{-0.033}$	-127 ± 171
8244.99	$0.013^{+0.011}_{-0.031}$	-151 ± 96
8276.99	$0.013^{+0.011}_{-0.031}$	-144 ± 96
8308.99	$0.004^{+0.002}_{-0.033}$	172 ± 171
8324.99	$0.006^{+0.004}_{-0.032}$	83 ± 165
8356.99	$0.018^{+0.015}_{-0.030}$	-88 ± 79
8372.99	$0.015^{+0.013}_{-0.030}$	-72 ± 88
8404.99	$0.014^{+0.012}_{-0.031}$	-87 ± 92
8420.99	$0.017^{+0.014}_{-0.030}$	-57 ± 82
8436.99	$0.022^{+0.018}_{-0.030}$	-64 ± 72
8500.99	$0.021^{+0.018}_{-0.030}$	-86 ± 74
8516.99	$0.028^{+0.021}_{-0.030}$	-82 ± 65
8532.99	$0.027^{+0.021}_{-0.030}$	-28 ± 66
8564.99	$0.021^{+0.017}_{-0.030}$	-71 ± 75
8692.99	$0.028^{+0.021}_{-0.030}$	-54 ± 65
8708.99	$0.024^{+0.020}_{-0.030}$	-62 ± 69
8724.99	$0.021^{+0.017}_{-0.030}$	-90 ± 74
8740.99	$0.030^{+0.022}_{-0.029}$	-59 ± 61
8772.99	$0.022^{+0.018}_{-0.030}$	-61 ± 72
8788.99	$0.030^{+0.022}_{-0.029}$	-45 ± 62
8804.99	$0.022^{+0.018}_{-0.030}$	-50 ± 73
8820.99	$0.031^{+0.023}_{-0.030}$	-48 ± 61
8836.99	$0.026^{+0.020}_{-0.030}$	-31 ± 68

Table C.13: Amplitudes (dimensionless) and phases (in degrees) of D-term for antenna Matera versus frequency

Freq (MHz)	Amp. RCP	Phase RCP
8212.99	$0.051^{+0.026}_{-0.029}$	142 ± 35
8228.99	$0.031^{+0.023}_{-0.030}$	123 ± 60
8244.99	$0.025^{+0.020}_{-0.030}$	166 ± 68
8276.99	$0.012^{+0.010}_{-0.031}$	36 ± 103
8308.99	$0.081^{+0.027}_{-0.029}$	50 ± 20
8324.99	$0.051^{+0.026}_{-0.029}$	11 ± 34
8356.99	$0.021^{+0.017}_{-0.030}$	88 ± 74
8372.99	$0.028^{+0.021}_{-0.030}$	131 ± 65
8404.99	$0.018^{+0.015}_{-0.030}$	86 ± 79
8420.99	$0.014^{+0.011}_{-0.031}$	177 ± 93
8436.99	$0.013^{+0.011}_{-0.031}$	53 ± 97
8500.99	$0.004^{+0.002}_{-0.033}$	94 ± 172
8516.99	$0.019^{+0.016}_{-0.030}$	74 ± 77
8532.99	$0.017^{+0.014}_{-0.030}$	145 ± 82
8564.99	$0.086^{+0.027}_{-0.028}$	-175 ± 19
8692.99	$0.023^{+0.019}_{-0.030}$	119 ± 71
8708.99	$0.022^{+0.018}_{-0.030}$	84 ± 72
8724.99	$0.023^{+0.019}_{-0.030}$	129 ± 71
8740.99	$0.034^{+0.024}_{-0.029}$	-112 ± 56
8772.99	$0.030^{+0.022}_{-0.029}$	151 ± 62
8788.99	$0.010^{+0.008}_{-0.031}$	-13 ± 119
8804.99	$0.011^{+0.009}_{-0.031}$	128 ± 112
8820.99	$0.021^{+0.017}_{-0.030}$	111 ± 75
8836.99	$0.021^{+0.017}_{-0.030}$	133 ± 75

Table C.14: Amplitudes (dimensionless) and phases (in degrees) of D-term for antenna Westford versus frequency

Freq (MHz)	Amp. RCP	Phase RCP
8212.99	$0.122^{+0.027}_{-0.028}$	129 ± 13
8228.99	$0.123^{+0.027}_{-0.028}$	115 ± 13
8244.99	$0.112^{+0.027}_{-0.028}$	106 ± 15
8276.99	$0.110^{+0.027}_{-0.028}$	78 ± 15
8308.99	$0.111^{+0.027}_{-0.028}$	49 ± 15
8324.99	$0.101^{+0.027}_{-0.028}$	39 ± 16
8356.99	$0.101^{+0.027}_{-0.028}$	-19 ± 16
8372.99	$0.100^{+0.027}_{-0.028}$	-15 ± 17
8404.99	$0.104^{+0.027}_{-0.028}$	-26 ± 16
8420.99	$0.110^{+0.027}_{-0.028}$	-33 ± 15
8436.99	$0.112^{+0.027}_{-0.028}$	-42 ± 15
8500.99	$0.125^{+0.027}_{-0.028}$	-100 ± 13
8516.99	$0.133^{+0.027}_{-0.028}$	-112 ± 12
8532.99	$0.157^{+0.027}_{-0.028}$	131 ± 10
8564.99	$0.145^{+0.027}_{-0.028}$	-139 ± 11
8692.99	$0.156^{+0.027}_{-0.028}$	160 ± 10
8708.99	$0.154^{+0.027}_{-0.028}$	155 ± 11
8724.99	$0.151^{+0.027}_{-0.028}$	136 ± 11
8740.99	$0.158^{+0.027}_{-0.028}$	142 ± 10
8772.99	$0.164^{+0.027}_{-0.028}$	118 ± 10
8788.99	$0.153^{+0.027}_{-0.028}$	114 ± 11
8804.99	$0.138^{+0.027}_{-0.028}$	106 ± 12
8820.99	$0.151^{+0.027}_{-0.028}$	93 ± 11
8836.99	$0.133^{+0.027}_{-0.028}$	87 ± 12

Table C.15: Amplitudes (dimensionless) and phases (in degrees) of D-term for antenna Effelsberg versus frequency

Freq (MHz)	Amp. RCP	Phase RCP
8212.99	$0.010^{+0.008}_{-0.031}$	-52 ± 121
8228.99	$0.003^{+0.002}_{-0.034}$	-174 ± 173
8244.99	$0.004^{+0.002}_{-0.033}$	111 ± 172
8276.99	$0.004^{+0.002}_{-0.033}$	61 ± 171
8308.99	$0.007^{+0.005}_{-0.032}$	145 ± 161
8324.99	$0.005^{+0.003}_{-0.033}$	14 ± 169
8356.99	$0.008^{+0.006}_{-0.032}$	-38 ± 142
8372.99	$0.005^{+0.003}_{-0.033}$	-100 ± 170
8404.99	$0.008^{+0.006}_{-0.032}$	-173 ± 147
8420.99	$0.007^{+0.005}_{-0.032}$	124 ± 159
8436.99	$0.008^{+0.006}_{-0.032}$	155 ± 149
8500.99	$0.005^{+0.003}_{-0.033}$	105 ± 169
8516.99	$0.009^{+0.007}_{-0.032}$	53 ± 134
8532.99	$0.011^{+0.008}_{-0.031}$	75 ± 115
8564.99	$0.007^{+0.005}_{-0.032}$	40 ± 159
8692.99	$0.022^{+0.018}_{-0.030}$	-11 ± 73
8708.99	$0.017^{+0.014}_{-0.030}$	-20 ± 83
8724.99	$0.012^{+0.009}_{-0.031}$	-37 ± 105
8740.99	$0.009^{+0.007}_{-0.031}$	18 ± 127
8772.99	$0.022^{+0.018}_{-0.030}$	52 ± 73
8788.99	$0.022^{+0.018}_{-0.030}$	68 ± 72
8804.99	$0.029^{+0.022}_{-0.029}$	61 ± 62
8820.99	$0.033^{+0.024}_{-0.029}$	64 ± 57
8836.99	$0.038^{+0.025}_{-0.029}$	54 ± 49

Appendix D

Polarization Leakage Plots

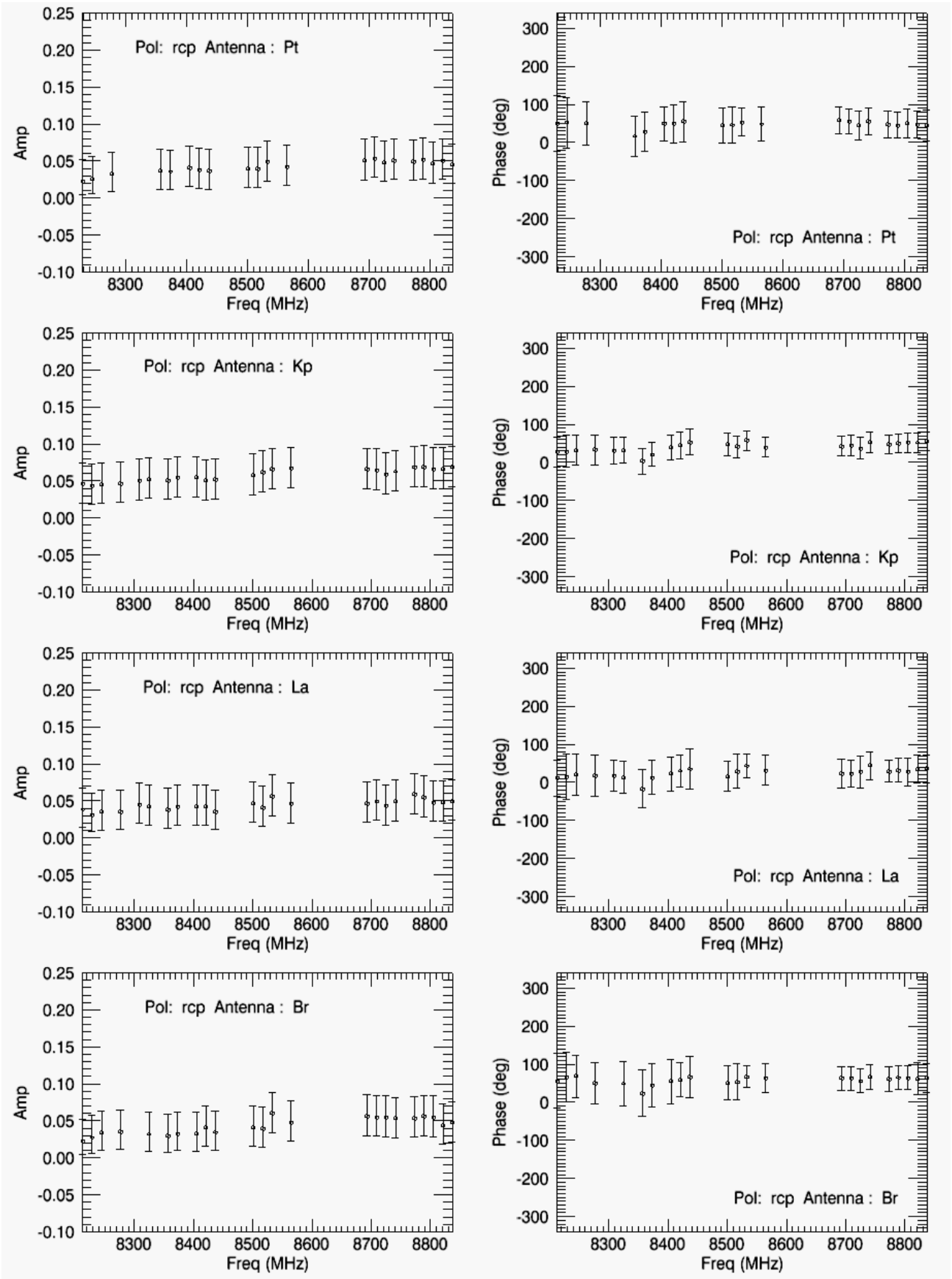

Figure D.1: Left column: RCP D-term amplitudes (dimensionless) versus frequency. Right column: RCP D-term phases versus frequency.

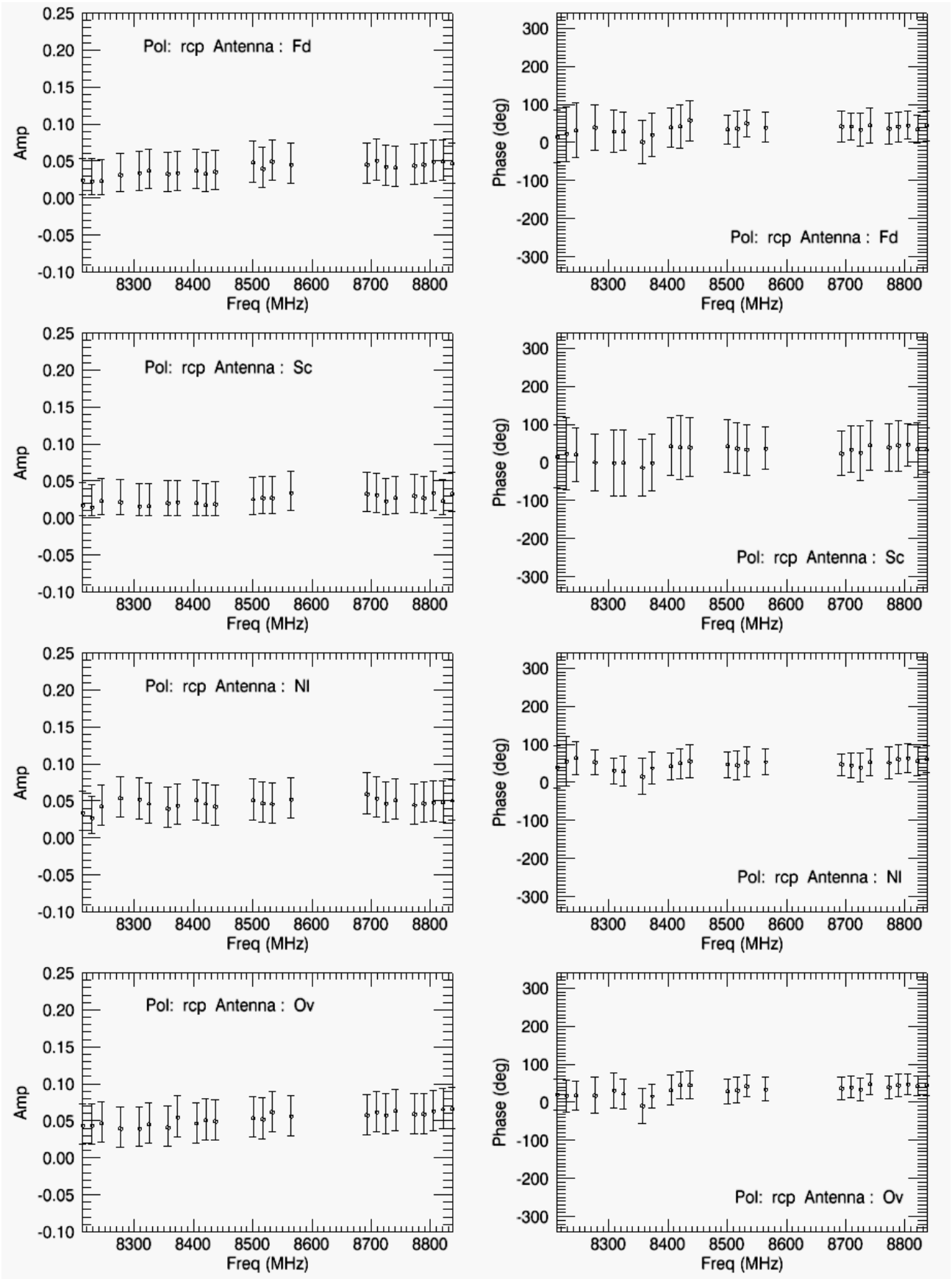

Figure D.2: Left column: RCP D-term amplitudes (dimensionless) versus frequency. Right column: RCP D-term phases versus frequency.

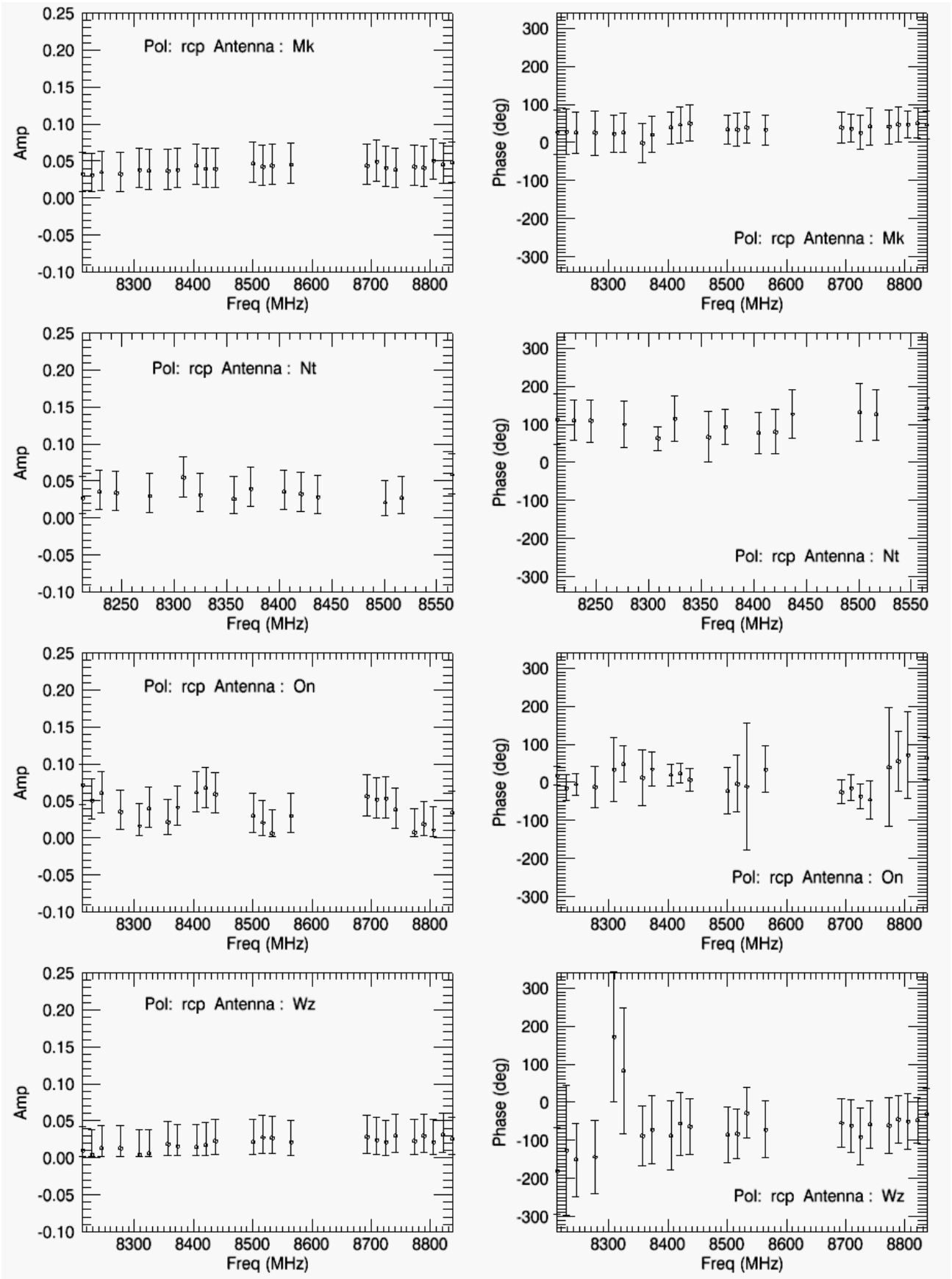

Figure D.3: Left column: RCP D-term amplitudes (dimensionless) versus frequency. Right column: RCP D-term phases versus frequency.

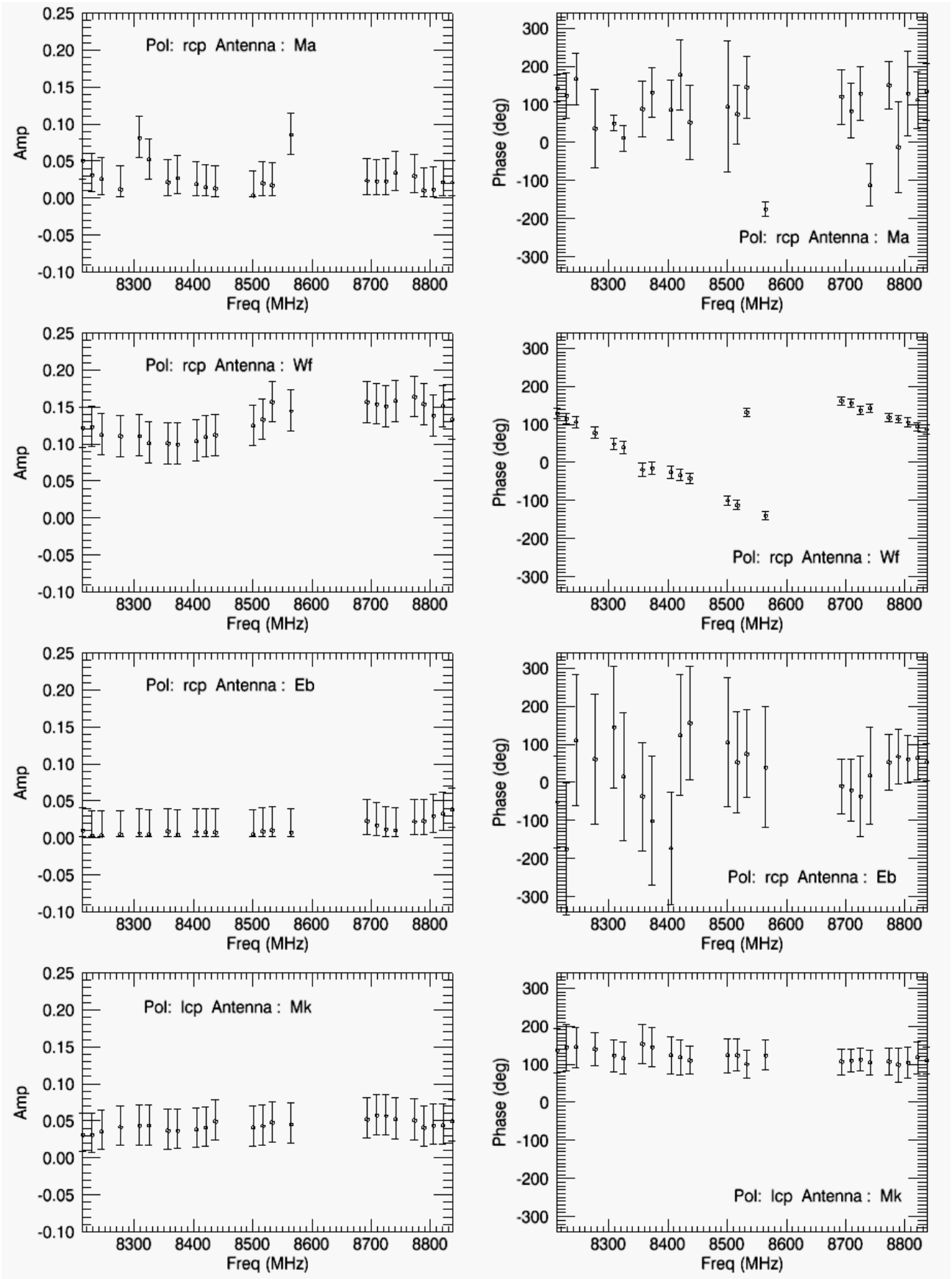

Figure D.4: First three rows, left column RCP D-term amplitudes (dimensionless) versus frequency, left column: RCP D-term phases versus frequency. Last row, left column: LCP D-term amplitudes (dimensionless) versus frequency and left column: LCP D-term phases versus frequency.

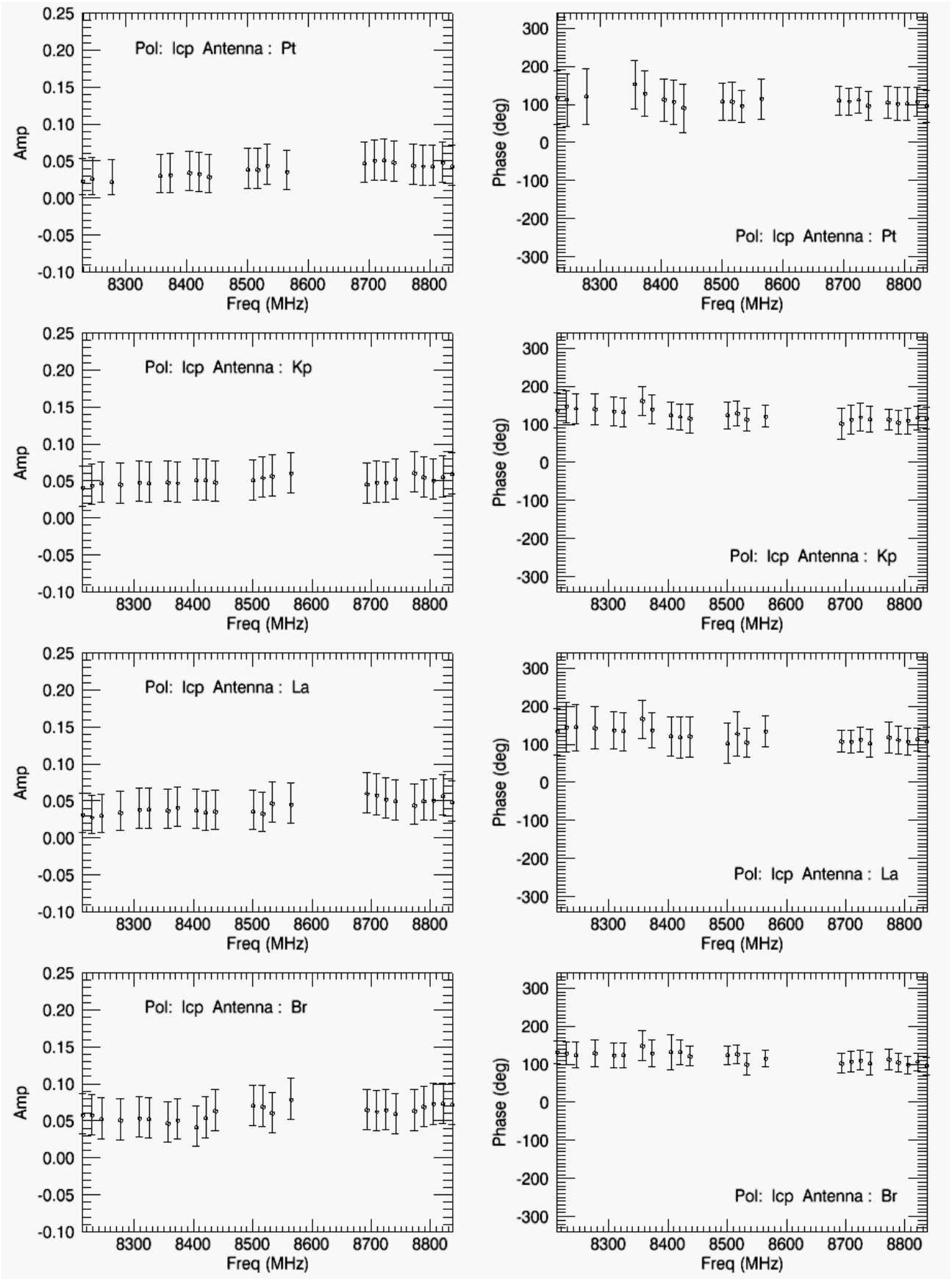

Figure D.5: Left column: LCP D-term amplitudes (dimensionless) versus frequency. Right column: LCP D-term phases versus frequency.

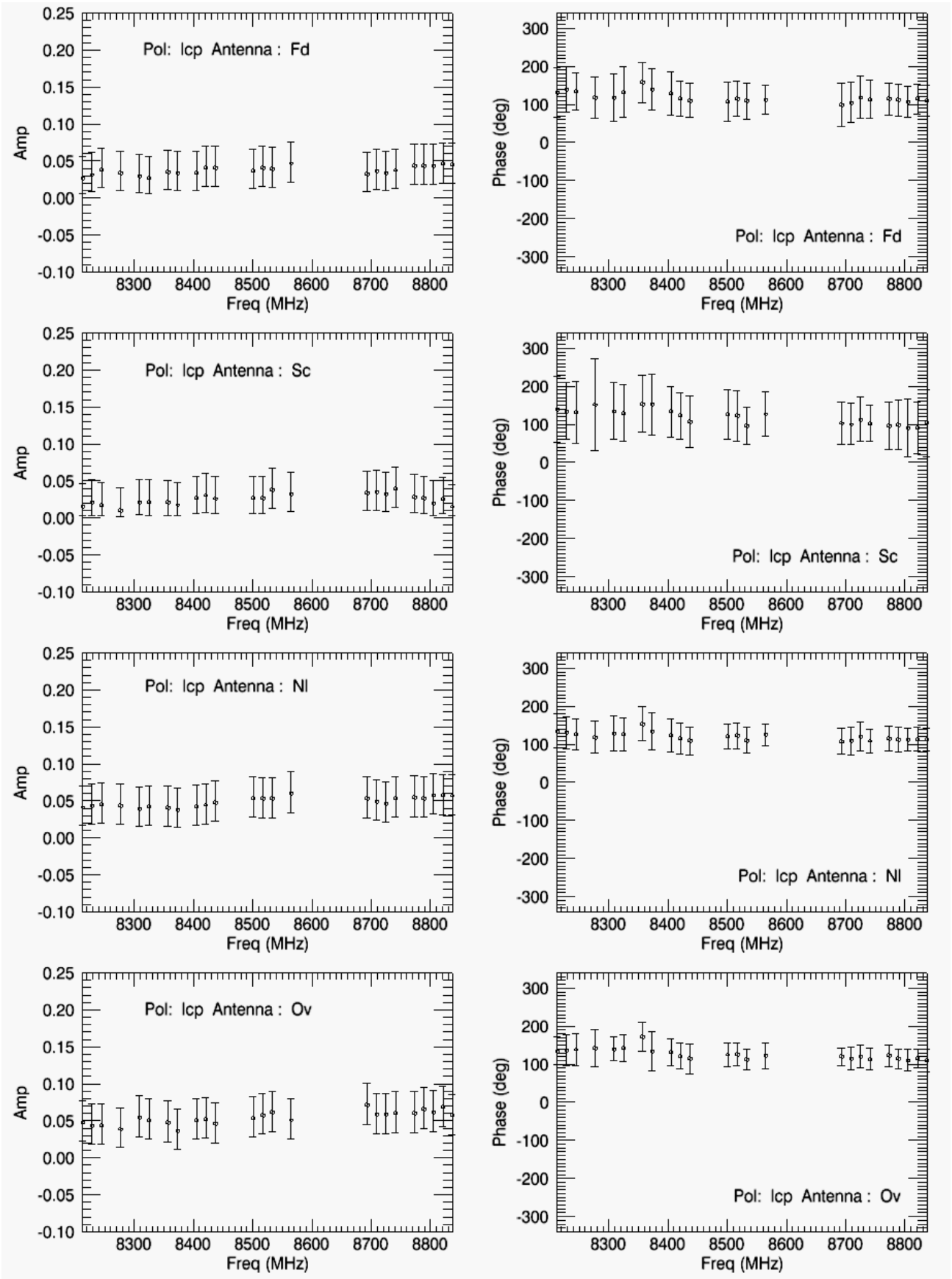

Figure D.6: Left column: LCP D-term amplitudes (dimensionless) versus frequency. Right column: LCP D-term phases versus frequency.

Appendix E

Corrections of the Leakage on the Delay

E.1 C-Program Source Codes

E.1.1 Pang.c

```
/*
 *
 * pang.c
 * calculates the parallactic angle
 *
 *
 * compile with gcc pang.c -lc -lm -o pang
 *
 *
*/

#include <stdio.h>
#include <math.h>
#include <string.h>
#include <stdlib.h>
#define INFIL  "OQ208.tbwdhj"
#define INFIL1 "1741-038.ukdwut"
#define OUTFIL "parallactic_angle.txt"
#define MAXCOLUMN 1000
#define MAXSTAT 64
#include "mk4_data.h" /*living in include*/
#include "vex.h"      /*living in include*/
#include "pass_struct.h" /*living in nfourfit  directory */
#include "param_struct.h" /*living in nfourfit directory */

void doy2date(int doy, int yy, int *mm, int *dd);

void pang(struct vex *root, struct type_pass *pass)
/* the structure vex is contained in ../include/vex.h */
```

```
{

   extern double PA[MAXSTAT];
   extern char PA_statid[MAXSTAT];
   struct station_struct *st;
   double argument1, argument2;
   double lat, h, delta;   /* h = hour angle of the source --
                              delta = declination of the source
                              lat = latitude of the antenna */
   double LST;         /* LST = local sidereal time --
                          ra = right ascension */
   double GMST, longi;     /* GST = Greenwich mean sidereal time --
                              longi = longitude  */
   double JD, UT, D;       /* JD = Julian date --
                              UT = universal time */
   double time;
   int    yy, mm, dd;
   double    hh, min;
   int rah, ram ;          /* rah = righ ascension hour --
                              ram = right ascension minute*/
   float ras;              /* ras = right ascension second */
   int decdeg, decmin ;
   float decsec;          /* decdeg = declination degree --
                             decmin = decl. min --
                             decsec = decl. sec */
   int UTh, UTmin, doy;    /* UTh = as read from scan name --
                              UTmin = as read from scan name,
                              doy = as read from scan name */
   int doyindex ;          /* doyindex = doy + 1 in leap years */
   double ra, dec;         /* ra = right ascension in hours --
                              dec = declination in radians*/
   int i = 0   ;           /* i = index for filling the vector
                              containing the station names and coordinates */
   int j;                  /* j = index for antennas coordinate and names */
   int c;                  /* c = in between to calculate the JD */
   int k;                  /* k =  index for resetting GMST between 0h and 24h  */
   int l;
   double x[MAXSTAT],y[MAXSTAT],z[MAXSTAT]; /* position of the station
                                               in meter from the centre of the Earth*/

/* read the ra values from the structure sky_coord defined in mk4_typedefs.h
 * root is variable name which is a pointer to data type vex contained in vex.h
 * in the structure vex there is a variable named ovex, which itsefl is a pointer
 * to a structure called scan_structure contained in ovex.h.
 * In the structure scan_structure there si a variable called src, which is a
 * structure of type source_struct contained in ovex.h. In the structure source_struct
 * there is a variable called position, which is a structure of type sky_coord contained
 * in mk4_typedefs.h.  In the structure sky_coord there are RA and DEC as reported below. */
```

```
   rah = root->ovex->src.position.ra_hrs;
   ram = root->ovex->src.position.ra_mins;
   ras = root->ovex->src.position.ra_secs;

/* conversion of ra in hours of time to calculate GMST as required by the formula below */

   ra = rah  + ram / 60. + ras /3600. ;

/* read the dec values from the structure sky_coord defined in mk4_typedefs.h*/

   decdeg = root->ovex->src.position.dec_degs;
   decmin = root->ovex->src.position.dec_mins;
   decsec = root->ovex->src.position.dec_secs;

/* conversion of dec in radiant for  calculating the parallactic angle*/

    dec = decdeg + decmin / 60. + decsec / 3600.; /* declination in degree of arc*/
    dec = dec * (M_PI / 180.);                    /* dec in radians */

/* read from structure type_pass contained in the file pass_struct.h.
 * reftime is the nr. of second since the start of the year*/

    time = pass->reftime;

/* calculate the DOY. The +1. is because C start to count from zero*/

    time = (time / 86400.) + 1. ;
    doy = floor(time);

/* UT hour*/

    hh = (time - doy) * 24.;
    UTh = floor(hh);

/* UT min*/

    UTmin = floor((hh - UTh) * 60.);

/* UT sec not used*/

/* conversion of UT in hours since --I belive-- to calculate JD I need UT in hours */

    UT = UTh + UTmin / 60. ;

/* find the year of the observation in the strucure mk4_typedefs.h*/
    yy = root->ovex->start_time.year;

//  printf("year %d\n", yy);
```

```
/* search for station one letter code in ovex.h
 * .h file:  vex.h
 *                 ovex.h
 *                       ovex.h
 *                           ovex.h
 * data type vex
 *                 scan_struct
 *                       station_struct
 *                           char
 * declared  fourfit.c                          */


    for (l = 0; l < root->ovex->nst; l++)
    {
      st = root->ovex->st + l;
      PA_statid[l] = st->mk4_site_id;

/* search for station coordinates respect to the centre of the Earth in ovex.h */
      x[l] = st->coordinates[0];
      y[l] = st->coordinates[1];
      z[l] = st->coordinates[2];

    }

/* conversion from doy to dd and mm and from yy I see whether I have a leap year */

   doy2date(doy, yy, &mm, &dd);

/* hour angle calculation from LST */

/* From http://www.astro.uu.nl/~strous/AA/en/reken/juliaansedag.html */

   if ( mm < 3 ) {
      mm = mm + 12 ;
      yy = yy - 1;
   }

   c = 2 - floor( yy / 100) + floor  (yy / 400);

   JD = floor(1461 * (yy +4716) / 4) + floor (153 * (mm + 1) /5) + dd + c -1524.5 + UT /24.;

   D = JD - 2451545.0;

/* from:  http://aa.usno.navy.mil/faq/docs/GAST.php */
/* GMST in hours: */

   GMST = 18.697374558 + 24.06570982441908 * D ;

/* the GMST must be reduced to the range from 0h to 24h */
```

```
   k = 0;
   while (GMST > 0) {
     GMST = GMST - 24.;
     k += 1;
   }
   k--;

   GMST = GMST + 24.;

/*http://www.csgnetwork.com/siderealjuliantimecalc.html
Greenw. lat = 51 deg 28 arcmin 38 arcsec N
        long = o deg 0 arcmin 0 srcsec */

/* the longitude is now in radians */

   for (j = 0; j < root->ovex->nst ; j++) {
     longi = atan2 (y[j] , x[j]);

/* the longitude is measured in time-measurement i.e. 15 deg = 1h; 15 arcmin = 1 min ;
/* 15arcsec = 1 sec -- pag 41 Smart */

     longi = (longi * 180./ M_PI) / 15. ; /* longi in hours */

     LST = GMST + longi;  /* - antenna is at east of Greenwich
                             + antenna is at west of Greenwich*/

/* h is in hour */

     h = LST - ra;

/* Calculation of the latitude starting from the positions
   in meter from the centre of the Earth -- from Smart */

/* lat is in radians = arctg (z / sqrt (x^2+y^2)) */

     lat =  atan2 (z[j] , sqrt( x[j] * x[j] + y[j] * y[j]));

/* let's select to have everything in radians*/

     h = (h *  15.) * M_PI/ 180. ;  /* hour angle in radians */

/* rotation due to the parallactic angle for altaz mounting from
   Radio Image synthesis II p. 115 */

    argument1 = (cos(lat) * sin(h));
    argument2 = (sin(lat) * cos (dec) - cos(lat) * cos(h) * sin(dec));

    PA[PA_statid[j] - 'A'] = atan2 (argument1 , argument2);
```

```
} /* close of the for*/
  return;
}

void doy2date(int doy, int yy, int *mm, int *dd) {

  int month[12] = {31,28,31,30,31,30,31,31,30,31,30,31};
  int i;

/* check if the year is a leap year*/

  if (((yy % 4 == 0) && (yy % 100 != 0)) || (yy & 400 == 0))  {
     month[1] = month[1] + 1;
  }

/* for each month from Jan upward,
 * subtract total number of days in month from day number in year,
 * until total <= 0
 */

  i = 0;
  while (doy > 0) {
    doy = doy - month[i];
    i += 1;
  }

/* back off one month, to make day number > 1 */

  i--;

/* c counts from zero, i.e. Jan would have a value of mm = 0,
   which is invalid */
  *mm = i + 1;
  *dd = doy + month[i];
  return;
}
```

E.1.2 Dterm_load.c

```
#include <stdio.h>
#include <math.h>
#include <string.h>
#include <stdlib.h>
#include "vex.h"
#define INFIL "/home/operator/GEO/BIN/Alessandra/fourfit/nfourfit/dterm_X-band.dat"
#define MAXCOLUMN 1000
#define bot_freq 8212.99 /*in MHz first freq observed*/
#define freq_int 16      /*in MHz - frequency interval*/
```

```
void dterm_load(struct vex *root)
{

    extern double PA[64];
    extern char PA_statid[64];
    extern double dterm_theta[65][65][65][3]; /* storage for visibility angle
                                                 correction due to dterm -
                                                 ref -  rem - freq - pol  */
    struct station_struct *sta;
    FILE *fp1; /* pointer to dterm file*/
    char line[MAXCOLUMN] ;
    char dterm_pol, dterm_stat2id[3];
    double dterm_amp, dterm_phase, dterm_freq;
    double dterm[64][64][2][2]; /* storage for dterm station - freq - pol - amp/phase */
    int freq_index, l;
    int stat_index_ref, stat_index_rem;
    int stat_index;
    int pol_index;
    double PA_ref, PA_rem;

 /* read input log file*/

   fp1 = fopen(INFIL, "r");
   if (fp1 == NULL) {
     printf("Trouble opening %s\n", INFIL);
      exit(1);
   }

/* dterm_theta and dterm initialization: */

     for (pol_index = 0; pol_index <= 1; pol_index++) {
        for (freq_index = 0; freq_index < 64; freq_index++) {
           for (stat_index_ref = 0; stat_index_ref < 64; stat_index_ref++){
              for (stat_index_rem = 0; stat_index_rem < 64; stat_index_rem++){
                 dterm_theta[stat_index_ref][stat_index_rem][freq_index][pol_index] = 0;
              }
              dterm[stat_index_ref][freq_index][pol_index][0] = 0;
              dterm[stat_index_ref][freq_index][pol_index][1] = 0;
           }
        }
     }

  /* read and process every line from input dterm file */

    fgets(line, MAXCOLUMN, fp1);
    while (!feof(fp1)) {
       sscanf(line, "%lf %2s %c %*lf %*lf %lf %lf", &dterm_freq, &dterm_stat2id,
                    &dterm_pol, &dterm_amp, &dterm_phase);
```

```
   freq_index = (dterm_freq - bot_freq) / freq_int;

   l = 0;
   sta = root->ovex->st;
   while (strstr(dterm_stat2id, sta->site_id) == NULL &&  l < root->ovex->nst)
   {
      l++;
      sta = root->ovex->st + l;
   }
   stat_index = sta->mk4_site_id - 'A';
   if (dterm_pol == 'R') {
      pol_index = 0;    /* pol_index = 0 => RCP*/
   }
   else pol_index = 1;  /*LCP*/
   dterm[stat_index][freq_index][pol_index][0] = dterm_amp;
   dterm[stat_index][freq_index][pol_index][1] = dterm_phase * (M_PI / 180.);
   fgets(line, MAXCOLUMN, fp1);

} /* end while*/

 for (pol_index = 0; pol_index <= 1; pol_index++) {
    for (freq_index = 0; freq_index < 64; freq_index++) {
       for (stat_index_ref = 0; stat_index_ref < 64; stat_index_ref++){
          for (stat_index_rem = 0; stat_index_rem < 64; stat_index_rem++){
             l = 0; /* now l is index for stepping along the PA_statid
                       array to find the matching ref/rem stations*/

             while ((PA_statid[l] - 'A' != stat_index_rem) && (l < 64)) {
                l++;
             } /*endwhile for PA_statid not equal to stat_index_ref*/
             PA_rem = PA[stat_index_rem];
             l= 0;
             while ((PA_statid[l] - 'A' != stat_index_ref) && (l < 64)) {
                l++;
             } /*endwhile for PA_statid not equal to stat_index_rem*/
             PA_ref = PA[stat_index_ref];

             dterm_theta[stat_index_ref][stat_index_rem][freq_index][pol_index] =
                  dterm[stat_index_ref][freq_index][pol_index][0] *
                  dterm[stat_index_rem][freq_index][pol_index][0] *
                  sin((dterm[stat_index_ref][freq_index][pol_index][1] -
                  dterm[stat_index_rem][freq_index][pol_index][1]) - 2 *
                  (PA_ref - PA_rem));

          } /*endfor stat_index_rem*/
       } /*endfor stat_index_ref*/
    } /*endfor freq_index*/
 } /* endfor  pol_index */
```

```
/* create a matix of dterm theta corrections that accomodate for all the possible fourfit
 * baseline conbination I.e. AB and BA will be equally catered for.*/

    return;

}
```

E.1.3 Dterm_apply.c

```
#include <stdio.h>
#include <math.h>
#include <string.h>
#include <stdlib.h>
#include "param_struct.h"
#include "pass_struct.h"
#include "vex.h"


#define bot_freq 8212.99
#define freq_int 16.
#define MAXCOLUMN 1000
double dterm_apply(struct type_pass *pass, int fr)
{

    extern struct mk4_fringe fringe;
    extern double PA[64];
    extern char PA_statid[64];
    extern double dterm_theta[65][65][65][3];
    extern struct type_param param;
    double freq_index;
    int stat_index_ref, stat_index_rem;
    int stat_index;
    int pol_index;
    int miss_freq_top = 0;
    int miss_freq_bot = 0;
    double miss_re, miss_im;
    double miss_freq;
    double dterm_re_1, dterm_im_1, dterm_re_2, dterm_im_2;
    double delta_dterm_re, delta_dterm_im;
    double delta_freq;
    double dterm_freq_top, dterm_freq_bot;

    freq_index = (pass->pass_data[fr].frequency - bot_freq) / freq_int ;

/* test to see whether I am between the frequencies that I have in dterm_X-band.dat.
   If no, then no correction to be implemented - > retunt zero*/
    if ((freq_index < 0) || (freq_index >= 64)){
        return(0.0);
    }
```

```
/*test whether dterm_theta is equal zero., i.e. I do not have any value in dterm_X-band.dat,
 but I am within the min-max range of it. If == 0, then need interpolation */

    if(dterm_theta[param.baseline[0]-'A'][param.baseline[1] -'A'][(int)floor(freq_index)][0] == 0
      || ((int)freq_index - freq_index) != 0.) {

/* search for the first occurrence in freq where dterm_theta has non zero value moving toward
 * the lower freqs*/
      while
      (dterm_theta[param.baseline[0]-'A'][param.baseline[1] -'A'][(int)floor(freq_index)][0] == 0
       && freq_index > 0) {
          freq_index--;
      }
      miss_freq_bot = (int)floor(freq_index);
/* reset the freq_index to the original value*/
      freq_index = (pass->pass_data[fr].frequency - bot_freq) / freq_int ;

/* search for the first occurence in freq where dterm_theta has non zero value moving toward the
 * higher freqs*/
      while
      (dterm_theta[param.baseline[0]-'A'][param.baseline[1] -'A'][(int)ceil(freq_index)][0] == 0
       && freq_index < 64) {
          freq_index++;
    }

      miss_freq_top = (int)ceil(freq_index);
/*handle the case where I reach the top or the bottom of the frequencies present in the
  file dterm_X-band.dat without having found any non-zero dterm_theta*/

      if((int)freq_index == 64) {
        return((dterm_theta[param.baseline[0]-'A'][param.baseline[1] -'A'][miss_freq_bot][0]));
      }
      else if (miss_freq_bot == 0) {
        return((dterm_theta[param.baseline[0]-'A'][param.baseline[1] -'A'][miss_freq_top][0]));
      }

/* reset the freq_index to the original value*/
      freq_index = (pass->pass_data[fr].frequency - bot_freq) / freq_int ;

/* do the interpolation using real and imaginary, easy to handle that phase*/
      dterm_re_1 =
         cos (dterm_theta[param.baseline[0]-'A'][param.baseline[1] -'A'][miss_freq_bot][0]);
      dterm_im_1 =
         sin (dterm_theta[param.baseline[0]-'A'][param.baseline[1] -'A'][miss_freq_bot][0]);
      dterm_re_2 =
         cos (dterm_theta[param.baseline[0]-'A'][param.baseline[1] -'A'][miss_freq_top][0]);
      dterm_im_2 =
         sin (dterm_theta[param.baseline[0]-'A'][param.baseline[1] -'A'][miss_freq_top][0]);
```

```
      delta_dterm_re = dterm_re_2 - dterm_re_1;
      delta_dterm_im = dterm_im_2 - dterm_im_1;

      dterm_freq_top = (miss_freq_top * freq_int) + bot_freq ;
      dterm_freq_bot = (miss_freq_bot * freq_int) + bot_freq ;
      delta_freq = dterm_freq_top - dterm_freq_bot;

      miss_freq = pass->pass_data[fr].frequency;

      miss_im = (((miss_freq - dterm_freq_bot) / delta_freq) * delta_dterm_im) + dterm_im_1;
      miss_re = (((miss_freq - dterm_freq_bot) / delta_freq) * delta_dterm_re) + dterm_re_1;

/*return the interpolated value of dterm_theta*/
      return(atan2(miss_im, miss_re));

    } /* endif for the dterm_theta == 0 */
    else {
/* if dterm_thena != 0, then no interpolation is needed and the value is returned*/
      return(dterm_theta[param.baseline[0]-'A'][param.baseline[1] -'A'][(int)freq_index][0]);
    }
}
```

E.1.4 Cmbd.c

```
/*
 *
 * cmbd.c
 * calculates the closure MBD
 *
 * compile with gcc cmbd.c -lc -lm -o cmbd
 *
 *
*/

#include <stdio.h>
#include <math.h>
#include <string.h>
#include <stdlib.h>
#define INFIL  "MBD_wo_dterm.txt"
#define OUTFIL "temp.txt"
#define MAXCOLUMN 1000
#define MAXANT 20
#define MAXBAS (MAXANT *( MAXANT -1)) / 2
#define MAXTRI (MAXANT * (MAXANT-1) * (MAXANT - 2)) / 6
    struct scan {
           char ref[MAXBAS];
           char rem[MAXBAS];
           char root[MAXBAS][20];
           double mbd[MAXBAS];
```

```
           char scan_name[MAXBAS][20];
           };
struct scan sc;
double baseline_mbd (int ref, int rem, int nr_bas);
int fill_ante (int nr_bas);
char ante[MAXANT];
main() {

    FILE *fp1, *fp2;        /* file pointers for I/O files */
    char band;
    char line[MAXCOLUMN];
    char *pt;
    int i, j, k, l, x, y, z;
    int maxtri, nt, nr_ant;
    double ac;
    char triangle[MAXTRI][4];
    int scan_name_flag; /* flag for finding the scan name*/
    double cmbd;

/* read mbd.txt file*/

    fp1 = fopen(INFIL, "r");
    if (fp1 == NULL) {
      printf("Trouble opening %s\n", INFIL);
      exit(1);
    }

/* Open output file cmbd.txt */

    fp2 = fopen(OUTFIL, "w");
    if (fp2 == NULL) {
      printf("Trouble opening %s\n", OUTFIL);
      exit(1);
    }

/* read and process every line from input root file */

    fgets(line, MAXCOLUMN, fp1);
    while (!feof(fp1)) {
     i = 0;
     scan_name_flag = 0;

/* read and process the root files within one scan*/


     while (!feof(fp1) && (scan_name_flag == 0)) {
       sscanf(line, "/datafs/%*4c/%s %c%c %c %lf",
              &sc.scan_name[i], &sc.ref[i], &sc.rem[i], &band, &sc.mbd[i]);
       if (band == 'X') {
```

```
         pt = strstr(sc.scan_name[i],"/");
         *pt = '\0';
         pt++;
         sscanf(pt, "%s", &sc.root[i]);

/* test to see if we are within the same scan */

        if(((strcmp(sc.scan_name[i], sc.scan_name[i-1]) != 0)
             || (strcmp(sc.root[i], sc.root[i-1]))) && (i > 0)) {
           scan_name_flag = 1;
        } /* close if strcmp */
        else
        i++;
       } /* close the if band == X*/
       if(scan_name_flag == 0){
          fgets(line, MAXCOLUMN, fp1);
       } /* close if scan_flag_name == 0 */
     } /* close the while scan_name_flag == 0 loop */

/* calculate how many antennas are present in the scan */
          nr_ant = fill_ante(i);

/* Triple nested loop over the antennas for calculating the cMBD */

/* Test if it is possible to build a triangle of baseline */
     if (nr_ant >= 3) {
      for (j = 0; j < nr_ant - 2; j++){
       for (k = j + 1; k < nr_ant -1; k++){
         for (l = k + 1; l < nr_ant; l++){
          cmbd = baseline_mbd(j,k,i) + baseline_mbd(k,l,i) - baseline_mbd(j,l,i);
//            fprintf(fp2, "%s %c%c%c %.7lf\n", sc.scan_name, ante[j], ante[k], ante[l], cmbd);
          fprintf(fp2, " %.7lf\n", cmbd);
         } /*close for l*/
       } /*close for k */
      } /*close for j */
     } /*close if nr_ant >= 3*/
    }/*close while eof*/
} /*close the main*/

double baseline_mbd (int ref, int rem, int nr_bas) {
  int u;
  u = 0;
 for(u = 0; u < nr_bas; u++) {
    if((sc.ref[u] == ante[ref]) && (sc.rem[u] == ante[rem])) {
     return(sc.mbd[u]);
    }
 }
 return(0);
}
```

```
int fill_ante(nr_bas) {

  int nr_ant;
  int i,j;
  int flag_rem, flag_ref;

  nr_ant = 1;
  ante[0] = sc.ref[0];
   for(i = 0; i < nr_bas; i++){
     flag_rem = 0;
     flag_ref = 0;
     for(j=0; j < nr_ant; j++){
      if(ante[j] == sc.ref[i]) {
        flag_ref = 1;
      }
      if(ante[j] == sc.rem[i]) {
        flag_rem = 1;
      }
     }
      if(flag_ref == 0) {
        ante[nr_ant] = sc.ref[i];
        nr_ant++;
      }
      if(flag_rem == 0)  {
        ante[nr_ant] = sc.rem[i];
        nr_ant++;
      }
   }

  return(nr_ant);

}
```

Appendix F

Glossary

AIPS Astronomical Image Processing System. Software used to reduce radio astronomical data.

Amplifier Device that increase the strength of a signal.

Angular Resolution or spatial resolution. Minimum angular distance between two sources that an optical device (i.e. telescope) can separate.

Antenna Device that converts an electromagnetic wave into a current flowing on a wire, if receiving or converts current into an electromagnetic wave, if transmitting.

BBC Baseband Converter. Device that downconverts the signal from intermediate frequency to baseband frequency.

Baseline Distance in metre or wavelength between two radio telescopes which observe as an interferometer.

CALC 8 Geometrical model applied by the correlators to the data. It is an additional delay that is inserted into the data stream, effectively moving the stations to be in the same wavefront.

Calibrator Well studied object whose characteristics are known and can be used to calibrate the system.

Clock offset Error present in the data due to imperfection in setting the station clock and imperfection in its rate.

Closure Quantities that are used to remove station-based errors.

Correlator Device that multiplies and integrates in time the data streams coming from two telescopes acting as an interferometer.

CP Circular Polarization. Property of a propagating electromagnetic wave in which the tip of the electric vector describes a circle with time.

Coordinate (u,v) plane Plane consisting of the baseline lengths in the E-W and N-S directions.

Crosstalk Unwanted coupling between signals in neighbouring electronics due to electromagnetic induction.

dB decibel. Logarithm in base 10 of the ratio between two measures multiplied by 10.

DAR Data Acquisition Rack. Electronics system for frequency conversion, filtering and sampling of signal that arrive from the antenna on the IF cables and outputs to the recorder.

D-term Vector that describes mathematically the polarization leakage. The amplitude (dimensionless) of this vector describes the fractional voltage leakage from one polarization into the other and whose phase (in degrees) is due to the electrical length of the leakage path.

Drudg Program run at the Mark IV stations for converting the schedule file into low level commands for the telescope control system.

EOP Earth Orientation Parameters. They describe the orientation of the Earth's rotation axis in space.

EVN European VLBI Network. Network of European radio observatories for regular astronomical VLBI observations.

Fringe fitting Process that estimates the signal delay and the rate of change of the delay between the signals received at two or more antennas.

Geometrical Delay Signal propagation time difference due to the physical separation between two antennas. It is given by the scalar product between the unit vector in the direction of the source and the vector between two antennas.

Group Delay Time for information to propagate between two places when transported by an electromagnetic wave. It is given by the first derivative of the phase delay expressed in turns of phase with respect to frequency.

HOPS Haystack Observatory Postprocessing System. Software used to reduce radio astronomical data.

Feed Horn Component of the receiver. It transform the radiation from free space into a waveguide.

IF Intermediate Frequency. Frequency to which the radio signal is down converted during the reception process for engineering reasons.

Flux Density Measure of the quantity of energy received per unit of time and area from a celestial body.

Radio Image Image of a radio source, which can be obtained using the Fourier transform relationship between the cross-correlation function and the brightness distribution of the source.

Interferometer Array of radio telescopes that observe simultaneously and combine their signal coherently to exploit the physical effect of interference.

IVS International VLBI Service. It supports astrometric, geodetic and geophysical activities.

Jansky Unit of measure of the flux density. $1Jy = 10^{-26}\frac{\mathrm{W}}{\mathrm{Hz}\cdot\mathrm{m}^2}$

JIVE Joint Institute for VLBI in Europe. Dedicate institute for VLBI research in Europe.

K5 Japanese data acquisition rack.

LCP Left Circular Polarization. Property of a propagating electromagnetic wave in which the tip of the electric vector describes a circle with time and rotates clockwise while looking at the source.

LO Local Oscillator. Device used to generate a sinusoidal signal of known frequency used to convert the radio signal down to a more convenient frequency.

Maser Atomic clock used at the stations to keep track of the time.

Mark IV Technology developed at the Haystack Radio Observatory including the Mark IV correlator and Mark IV data acquisition rack.

Maxwell equations Equations describing the electromagnetic field.

MBD Multiband Delay. Geodetic observable obtained from VLBI measurements.

NRAO National Radio Astronomical Observatory. U.S.-based research institution.

Passband Filter Device that blocks frequencies above and below a defined frequency band.

Parallactic Angle Is the angle between the line joining the radio source to the north celestial pole and the line joining the source to the zenith at the antenna.

Parsel Tongue Scripting language written in Python used as an interface to AIPS.

Patching Connection of the IFs to the BBCs.

Phase delay Total number of turn of phases though which an electromagnetic wave rotates when propagating e.g. through the atmosphere, and electronics.

Polarizer Device used to separate two state of polarization.

Polarization of light Statistical tendency of the electric field of the electromagnetic radiation to be oriented in a particular direction in space.

Polarization Leakage Contamination of the radio astronomical signal due to non-perfect separation of the two polarizations in the polarizer.

Position angle calibrator Radio astronomical source with known polarization position angle for calibrating the absolute phase offset between the two polarization channels at the stations.

PSF Point Spread Function. Response of an imaging system to a point-like source.

Quasar Quasi-stellar Radio Source.

Radiometer Equation.$\Delta S = \frac{1}{\eta_{\text{eff}}} \cdot \frac{\sqrt{\text{SEFD}_1 \cdot \text{SEFD}_2}}{\sqrt{2 \cdot \Delta\nu \cdot \tau_{\text{int}}}}$. Where SEFD_1 and SEFD_2 are the system equivalent flux densities expressed in jansky for the two antennas, η_{eff} is the correlation efficiency (equal to 0.5 for 1 bit/sample and equal to 0.7 for 2 bit/sample), $\Delta\nu$ is the bandwidth in hertz, τ_{int} is the integration time in second, and ΔS is the root mean square (rms) thermal noise fluctuations expected in the measurement, in jansky.

RCP Right Circular Polarization. Property of a propagating electromagnetic wave in which the tip of the electric vector describes a circle with time and rotates anticlockwise while looking at the source.

RD0705 VLBI experiment designed and used to calculate the polarization leakage.

Receiver Device composed of a feed horn, polarizer, antenna and amplifier.

Response of an Interferometer Behaviour of the correlator output as the source moves across the sky.

RF Radio Frequency. Electromagnetic radiation whose frequency range from 3 kHz to 300 GHz.

Rice Distribution A non-parametric probability distribution.

S-band Frequency band between 2 GHz to 4 GHz.

Schedule File that contains the information needed by the telescope operators and the telescope control computers to conduct the observation.

SEFD System Equivalent Flux Density. Parameter describing the sensitivity of antennas in Jy.

Sensitivity Minimum flux density that can be detected by an antenna.

SNR Signal-to-noise Ratio.

UT Universal Time.

Visibility Cross-correlation coefficients between the signals coming from two radio telescopes.

VLBA Very Long Baseline Array. Set of 10 radio telescopes built and owned by NRAO.

VLBA4 Kind of data acquisition rack.

VLBI Very Long Baseline Interferometry.

Waveguide Metal pipe used to transport electromagnetic waves.

X-Band Frequency band between 8 GHz and 12 GHz.

Zenith delay Propagation delay due to atmospheric constituents.

Bibliography

Airy G (1835) On the Diffraction of an Object-glass with Circular Aperture. Transactions of the Cambridge Philosophical Society pp 283–291

Alef W, Graham D (2002) The New Bonn Mk IV - AIPS Data Export Path. In: Proceedings of the 6th European VLBI Network Symposium, pp 31–32

Arndt F (1996) Hochfrequenztechnik Band I. Notes for Bremen University students. Course in RF and Microwave Engineering

Bertarini A, Titus M, Kingham K, Hall D (2009) What the Correlators Can Do for You. Diagnosis of Station Performance (and more) Using Aedit & Fourfit. Tech. rep., MIT Haystack Observatory, Technical Operation Workshop

Born M, Wolf E (1999) Principle of Optics. Cambridge University Press, ISBN 9780521642224

Brophy JJ (1990) Basic Electronic for Scientists. McGraw-Hill, Inc. New York, ISBN 88-383-1083-1

Burg JP (1967) Maximum Entropy Spectral Analysis. In: Proceedings of the 37th Meeting of the Society Exploratory Geophysics

Carilli CL, Carlstrom J, Holdaway M (1999) Synthesis Imaging in Radio Astronomy II, Astronomical Society of the Pacific Conference Series, vol. 180., chap 28, Millimetre Interferometry, pp 565–600. ISBN 1-58381-005-6

Chao BF (2004) Earth Rotational Variations Excited by Geophysical Fluids. In: Baver NRVKD (ed) International VLBI Service for Geodesy and Astrometry 2004 General Meeting Proceedings, pp 38–46, NASA/CP-2004-212255

Charlot P (1990) Radio-Source Structure in Astrometric and Geodetic Very Long Baseline Interferometry. Astronomical Journal 99:1309–1326

Clark BG (1999) Synthesis Imaging in Radio Astronomy II, Astronomical Society of the Pacific Conference Series, vol. 180., chap 1, Coherence in Radio Astronomy, pp 2–10. ISBN 1-58381-005-6

Clark TA, Rogers AEE (1982) Mark III VLBI Data Acquisition Terminal. NASA/Goddard Space Flight Center, Space Geodesy Program

Clark TA, Corey BE, Davis JL, Elgered G, Herring TA, Hinteregger HF, Knight CA, Levine JI, Lundquist G, Ma C, Nesman EF, Phillips RB, Rogers AEE, Ronnang BO, Ryan JW, Schupler BR, Shaffer DB, Shapiro II, Vandenberg NR, Webber JC, Whitney AR (1985) Precision Geodesy Using the Mark-III Very-Long-Baseline Interferometer System. IEEE Transactions on Geoscience and Remote Sensing GE-23(4):438–449

Corey BE, Clark TA (1991) The RF Bandwidth Upgrade: Doubling the X-Band Spanned Bandwidth of Geodetic VLBI Receiving Systems. In: Geodetic VLBI: Monitoring Global Change

Corey BE, Titus M (2006) Antenna Cross-Polarization Characteristics at Geodetic VLBI. In: Baver DBKD (ed) IVS 2006 General Meeting Proceedings, pp 1–5, NASA/CP-2006-214140

Cornwell T (1995) Imaging Concepts. In: J A Zensus, P J Diamond, & P J Napier (ed) Very Long Baseline Interferometry and the VLBA, Astronomical Society of the Pacific Conference Series, vol 82, pp 39–+

Cornwell T, Fomalont EB (1999) Synthesis Imaging in Radio Astronomy II, Astronomical Society of the Pacific Conference Series, vol. 180., chap 10, Self-Calibration, pp 187–199. ISBN 1-58381-005-6

Cotton WD (1999) Synthesis Imaging in Radio Astronomy II, Astronomical Society of the Pacific Conference Series, vol. 180., chap 6, Polarization in Interferometry, pp 111–126. ISBN 1-58381-005-6

Fomalont EB (1999) Synthesis Imaging in Radio Astronomy II, Astronomical Society of the Pacific Conference Series, vol. 180., chap 23, Astrometry anfd Geodesy, pp 463–479. ISBN 1-58381-005-6

Gomez JL (2002) Polarization Calibration of the VLBA Using the D-terms. Tech. rep., National Radio Astronomy Observatory, VLBA Scientific Memo No. 30

Gontier AM, Britzen S (1994) Influence of Radio Source Structure on Geodetic VLBI Analysis. In: Kus AJ, Schilizzi RT, Borkowski KM, Gurvit LI (eds) 2nd EVN/JIVE Symposium, pp 9–+

Hertz H (1889) Üeber Strahlen Electrischer Kraft. Annalen der Physik und Chemie 36:769–783

Hinteregger HF, Shapiro II, Robertson DS, Knight CA, Ergas RA, Whitney AR, Rogers AAE, Moran JM, Clark TA, Burke BF (1972) Precision Geodesy via Radio Interferometry. Science, New Series 178:396–398

Högbom JA (1974) Aperture Synthesis with a Non-Regular Distribution of Interferometer Baselines. Astronomy & Astrophysics Supplement 15:417–+

Jackson JD (1998) Classical Electrodynamics. Wiley, New York, ISBN 978-0-47130-932-1

Jackson N, Battye RA, Browne IWA, Joshi S, Muxlow TWB, Wilkinson PN (2007) A Survey of Polarization in the JVAS/CLASS Flat-Spectrum Radio Source Surveys - I. The Data and Catalogue Production. MNRAS 376:371–377

Johnson CJ, Jasik H (1984) Antenna Engineering Handbook. McGraw-Hill Inc., ISBN 978-0070322912

Johnson RW (2001) An Introduction to the Bootstrap. Teaching Statistics pp 49–54

Kemball A, Martinsek A (2005) Bootstrap Resampling as a Tool for Radio Interferometric Imaging Fidelity Assessment. Astronomical Journal 129:1760–1775

Kemball AJ (1999) Synthesis Imaging in Radio Astronomy II, Astronomical Society of the Pacific Conference Series, vol. 180., chap 25, VLBI Polarimetry, pp 499–509. ISBN 1-58381-005-6

Kovalev YY, Petrov L, Fomalont EB, Gordon D (2007) The Fifth VLBA Calibrator Survey - VCS5. Astronomical Journal 133:1236–1242

Leppanen KJ, Zensus JA, Diamond PJ (1995) Linear Polarization Imaging with Very Long Baseline Interferometry at High Frequencies. Astronomical Journal 110:2479–+

Massi M, Aaron S (1997) Stability of EVN D-terms. Tech. rep., European VLBI Network, EVN Doc. no. 77

Massi M, Rioja M, Gabuzda D, Leppänen K, Sanghera H, Ruf K, Moscadelli L (1997) Baseline Errors in European VLBI Network Measurements. III. The Dominant Effect of Instrumental Polarization. Astronomy & Astrophysics 318:L32–L34

Niell A, Whitney A, Petrachenko W, Schlüter W, Vandenberg N, Hase H, Koyama Y, Ma C, H S, Tuccari G (2007) VLBI2010: A Vision for Future Geodetic VLBI. In: IAG Symposia, vol 130, pp 757–759

Olsson R, Kildal PS, Weinreb S (2006) The Eleven Antenna: a Compact Low-Profile Decade Bandwidth Dual Polarized Feed for Reflector Antennas. IEEE Transactions on Antennas and Propagation pp 368–375

Porcas RW (2009) Radio Astrometry with Chromatic AGN Core Positions. Astronomy & Astropysics Letters pp L1–L4

Robertson DS (1991) Geophysical Applications of Very-Long-Baseline Interferometry. Reviews of Modern Physics 63:899–918

Rogers AEE (1991) Instrumentation Improvements to Achieve Millimeter Accuracy. In: Geodetic VLBI: Monitoring Global Change, pp 1–+

Rohlfs K, Wilson TL (1996) Tools of Radioastronomy, Springer-Verlag Telos; 2nd edition, chap 3, Wave Polarization, pp 33–47. ISBN 978-3540609810

Romney JD (1999) Synthesis Imaging in Radio Astronomy II, Astronomical Society of the Pacific Conference Series, vol. 180., chap 4, Cross-Correlators, pp 57–78. ISBN 1-58381-005-6

Schwab FR, Cotton WD (1983) Global Fringe Search Techniques for VLBI. Astronomical Journal 88:688–694

Sorgente M, Massi M (1997) Preliminary Study on the Influence of the Instyrumental Polarization on Geodetic Data. Tech. rep., European VLBI Network, EVN Doc. no. 107/2000

Sovers OJ, Fanselow JL, Jacobs CS (1998) Astrometry and Geodesy with Radio Interferometry: Experiments, Models, Results. Rev Mod Phys 70(4):1393–1454

Stanghellini C, Bondi M, Dallacasa D, Jiang DR, Rioja MJ, Sanghera HS (1996) The Radio Source OQ208. Memorie della Societa Astronomica Italiana 67:1047–+

Thompson AR (1993) An Introduction to the VLBA Receiving and Recording System. National Radio Astronomy Observatory, VLBA Technical Report No. 15 (Rev. A)

Thompson AR (1999) Synthesis Imaging in Radio Astronomy II, Astronomical Society of the Pacific Conference Series, vol. 180., chap 2, Foundamentals Of Radio Interferometry, pp 11–36. ISBN 1-58381-005-6

Thompson AR, D'Addario L (1984) Frequency Response of a Synthesis Array: Performance Limitations and Design Tolerances. Radio Science 17:357

Thompson AR, Moran, J M GW Swenson (2001a) Interferometry and Synthesis in Radio Astronomy, Second Edition. John Wiley & Sons, Inc., ISBN 88-383-1083-1

Thompson AR, Moran, J M GW Swenson (2001b) Interferometry and Synthesis in Radio Astronomy, Second Edition, John Wiley & Sons, Inc., chap 6, Response of the Receiving System, pp 168–211

Tornatore V, Charlot P (2007) The Impact of Radio Source Structure on European Geodetic VLBI Measurements. Journal of Geodesy 81:469–478

Vandenberg NR (1997) drudg: Experiment Preparation Drudge Work. NASA/Goddard Space Flight Center, Space Geodesy Program, VLBI Software Manual, http://vlbi.gsfc.nasa.gov/files_user_manuals/sked/drudg.pdf

Vandenberg NR (1999) sked: Interactive/Automatic Scheduling Program. NASA/Goddard Space Flight Center, Space Geodesy Program, VLBI Software Manual, http://lupus.gsfc.nasa.gov/files_user_manuals/sked/sked.pdf

Walker RC (2009) THE SCHED USER MANUAL Version 8.1. National Radio Astronomy Observatory, http://www.aoc.nrao.edu/cwalker/sched/sched/sched.html

Weisstein EW (1999) Interquartile Range. From MathWorld–A Wolfram Web Resource. http://mathworld.wolfram.com/InterquartileRange.html

Whitney AR (2000) How Do VLBI Correlators Work? In: N R Vandenberg & K D Baver (ed) International VLBI Service for Geodesy and Astrometry 2000 General Meeting Proceedings, pp 187–205, NASA/CP-20000209893

Whitney AR, Cappallo R, Aldrich W, Anderson B, Bos A, Casse J, Goodman J, Parsley S, Pogrebenko S, Schilizzi R, Smythe D (2004) Mark 4 VLBI Correlator: Architecture and Algorithms. Radio Science 39:RS1007

Wrobel JM, Walker RC (1999) Synthesis Imaging in Radio Astronomy II, Astronomical Society of the Pacific Conference Series, vol. 180., chap 9, Sensitivity, pp 171–185. ISBN 1-58381-005-6

Acknowledgement

Special thanks to my supervisor Axel Nothnagel, to the assessors Heiner Kuhlmann and Anton Zensus, and to
Alan Roy, Brian Corey, Craig Walker, Ed Himwich, Cormac Reynolds, John Gibson, Walter Alef, Dave Graham, Maria Massi, Leonid Petrov, Arno Müskens, Simone Bernhart, Laura La Porta, Helge Rottmann, Alexander Neidhard, Christian Plötz, Alan Rogers, Annamaria Davanzo, Claudio Bertarini.

and to my daughter S A B R I N A.